Stony Brook University

Multifunctional Smart Structures for Energy Harvesting, Structure Health Monitoring, and Vibration Control

A Dissertation Presented

by

Wanlu Zhou

to

The Graduate School

in Partial Fulfillment of the

Requirements

for the Degree of

Doctor of Philosophy

in

Mechanical Engineering

Stony Brook University

August 2015

Stony Brook University

The Graduate School

Wanlu Zhou

We, the dissertation committee for the above candidate for the

Doctor of Philosophy degree, hereby recommend

acceptance of this dissertation.

Dr. Lei Zuo – Dissertation Advisor
Associate Professor, Department of Mechanical Engineering

Dr. Imin Kao – Co-Advisor
Associate Dean, College of Engineering and Applied Sciences
Professor, Department of Mechanical Engineering

Dr. Jeffrey Ge - Chairperson of Defense
Professor and Chair, Department of Mechanical Engineering

Dr. John Murray
Associate Professor, Department of Electrical & Computer Engineering
Stony Brook University

This dissertation is accepted by the Graduate School

Charles Taber
Dean of the Graduate School

Abstract of the Dissertation

Multifunctional Smart Structures for Energy Harvesting, Structure Health Monitoring, and Vibration Control

by

Wanlu Zhou

Doctor of Philosophy

in

Mechanical Engineering

Stony Brook University

2015

Smart structure, which is defined as "a system or material which has built-in or intrinsic sensors, actuators and control mechanisms is capable of responding adaptively to the environment", has attracted more and more interest in recent decades, especially in the applications of aerospace, civil, and mechanical infrastructures. Piezoelectric, with its special electromechanical characteristics, is widely used in the smart structure design. Piezoelectric-based multifunctional smart structures for integrated vibration energy harvesting, structure health monitoring, and vibration control are studied in this dissertation.

In the aspect of energy harvesting, a novel piezoelectric energy harvester with multi-mode dynamic magnifier is proposed and investigated, which is capable of significantly increasing the bandwidth and the energy harvested from the ambient vibration. In addition, a 33-mode multilayer piezoelectric stack with force amplification frame is designed and studied, which has large power generation and high power density ratio. In the aspect of structure health monitoring, an admittance-based structure health monitoring method with a high-order resonant circuit is proposed and investigated, with advantage of increased damage detection sensitivity. In the aspect of vibration control, a self-powered piezoelectric vibration control system is proposed and investigated for flexible structures, with both functions of minimizing the vibration of the flexible structure and at the same time harvesting energy for the self-powered control implementation. In addition, a vibration and wave propagation attenuation method for metamaterials with periodic piezoelectric arrays with high-order resonant circuit shunts is proposed and developed. The proposed high-order resonant shunt circuit can introduce two local resonances in series around the tuning frequency to broaden the attenuation bandwidth, or can create two separate resonances to achieve two separate bandgaps.

Table of Contents

List of Figures

List of Tables

Acknowledgments

For the past five years in pursuing my Ph.D. degree in the Department of Mechanical Engineering at Stony Brook University, I would like to thank a lot of people who helped me a lot in research, course study, and life.

First and foremost, I would like to express my deepest thanks to my advisor, Dr. Lei Zuo, for his guidance and cultivation since the first day I joined his group. He is a smart, rigorous, and knowledgeable scholar. He can always give constructive and valuable instructions on projects in our group. Besides, Dr. Lei Zuo is the most hardworking person I have ever seen. Everyday he only sleeps very short time, and spends the rest of day on projects and proposals. He is very conscientious to research, exploring deep in academic problems. He emphasizes a lot on "curiosity", "creativity", and "self-motivation" in doing research. He is also very kind to help me build my career, and train me in the career direction. I really learned a lot from him.

Second, I would like to thank Dr. Tian-Bing Xu at National Institute of Aerospace. We have collaborative projects on piezoelectric stack energy harvesting. I learned a lot on his innovative design of multilayer piezoelectric stack energy harvester with force amplification frame.

I also want to thank my previous partner, Gopinath Reddy Penamalli, who already graduated and is now working in a company in Michigan. Since Gopinath joined the group one year earlier than me and he is the person in our group firstly started piezoelectric projects, he taught and helped me a lot in the project, especially at the beginning time.

I would like to thank Prof. Kao, Prof. Ge, and Prof. Murray to serve on my dissertation committee. Their knowledgeable insights and suggestions greatly enrich my dissertation.

In addition, I would like to thank many of my lab mates, Xiudong Tang, Xiaoming Chen, Tao Ni, Zhongjie Li, Bo Zhang, Peng Li, Yilun Liu, Changwei Liang, Hongbo Yu. Thank you for your help on both my study and daily life.

At last, I would like to thank my parents, my husband You Wu, and my dearest son Aiden. Thank you all for bringing me a happy life.

Vita, Publications and/or Fields of Study

[1] W. Zhou, Y. Wu and L. Zuo, 2015, "Vibration and Wave Propagation Attenuation for Metamaterials by Periodic Piezoelectric Arrays with High-Order Resonant Circuit Shunts", *Smart Materials and Structures*, 24, 065021.

[2] W. Zhou and L. Zuo, 2014, "A Self-Powered Piezoelectric Vibration Control System with Switch Pre-Charged Inductor (SPCI) Method", *IEEE/ASME Transactions on Mechatronics*, 10.1109/TMECH.2014.2299792.

[3] W. Zhou and L. Zuo, 2012, "Sensitivity-Enhanced Admittance-Based Structure Health Monitoring using a Higher-Order Resonant Circuit", *Smart Materials and Structures*, 21, 105023.

[4] W. Zhou, G. R. Penamalli and L. Zuo, 2012, "An Efficient Vibration Energy Harvester with Multi-Mode Dynamic Magnifier", *Smart Materials and Structures*, 21, 015014.

[5] T. B. Xu, E. Siochi, J. H. Kang, L. Zuo, W. Zhou, X. Tang and X. Jiang, 2013, "Energy Harvesting using a PZT Ceramic Multilayer Stack", *Smart Materials and Structures*, 22, 065015.

[6] P. Musgrave, W. Zhou and L. Zuo, 2015, "Piezoelectric Energy Harvesting from Torsional Vibration", *ASME 2015 International Design Engineering Technical Conferences*, Aug 2-5, Boston, MA.

[7] S. Chen, L. Wang, W. Zhou, P. Musgrave and L. Zuo, 2015, "Optimal Design of Force Magnification Frame of a Piezoelectric Stack Energy Harvester", *SPIE Smart Structures/NDE*, March 9-12, San Diego, CA.

[8] Y. Wu, W. Zhou, L. Zuo, and H. Sun, 2014, "Broad-Band Motion Regulating Pendulum Energy Harvester", *ASME 2014 Dynamic Systems and Control Conference*, Oct 22-24, San Antonio, TX.

[9] W. Zhou, L. Zuo, and T. B. Xu, 2014, "Energy Delivery from Piezoelectric Structure to Resistive Load", *Twelfth International Conference on Motion and Vibration Control (MOVIC 2014)*, August 4-6, Sapporo, Japan. (*Invited talk*)

[10] W. Zhou, Y. Wu, and L. Zuo, 2014, "Cantilever Beam Metamaterial Structure with Periodic Piezoelectric Arrays with High-Order Resonant Circuit Shunts for Vibration Control", *ASME 2014 Conference on Smart Materials, Adaptive Structures and Intelligent Systems*, September 8-10, Newport, RI.

[11] Y. Wu, L. Zuo, W. Zhou, C. Liang, and M. McCabe, 2014, "Multi-source energy harvester for wildlife tracking", *SPIE Smart Structures/NDE*, March 10-13, San Diego, CA.

[12] W. Zhou, T. B. Xu and L. Zuo, 2013, "A Piezoelectric Multilayer-Stack Energy Harvester with Flextensional Frame", *MFPT 2013 and ISA's 59th International Instrumentation Symposium*, May 13-17, Cleveland, OH.

[13] W. Zhou and L. Zuo, 2013, "A Novel Piezoelectric Multilayer Stack Energy Harvester with Force Amplification", *Proceedings of the ASME 2013 International Design Engineering Technical Conferences & Computers and Information in Engineering Conference, IDETC/CIE 2013*, August 4-7, Portland, OR.

[14] W. Zhou and L. Zuo, 2013, "A Self-Powered Piezoelectric Vibration Control System with Switch Pre-Charged Inductor (SPCI) Method", *American Control Conference*, June 17-19, Washington, DC.

[15] W. Zhou, Y. Wu and L. Zuo, 2013, "Experiment Study on Damage Detection Method with Higher-Order Circuit", *SPIE Smart Structures/NDE*, March 12-13, San Diego, CA.

[16] W. Zhou, G.R. Penamalli and L. Zuo, 2012, "Admittance-Based Damage Detection Method using a Higher-Order Circuit", *2012 Proceedings of SPIE in Smart Structures*, March 11-15, San Diego, CA.

[17] T.B. Xu, J.H. Kang, E. Siochi, L. Zuo, W. Zhou, X. Tang and X. Jiang, 2011, "A Piezoelectric Ceramic Multilayer Stack for Energy Harvesting under Dynamic Forces", *ASME Design Engineering Technical Conferences*, Aug. 28-31, Washington DC.

[18] W. Zhou, G.R. Penamalli and L. Zuo, 2011, "Multi-Mode Vibration Energy Harvester and Tuned Mass Damper using Double-Beam Structure", *2011 ASME International Mechanical Engineering Congress and Exposition (IMECE)*, Nov 11-17, Denver, Colorado.

Chapter 1 Introduction

1.1 Background of Smart Structures

"Smart structure" is defined as "A system or material which has built-in or intrinsic sensors, actuators and control mechanisms whereby it is capable of sensing a stimulus, responding to it in a predetermined manner and extent, in a short/appropriate time, and reverting to its original state as soon as the stimulus is removed" [1]. It can respond adaptively in a pre-designed useful and efficient way to changes in environmental conditions, also including changes in its own condition. One example is an active aero-elastic wing (AAW), which is comprised of mechanical structure, control unit, smart materials, and sensors, capable of commanding shape changes based on real-time flight data. By incorporating distributed sensing networks, flight control algorithms can use real-time structural and aerodynamic data to alter speed, reduce observability, or increase maneuverability, based on mission objectives or immediate needs.

The increased interest in multifunctional smart structures is driven by the need for the development of new structures that can simultaneously perform multiple functions [2]. In many cases, the same material or device can be used for both sensing and actuation functions, as well as for other functions like energy harvesting and structural health monitoring. Piezoelectric materials, such as lead zirconate titanate (PZT), polyvinylidene fluoride (PVDF) and aluminum nitride (AlN), can be embedded in structures for sensing and actuation, as they naturally possess the required electromechanical coupling. The basic idea behind energy harvesting as related to multifunctional smart structures is to parasitically extract energy from the motion or deformation of a host structure and convert it to electrical energy which can be stored and used for other purposes. One popular application is to power small electronic devices such as wireless sensors for structural health monitoring purpose.

1.2 Smart Structures for Wind Turbine Blade and Helicopter Blade

1.2.1 Wind turbine blade vibration

Wind power investment worldwide is expected to expand three-fold from about $18 billion in 2006 to $60 billion in 2016 [3]. However, there are still many challenges in the wind turbine technologies. One big problem is that the unwanted flapping bending vibration of wind turbine blade not only decreases the energy efficiency of the whole system, but also accelerates

the speed of structure damage and fatigue, which results in a lot of loss. Therefore, building smart structures for wind turbine blades with high energy efficiency, structure health monitoring, and vibration control is a big challenge to the current development of wind turbine technology.

A typical horizontal axis wind turbine configuration is shown in Figure 1.1. The rotation of the rotor blades is driven by the external wind. Then the rotor blades rotate the shaft, which is connected with the electrical generator, so that electrical energy can be generated from the generator.

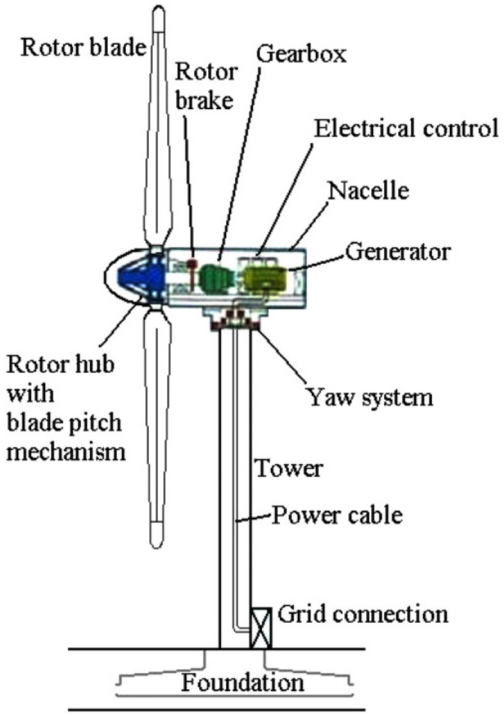

Figure 1.1 A typical configuration of a horizontal axis wind turbine [4]

Wind turbine blades are subject to deformation and vibration from a number of sources, such as the accumulation of particles like dust or ice, the external wind excitation, or the blade's own weight. Most wind turbine blades are fabricated using reinforced fiberglass composite materials. The most significant blade bending moments induced by external wind loads typically occur in flap-wise (out of blade plane) direction. Flap-wise forces have stochastic and deterministic components. The stochastic component is mainly due to the variability of wind speed and direction. The deterministic component is invariant, and increases with height. When the wind turbine blade is mounted high, a blade may twist or deform in directions perpendicular

to its length, or perpendicularly to the blade surface. This is often referred to as edge-wise bending.

The velocity variation over the rotor disc will also influence the blade and introduce both flap-wise and edge-wise fatigue damage on the blade, with moment fluctuations in the two directions. The flap-wise moments on the blade are the main cause for the rotor yaw and tilt moments. The edge-wise moments are less sensitive to the blade pitch than the flap-wise moments [5]. Therefore, the flap bending vibration is dominant and should be paid more attention.

In order to reduce the weight and cost of wind turbine, wind turbine blades and tower are both flexible thin-walled structures. Wang, *et al.* [6] analyzed the vibration of blades and tower by using thin-walled beam theory. Three forces are mainly found working on the blade, i.e., wind force, centrifugal force, and gravity force. Figure 1.2 shows the blade's two flap bending mode shapes, with the natural frequencies of 56.54Hz and 158.94Hz. The tower bending is strongly coupled with the blade flap bending, but it is independent of blade edge bending, because the dominant natural frequencies of tower vibration are designed to be far from the dominant natural frequencies of blade's flap vibration. Therefore, the influence of tower vibration on the blade's flap vibration is small. Since the external excitations from the wind loads will be most intense at the low frequency range, the first two flap bending mode shapes are dominant vibrations.

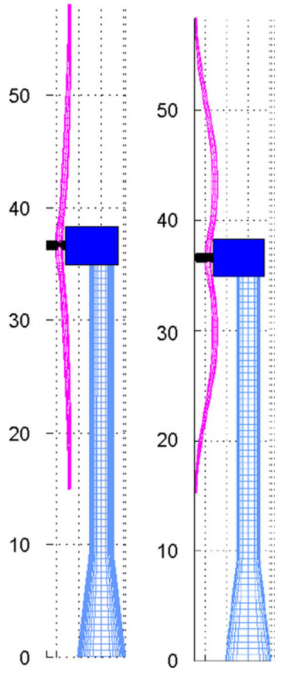

Figure 1.2 Blade's first two mode shapes of flap bending [6]

1.2.2 Structure health monitoring for wind turbine blades

In order to harvest wind energy more efficiently, the wind turbine blades are always designed large, which makes maintenance and repair works particularly difficult. In order to improve safety, to minimize down time, and to provide reliable power generation, the wind turbines must be monitored from time to time to ensure that they are in good condition. The self-excited vibrations caused by the aerodynamic instability is inevitable. The impact of vibrations on wind turbine blades should be paid much attention, because they generate noise, decrease the life of the blades, induce vibrations in the tower and other parts of the structure, causes structural

damage. Therefore, structure health monitoring and vibration control of wind turbine blades are crucial and significant for the wind turbine technology development.

The structural health monitoring (SHM) system is of primary importance to the whole wind turbine system, because structural damage may induce catastrophic damage to the integrity of the system. A SHM system is very useful in tackling the fatigue issue of wind turbine blades, due to predicting the exact life of a wind turbine component is extremely difficult due to their long designed service life of 10–30 years. A reliable, low-cost SHM system is highly needed for the wind turbine system, since it will reduce wind turbine lifecycle costs and make wind energy more affordable.

Since the wind turbine blade is the key element of a wind power generation system and the cost of the blades can account for 15–20% of the total turbine cost, extensive attention has been given to the structural health of blades [7]. Furthermore, rotating mass unbalance due to minor blade damage can cause serious secondary damage to the whole wind turbine system [8]. The locations at 30–35% and 70% along the length of the blade from the root section have been found more prone to damage [9]. Figure 1.4 illustrates the damage-prone locations on the blade, while Figure 1.5 shows an example of damage.

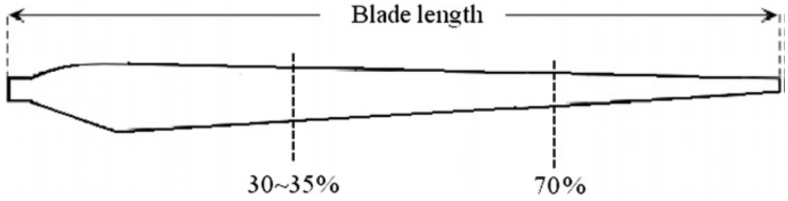

Figure 1.3 Locations of a wind turbine blade that is likely to damage [9]

Figure 1.4 An example of blade damage

Existing damage detection techniques for wind turbines include acoustic emission events detection method [10, 11], thermal imaging method [12], ultrasonic methods [13], modal-based approaches [14-17], fiber optics method [18], etc.

1.2.3 Vibration control in wind turbine blades

Many kinds of internal and external factors, such as wind turbulence, variety of wind speed, foundation vibrations due to environmental disturbances, etc., will cause the wind turbine blades having non-effective vibrations, including bending, and torsional vibrations. Moreover, the coupling effect among these non-effective vibrations makes the control of blade vibrations a big challenge.

Various active and passive vibration strategies have been applied for the vibration control of wind turbine blades. Veers, *et al.* [19] studied on a passive controller of using aero-elastic tailoring. It is concluded that it can provide either better power generation or vibration reduction, or both. Maldonado, *et al.* [20] presented an active vibration control method by using an array of synthetic jet actuators in a wind tunnel. Karaolis, *et al.* [21] introduced a method of using biased lay-ups in blade skins to achieve different types of twist coupling for wind turbine applications. Karaolis suggests that in addition to using the flapwise or centrifugal loading to twist a blade, it might be useful to internally pressurize a spar and use changes in the pressure to actively control the angle of blade twist. Kooijman [22] claimed that "the use of aeroelastic tailoring of the Fibre Reinforced Plastics to control limited torsional deformation is a promising way to improve rotor blade design." Dossing [23] presented a vibration control method on huge wind turbine blades by using tuned absorbers and identified the optimal design parameters. Laks, *et al.* [24] proposed a combined feel-forward/feedback control method, which can reduce the blade flap bending moments for wind turbine system.

1.2.4 Similarities with helicopter blades

Although the helicopter blades rotate around a vertical axis unlike the horizontal axis of wind turbine blades, its movement and vibration share some similarities with wind turbine blades. Helicopter rotor systems mainly consist of two or more equally spaced blades attached to a central hub. The blades are maintained in uniform rotational motion, usually by a shaft torque from the engine. As a response to the aerodynamic loads, helicopter blades undergo three basic deflections, flapping, lead-lag and pitching, which are shown in Figure 1.5. The out-of-plane

bending deflection (called flapping), and the in-plane bending deflection (called lead-lag) occur about the hinges and the pitching deflection occurs about a bearing. Like the wind turbine blades, the flap bending vibration in helicopter blades is the dominant vibration. The first three mode shapes of flap bending vibration of helicopter blade is as shown in Figure 1.6. It can be seen that the flap bending vibration is similar as the vibration of fixed-free cantilever beam.

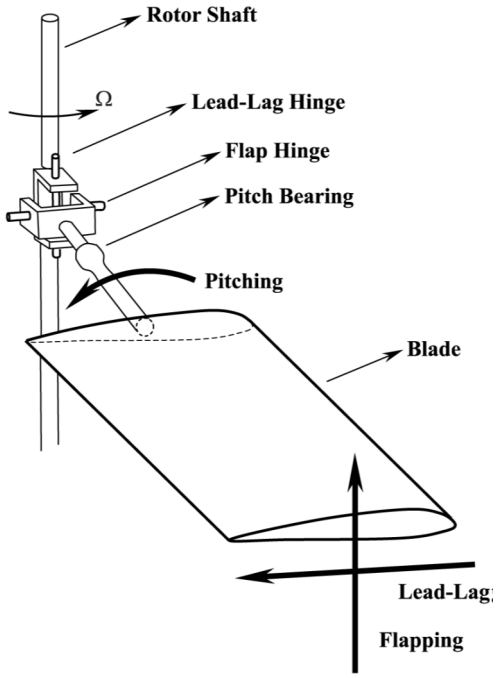

Figure 1.5 Helicopter rotor blade [25]

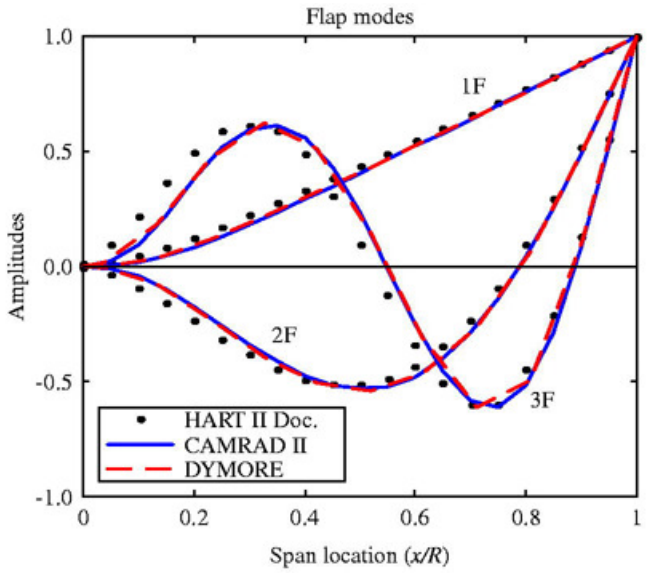

Figure 1.6 Mode shapes of flap bending vibration [26]

Many companies have conducted a lot of research on developing structure health monitoring sensors for helicopter application, such as MicroStrain company [27]. They designed an active radio frequency identification embedded usage tracking system for helicopter rotating components, as shown in Figure 1.7. Their objective is to develop a comprehensive and networked health management capability that can be embedded directly into rotorcraft components, with both functions of energy harvesting and structure health monitoring. They designed tiny, wireless energy harvesting radio frequency identification nodes that provide part identification, performance monitoring, on-board storage of component usage history, and remaining useful life.

Figure 1.7 MicroStrain's SHM sensors in helicopter application [27]

1.3 Piezoelectric Technology for Multifunctional Smart Structures

For energy harvesting, an electromechanical transducer is needed to convert mechanical energy to electrical energy. For structure health monitoring, a type of sensor, which can reflect the change of mechanical properties in the form of other kinds of detectable signal, such as electrical signal, is required. For vibration control, a sensor is needed to reflect the current vibration condition, and an actuator is required to conduct effective control performance. Based on the overall consideration of the three functions, piezoelectric material is a suitable choice as the transducer, sensor, and actuator for the multifunctional smart structure.

Over the past 50 years piezoelectric sensors have proven to be a versatile tool for the measurement of various processes. Today, they are used as sensors for measuring pressure, acceleration, strain or force in quality assurance, process control and development across many different industries. It has been successfully used in various critical applications, for example in medical, aerospace and nuclear instrumentation.

1.3.1 Background of Piezoelectric Technology

Piezoelectric material has two effects, i.e., direct piezo effect and inverse piezo effect, as shown in Figure 1.8. Direct piezo effect is: When an external force is applied on the piezoelectric material, either in compressing direction or stretching direction, electric charge will generate on the surface of the piezoelectric material. Direct piezo effect corresponds to the energy conversion from mechanical energy to electrical energy. With direct piezo effect, piezoelectric material can be used as sensor or energy harvester. Inverse piezo effect is: The application of an electric voltage to an unrestrained piezoceramic body results in its deformation. Inverse piezo effect corresponds to the energy conversion from electrical energy to mechanical energy. With inverse piezo effect, piezoelectric material can be used as actuator.

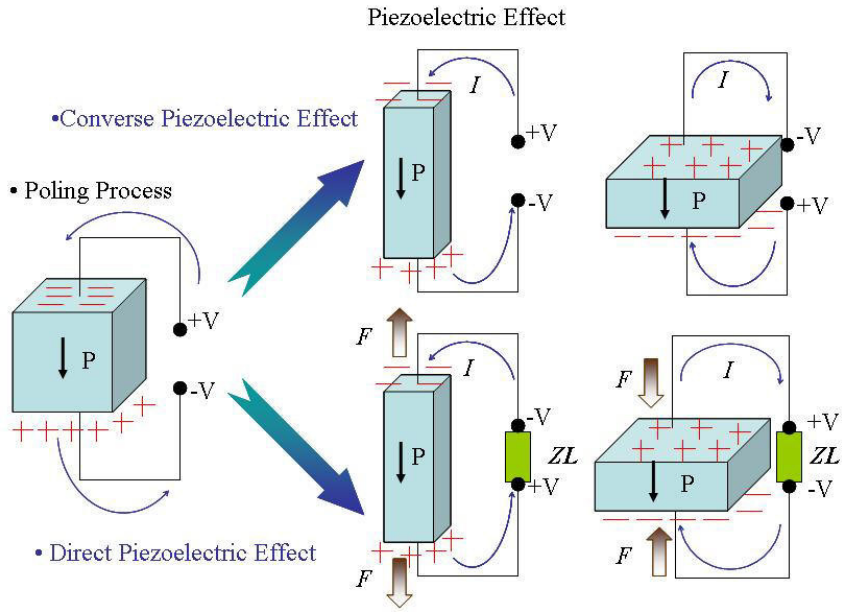

Figure 1.8 Piezoelectric effect [28]

Flexible piezoelectric materials are widely used for energy harvesting applications because of their ability to withstand large amounts of strain. Larger strains provide more mechanical energy available for conversion into electrical energy. A second method of increasing the amount of energy harvested from a piezoelectric is to utilize a more efficient coupling mode. There are two practical coupling modes, i.e., 31-mode and 33-mode, as shown in Figure 1.9. In the 31-mode, a force is applied in the direction perpendicular to the poling direction, an example of which is a bending beam that is poled on its top and bottom surfaces. In

the 33-mode, a force is applied in the same direction as the poling direction, such as the compression of a piezoelectric block that is poled on its top and bottom surfaces.

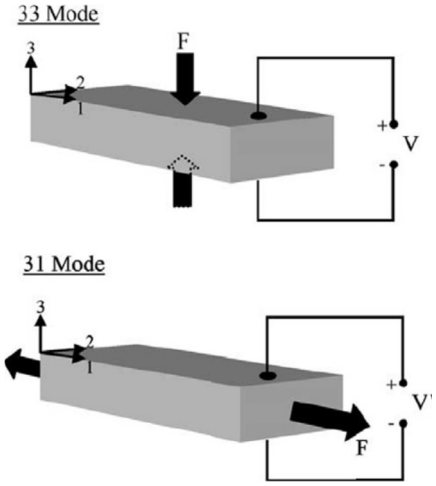

Figure 1.9 Two coupling modes of piezoelectric materials [29]

The electrical-mechanical coupling equations of piezoelectric materials are [30]

$$\begin{bmatrix} \boldsymbol{D} \\ \boldsymbol{S} \end{bmatrix} = \begin{bmatrix} \boldsymbol{\varepsilon^T} & \boldsymbol{d} \\ \boldsymbol{d^t} & \boldsymbol{s^E} \end{bmatrix} \begin{bmatrix} \boldsymbol{E} \\ \boldsymbol{T} \end{bmatrix} \tag{1.1}$$

where $\boldsymbol{D}$ is the electric charge density displacement, $\boldsymbol{E}$ is electric field strength, $\boldsymbol{S}$ is strain, $\boldsymbol{T}$ is stress, $\boldsymbol{\varepsilon^T}$ is permittivity in a constant stress field, $\boldsymbol{d}$ is the matrix for the direct piezoelectric effect, $\boldsymbol{d^t}$ is the matrix for the converse piezoelectric effect, $\boldsymbol{s^E}$ is compliance in a constant electric field.

Referring to the geometry of a typical piezoelectric material with three axes and six surfaces in Figure 1.10, the vectors of electric charge, electric field, strain, and stress can be expressed as, respectively,

$$\boldsymbol{D} = \begin{bmatrix} D_1 \\ D_2 \\ D_3 \end{bmatrix}, \ \boldsymbol{E} = \begin{bmatrix} E_1 \\ E_2 \\ E_3 \end{bmatrix}, \ \boldsymbol{S} = \begin{bmatrix} S_{11} \\ S_{22} \\ S_{33} \\ 2S_{23} \\ 2S_{13} \\ 2S_{12} \end{bmatrix} = \begin{bmatrix} S_1 \\ S_2 \\ S_3 \\ S_4 \\ S_5 \\ S_6 \end{bmatrix}, \ \boldsymbol{T} = \begin{bmatrix} T_1 \\ T_2 \\ T_3 \\ T_4 \\ T_5 \\ T_6 \end{bmatrix} \tag{1.2}$$

$$\boldsymbol{\varepsilon^T} = \begin{bmatrix} \varepsilon_{11}^T & 0 & 0 \\ 0 & \varepsilon_{22}^T & 0 \\ 0 & 0 & \varepsilon_{33}^T \end{bmatrix}, \ \boldsymbol{d} = \begin{bmatrix} 0 & 0 & 0 & 0 & d_{15} & 0 \\ 0 & 0 & 0 & d_{24} & 0 & 0 \\ d_{31} & d_{32} & d_{33} & 0 & 0 & 0 \end{bmatrix}, \ \boldsymbol{s^E} = \begin{bmatrix} s_{11}^E & s_{12}^E & s_{13}^E & 0 & 0 & 0 \\ s_{12}^E & s_{11}^E & s_{13}^E & 0 & 0 & 0 \\ s_{13}^E & s_{13}^E & s_{33}^E & 0 & 0 & 0 \\ 0 & 0 & 0 & s_{55}^E & 0 & 0 \\ 0 & 0 & 0 & 0 & s_{55}^E & 0 \\ 0 & 0 & 0 & 0 & 0 & s_{66}^E \end{bmatrix} \tag{1.3}$$

The voltage generated from the piezoelectric transducer is always an AC signal. In order to store the electrical energy in an energy storage unit (mainly using rechargeable batteries or super-capacitors), it is necessary to rectify AC signal to DC signal. Therefore, the energy harvesting circuit connected with the piezoelectric transducer is as shown in Figure 1.11.

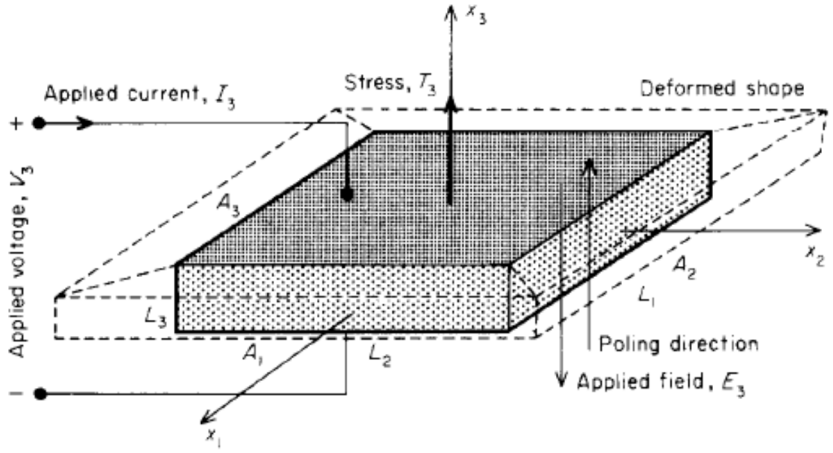

Figure 1.10 Geometry of a typical piezoelectric material [31]

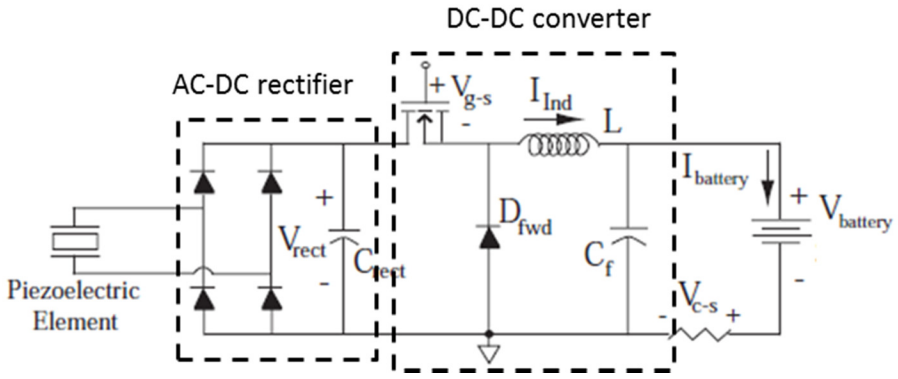

Figure 1.11 Typical energy harvesting circuit

1.3.2 Piezoelectric-based Energy Harvesting

Over the past decade there has been an abundant increase of interest in self-powered devices in the engineering applications like MEMS, continuous structural health monitoring,

environmental monitoring, portable electronics, etc. Practical solutions for the power supply of the electronic devices have been developed. Energy harvesting from ambient sources, such as mechanical vibrations, is a very promising alternative. One of the most efficient ways of harvesting vibration energy is piezoelectric transduction [32, 33].

Researchers already developed various kinds of piezoelectric energy harvesters. One early study into energy harvesting developed a piezoelectric energy harvesting system mounted in shoes, which can harvest energy during walking and use it to power a radio transmitter [34]. The energy harvesting shoe is shown in Figure 1.12. The device has a piezoceramic composite material located in the heel and a multilayer polyvinylidene difluoride (PVDF) foil laminate patch located in the sole of the shoe. The average power generated from both the PVDF and the piezoceramic composite material was estimated approximately 1 and 2 mW, respectively. Another example is an integrated piezoelectric vibration energy harvester and wireless temperature & humidity sensing node designed in 2005 [35], as shown in Figure 1.13, which is comprised of a microprocessor, on-board memory, strain sensing gauge and sensor signal conditions. It is claimed that the piezoelectric strain energy harvesting system can deliver around 2000mW under low level vibration conditions.

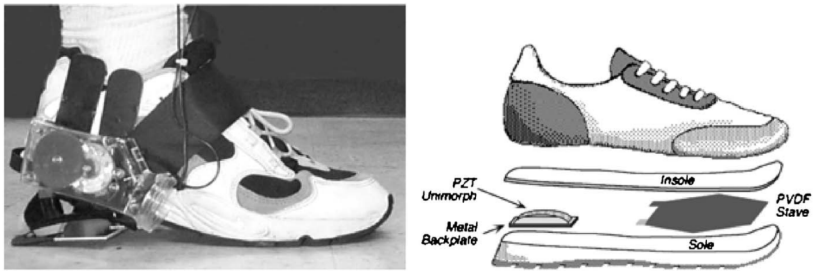

Figure 1.12 Energy harvesting shoe [34]

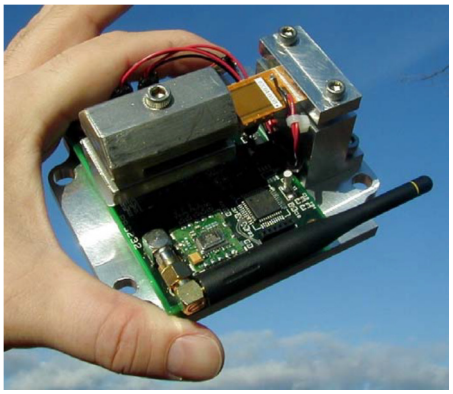

Figure 1.13 Integrated system of wireless sensor node and piezoelectric energy harvester [35]

Vibration-based energy harvesters generate the maximum power when the excitation frequency matches their resonance frequency. Under many circumstances, we know the excitation frequency before we design, so that we can design devices to have the appropriate resonance characteristics. In other situations, however, we either don't know excitation frequency a priori or it might change over time. A type of design that can operate effectively over a range of vibration frequencies would be required. Therefore, many researchers work on the frequency-tuning methods. Eichhorn, *et al.* [36] presented a piezoelectric generator, whose resonance frequency can be tuned by applying mechanical stress to its structure. The harvester is comprised of a cantilever beam with two arms connected to the tip of the beam. By applying different force to the arms, stress in the main part of the beam can be altered accordingly, which leads to a shift of its resonance frequency. Challa, *et al.* [37] designed a tunable energy harvesting device using a magnetic force technique, as shown in Figure 1.14, with two magnets, i.e., one is above the vibrating structure, and the other is below the vibrating beam. The design enables either an increase or decrease in the tuned resonant frequency. Kozinsky [38] designed a passive self-tuning resonator for broadband power harvesting by using a mechanical resonator with a mass that is free to move along its length. It adapts its resonant frequency to the drive as the mass moves to find the minimum potential energy.

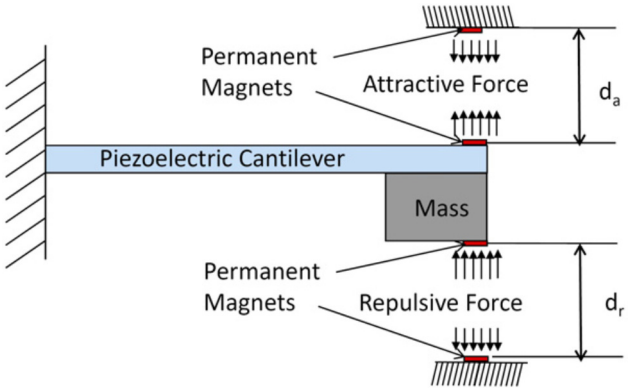

Figure 1.14 Schematic of the resonance frequency tunable energy harvesting device [37]

The traditional piezoelectric vibration energy harvesters are composed of a cantilever beam with a proof mass at the tip to increase the power output and also reduce the operating frequency. These traditional vibration-powered converters provide maximum output only when being operated close to resonant frequencies [39]. But this condition is difficult to guarantee since the ambient excitation/vibration is not controllable or intrinsically frequency-variant over a

broad bandwidth. In order to improve the efficiency, people have developed many methods, like the impedance matching between the piezoelectric transducer and the electrical load by Kong, *et al*. [40], Liang and Liao [41], and Chen, *et al*. [42]. Badel, *et al*. [43] augmented the harvester with an electrical switching device, in which the switch is triggered in a special manner to maximize the output voltage of the harvester.

Whereas, in order to overcome the narrow bandwidth problem, many methods have been developed, Sari, *et al.* [44] and Ferrari, *et al.* [45] used multiple piezoelectric cantilever beams with different natural frequencies closer to each other. Qi, *et al.* [46], and Xue, *et al.* [47] designed a multiresonant piezoelectric beam by attaching multiple cantilever beams of natural frequencies close to the first resonance of the primary beam. Roundy and Zhang [48], Leland and Wright [49] and Eichhorn, *et al.* [50] actively tuned the operating frequency of power harvesting device by applying an electrical input or axial load to piezoelectric bimorph. Xu, *et al.* [51] considered the interaction of harvester with L-shaped flexible structure to harvest the energy from two modes thereby improving the harvester efficiency. Yang, *et al.* [52] and Le, *et al.* [53] used multiple masses at different locations of the beam to harvest energy at the first and second natural frequencies. Recently, Yang and Yang [54] used a new type harvester deigned with two PZT beams coupled with variable elastic spring to improve the bandwidth by sacrificing the power.

1.3.3 Piezoelectric-based Structure Health Monitoring (SHM)

Piezoelectric-based structure health monitoring can be mainly divided into three categories: guided-wave-based method, impedance-based method, and vibration-based method. Due to their advantages and disadvantages, they are suitable for different conditions.

(1) Guided-wave-based SHM

Guided-wave SHM always consists of an actuator and a receiver, the actuator generates guide waves with some high-frequency pulse signal that propagates in the structure, while the receiver senses the wave signal. The structural discontinuity due to damage in the structure can be detected by the deformed guided wave signals. However, in order to distinguish between damage and structural features, prior information is required about the structure in its undamaged state [55]. PZT has been widely adopted for guided-wave SHM technology [56, 57]. Wilcox, *et al.* [58] investigated the use of circular and linear arrays using piezoceramic-disk actuators and linear arrays using square shear piezoceramics for long-range guided-wave SHM in isotropic

plate structures. Signal processing is a crucial process in guide-wave SHM. The objective is to extract information from the sensed signal to decide if damage exists in the structure. Signal processing approaches can be grouped into data cleansing, feature extraction and selection, pattern recognition, and optimal excitation signal construction.

(2) Impedance-based SHM

Impedance-based structural health monitoring techniques have been developed as a promising tool for real-time structural damage assessment, and considered as a new nondestructive evaluation method. A key aspect of impedance-based structural health monitoring is the use of piezoceramic materials as a collocated sensors and actuators [59]. Impedance or admittance-based structure health monitoring technology was widely proven to be an effective method to detect the damages [60-66]. It is typically applied for the excitation frequency of higher than 30 kHz. By attaching a piezoelectric transducer on the host structure, the mechanical impedance of the host structure can be directly reflected by the electrical impedance measured from the piezoelectric transducer. Since the damages in the host structure will often change the stiffness or mass of the structure, the mechanical impedance of damaged structures will be different from the original one. Therefore, the damage can be detected by monitoring the electrical impedance or admittance from the piezoelectric transducer.

Due to the high frequency measurement, the impedance or admittance-based damage detection technology is capable to detect to small-size damages in various structures. Based on the spectral analysis method, Wang and Tang [67] proposed a model-based approach that can identify both the location and the severity of the damage. However, in the laboratory setting, the conventional impedance or admittance-based methods are of high cost and huge size due to the heavy and expensive impedance analyzers, and thus are difficult to implement in fields [68]. In recent years, low-cost high-sensitive impedance measurement circuits and embedded systems have been proposed, which make impedance or admittance-based technology more practical and popular. Bhalla, *et al.* [69] used one piezoelectric as an actuator and the other one as a sensor, across which the voltage is measured. This method only needs a signal generator and a signal analyzer. Peairs, *et al.* [70] proposed a low cost impedance based method by measuring the voltage drop across a resistor that is connected serially with the piezoelectric transducer, since the electrical current can be obtained due to the voltage excitation, leading to the impedance or

admittance. The method enables online monitoring, since the signal generation and FFT algorithm can be programmed onto a small-size digital signal processing unit.

Based on Peairs, *et al.* [70]'s low cost measurement circuit, Wang and Tang [71] introduced an inductive circuitry to the electromechanical system by connecting a tunable inductor, a resistor and the piezoelectric element in series, as shown in Figure 1.15. The serial connection of the inductor and the piezoelectric capacitor creates an additional frequency resonant to the mechanical structure. It can greatly increase the admittance magnitude and the admittance sensitivity. The peak admittance magnitude with the inductive circuitry is increased by 28dB when comparing with the traditional one without the inductance, i.e., first-order circuit system. The admittance change is increased by 17, 25, and 33dB for the damage severity level of 0.2%, 1%, and 3%, respectively. They also introduced a negative capacitor to the electromechanical system [72], which can broaden the circuitry resonance to a much wider frequency range, so that the admittance magnitude is increased in a much wider frequency range.

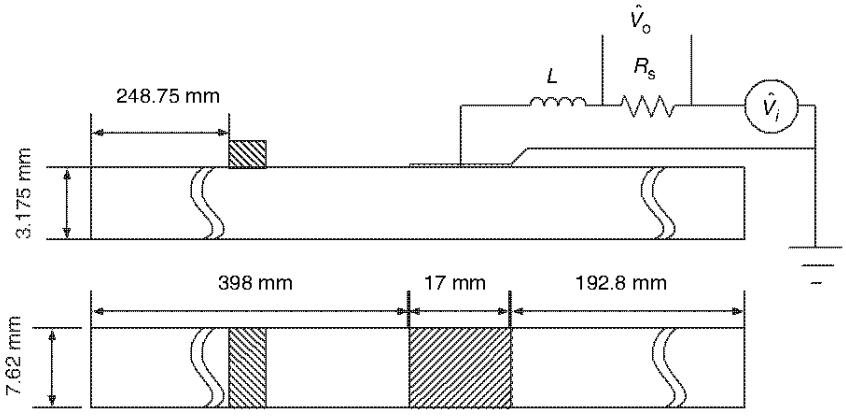

Figure 1.15 Admittance-based SHM with inductive circuitry [71]

(3) Vibration-based SHM

Vibration-based SHM can be classified to the following categories:

(1) Frequency changes. Many researchers studied on shifts in resonant frequencies for damage detection [73-76]. The changes in structural properties due to damage will cause changes in vibration frequencies, which is the principle of using modal methods for damage identification and health monitoring. However, since the frequency shifts to damage has very low sensitivity, it requires either very precise measurements or large levels of damage. An effective way is using multiple frequency shifts measured at different locations to detect the existence of damage. It can

provide spatial information about structural damage because changes in the structure at different locations will cause different combinations of changes in the modal frequencies.

(2) Mode shape changes. West [77] presented a method using of mode shape information for the location of structural damage. Ratcliffe [78] proposed a technique for locating damage in a beam that uses a finite difference approximation of a Laplacian operator on mode shape data. Skjaeraek, *et al.* [79] studied on the optimal sensor location issue for detecting structural damage based on changes in mode shapes and modal frequencies.

(3) Mode shape curvature changes. An alternative to using mode shapes to obtain spatial information about sources of vibration changes is using mode shape derivatives, such as curvature. Pandey, *et al*. [80] concluded that the damage in the structure can be reflected by the absolute changes in mode shape curvature. Topole and Stubbs [81] investigated on using a limited set of modal parameters for structural damage detection.

(4) Methods based on dynamically measured flexibility. Because the flexibility matrix is defined as the inverse of the static stiffness matrix, the flexibility matrix relates the applied static force and resulting structural displacement. Thus, each column of the flexibility matrix represents the displacement pattern of the structure associated with a unit force applied at the corresponding degree of freedom.

(5) Methods based on updating structural model parameters. It is based on the modification of structural model matrices such as mass, stiffness, and damping to reproduce as closely as possible the measured static or dynamic response from the data.

1.3.4 Piezoelectric-based Vibration Control

Vibration control methods are roughly categorized into two groups, active and passive methods. Active vibration control methods usually yield high-performance vibration suppression. However, active control systems need an external energy supply to suppress vibration. Passive vibration control methods use energy dissipative mechanisms such as dampers, frictional devices, and electric resistors. Passive methods do not need an energy supply, so they are always stable.

With its unique electromechanical coupling characteristics, piezoelectric materials are widely used in the vibration energy harvester, especially for microelectronics [82], wireless sensor nodes [83], etc. Sodano et al. [84] and Galhardi et al. [85] reviewed the piezoelectric-based energy harvesting technologies and applications. There are also a lot of interesting designs

of energy harvesters by using piezoelectric materials. Feenstra et al. [86] designed an energy harvesting backpack by employing a mechanically amplified piezoelectric stack. Howells [87] developed four proof-of-concept heel strike units to convert mechanical motion into electrical energy from the hells of boots.

The vibration control of a flexible structure by using piezoelectric materials has become an important topic in the past two decades. Halim et al. designed and experimentally evaluated the performance of a feedback controller based on the spatial H2 control [88] and the spatial H∞ control [89] to suppress vibration of a flexible beam. They also presented some resonant controllers to minimize the structural vibration using collocated piezoelectric actuator-sensor pairs [90]. Han et al. [91] utilized a LQG control algorithm and classical control methods to reduce the vibration level of lightweight composite structures. Baz and Poh [92] presented a modified independent modal space control method to select the optimal location, control gains and excitation voltage of the piezoelectric actuators for vibration control of a flexible beam. Narayanan and Balamurugan [93] showed that a LQR approach is more effective in vibration control than constant-gain negative velocity feedback in active vibration control with distributed sensors and actuators for piezo-laminated smart structures. Scruggs [94] presented a H2 control-based approach to maximize the power generation in the energy harvesting system, so that the harvested energy is maximal in constrain of minimized vibration.

Based on the electromechanical characteristics of piezoelectrics, electrical circuit design has also attracted many researchers' interest to the control implementation of the structural vibration. Caruso [95] analyzed three different electric shunt circuits, i.e., RL series shunt circuit, RL-C parallel shunt circuit, and RL parallel shunt circuit, in piezoelectric passive vibration damping. Behrens et al. [96] designed a negative capacitance controller to reduce the structural vibration in a broadband frequency range. Ottman et al. [97] presented a method of using step-down dc-dc converter (buck converter) to optimize piezoelectric energy harvesting by finding the optimal duty cycle. Lefeuvre et al. [98] got the equivalent relation between buck-boost converter with a certain duty cycle and resistance, so that buck-boost converter can be used to obtain optimized piezoelectric energy harvesting. The buck-boost converter method of finding optimal duty cycle to make the dc-dc converter be equivalent to optimal resistance is an effective way to get optimal power output. Fleming and Moheimani presented a method for online adaptation of the shunting impedance by minimizing the RMS strain [99], or minimizing the

relative phase difference between a vibration reference signal and the shunt circuit [100], or using LQG, H2, and H∞ control algorithms [101]. Guyomar et al. [102, 103] proposed the synchronized switch damping (SSD) to efficiently suppress the structural vibration. Li et al. [104] extended an improved SSD technique based on an energy transfer scheme to damp the vibration of the target structure. However, regarding control method, the buck-boost converter or SSD method is essentially a passive or semi-active control, the control performance of which is not as good as active control.

The synchronized switch method [105, 106] has a limitation that it only works for sinusoidal vibration, since the voltage converting process only occurs when the displacement of the structure attains the maximum or minimum. However, random vibration exists even more widely than sinusoidal vibration in reality. A universal vibration control method for all the kinds of vibrations, including random vibration, sinusoidal vibration, etc., is highly required. Moreover, the implementation of self-powered control is also a challenge.

1.3.5 Interactions among the three aspects

The above mentioned three piezoelectric-based technologies, i.e., energy harvesting, structure health monitoring, and vibration control, are not independent areas. There are interactions between each other. Due to the limited life span of batteries, researchers have paid more and more attentions on building self-powered structure health monitoring sensors and self-powered vibration control units, especially for the application in remote areas where the replacement of batteries is very difficult.

The technology of self-powered wireless sensor node for structure health monitoring has attracted a lot of attention [107, 108]. Delebarre, *et al.* [109] studied the feasibility of developing a structure health monitoring system having a double functionality, i.e., damage detection and energy harvesting in order to be fully autonomous. Zhu, *et al.* [110] built a low-profile, planar, self-powered intelligent sensor device (known as smart tag) for the use of wireless structure health monitoring in aeronautical applications, as shown in Figure 1.16. It can be fabricated within a composite material and embedded in the structure of an aircraft to monitor structural health and transmit measurement data wirelessly to the base station during the flight. Piezoelectric material is used as the energy generator.

There are also many researches on self-powered vibration control technology [111, 112]. Lallart and Guyomar [112] presented a low-power and self-powered piezoelectric vibration

control method based on a nonlinear approach. They presented a simple nonlinear processing method of the output voltage of piezoelectric elements, resulting in an increase of the piezoelectric electromechanical coupling coefficient which can reduce the mechanical energy, leading to a damping effect in terms of mechanical vibrations. Shimose, *et al.* [113] designed and compared both analog and digital self-powered systems for multimodal vibration suppression. Both types of the controllers do not require external energy. Konak, *et al.* [114] proposed a method of a self-powered discrete time piezoelectric vibration damper which does not need tuning to the structural resonant frequency and is powered by the piezoelectric elements.

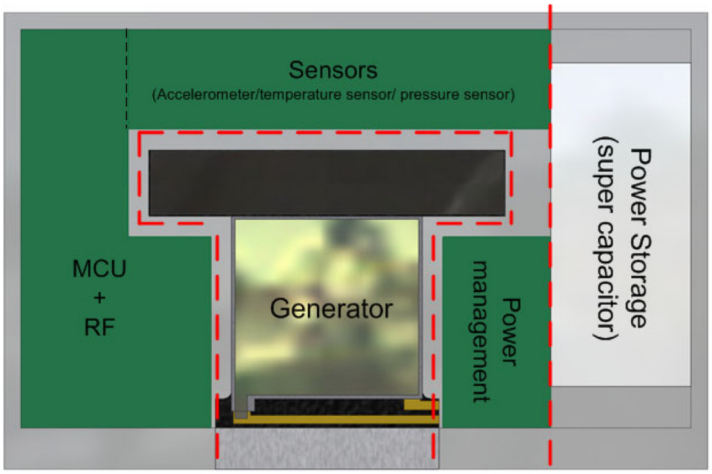

Figure 1.16 Layout of smart tag [110]

Few studies have been focused on multifunctional smart structures with both the functions of damage detection and vibration control. However, Ray, *et al.* [115] presented a towards multifunctional smart structure method of damage detection and vibration control in smart plates, in which the sensitivity of modal frequency shifts due to realistic damage cases has been enhanced, and it shows the potential of using the same piezoelectric sensors and actuators for implementing vibration damping control.

1.4 Objectives and Contributions of This Dissertation

An integrated multifunctional smart structure is highly required, because there are a lot of applications where energy, structural health, and vibration of host structure are all concerned. For example, for aircraft application, battery-free is a research target in order to reduce the weight of the aircraft as much as possible to improve the gas-efficiency. The structural health should be monitored to guarantee the aircraft operating in a safety situation, especially for aged aircrafts.

The large amount of vibration in the aircraft body will accelerate the generation of cracks and make the whole aircraft system consume more energy. Thus, the control of vibration of aircraft during flight is also very important. Therefore, the multifunctional smart structure is a necessary and significant technology for the aircraft application. Another application of the multifunctional smart structure is wind turbine. The aging of the blades in wind turbine requires a real-time damage detection method to monitor the safety of the structure. Wind turbine is a kind of device generating electrical energy by being rotated by wind. Only the rotational motion is effective, that is to say, the other kinds of motions, such as flap bending vibration, should be minimized to save more energy and improve the efficiency. Thus, vibration control is also necessary for wind turbine. The function of wind turbine is harvesting wind energy to electrical energy. If efficient energy harvesters can be designed to harvest the non-effective vibration of wind turbine blades, not only more energy can be harvested, but also the non-effective vibration can be attenuated.

The intellectual merits and impacts of designing a multifunctional smart structure with functions of energy harvesting, structure health monitoring, and vibration control include: (1) The knowledge in each of the three aspects can be explored, since novel methods in the three aspects will be proposed and investigated. Hopefully, an efficient piezoelectric energy harvester, which has a broad bandwidth and has a potential to harvest more energy than the traditional ones, will be designed for general applications. An effective damage detection method with higher detection sensitivity will be presented, which can detect small cracks even invisible inside the structure. A novel vibration control method which can reduce the mechanical energy resulting in decreased vibration, and harvest the reduced energy to electrical energy for self-power use or other energy use; (2) The connections and interactions among the three aspects will be bridged and new interdisciplinary knowledge will be established. Due to the electromechanical characteristics of piezoelectric, the technology involves many disciplines, including dynamics, mechanism, electronics, circuit design, etc.. Many mechanical properties of structures can be reflected from the electrical parameters the piezoelectric transducer or the external circuit connected to the piezoelectric transducer; (3) The technology will exert an unprecedented improvement for aerospace, civil, mechanical infrastructure applications. Many applications require this kind of multifunctional smart structure to achieve multiple functions at the same time, such as aircraft wings, wind turbines, etc.. Taking the aircraft application as an example, the wings of the aircraft can be made of the multifunctional smart structures, so that the

processes of damage detection and vibration control of the aircraft wings can be proceeded during the flight, with the harvested energy as the power supply for the two functional units. Therefore, damage situations, such as existence of cracks in the wings, can be detected on time. Some kinds of real-time fixing actions can be made to avoid dangerous risks.

Therefore, the objective of this study is designing smart structures with one or more functions of energy harvesting, structure health monitoring, and vibration control. The interactions among the three aspects are shown in Figure 1.17. The integrated smart structure can be applied for wind turbine blades, helicopter blades, aircraft wings, bridges, and other mechanical infrastructures.

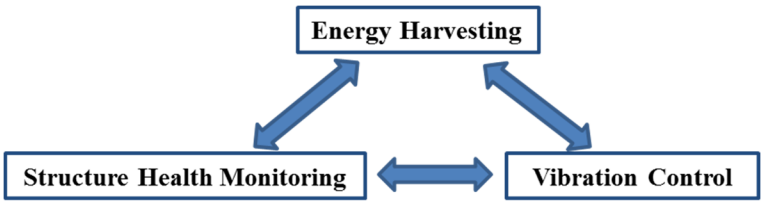

Figure 1.17 Relationship among the three aspects

The specific objectives for the three aspects include:

(1) Designing a high-efficient piezoelectric energy harvester which can harvest energy in a broad bandwidth of frequencies.

(2) Designing various kinds of piezoelectric stack energy harvesters with different force amplification frames, with high power density and energy conversion efficiency.

(3) Proposing an efficient structure health monitoring method which has the capability of detecting small damages in mechanical structures. By comparing with the existing damage detection methods, the proposed method should have higher damage detection sensitivity.

(4) Presenting a self-powered vibration control system which can both decrease the vibration of the host structure and at the same time harvest energy. Based on the energy equilibrium principle, the reduced mechanical energy, which suppresses the structural vibration, can be harvested as electrical energy.

(5) Developing a vibration and wave propagation attenuation method for metamaterials with periodic piezoelectric arrays, with broader vibration attenuation bandwidth.

The dissertation project has the following merits: (1) It improves the interdisciplinary development, since it involves concepts of mechanical engineering, electrical engineering, and civil engineering. The primary focus is on dynamics, vibration, mechatronics, etc.. It will bridge

different areas and create new knowledge in the interdisciplinary area. (2) It has potentiality to revolutionize the design of multifunctional smart structures. The knowledge of tuned mass damper (TMD) will be integrated into the design. TMD has the characteristics of decreasing the vibration of the host structure and increasing the vibration of the tuned mass damper itself. It is a revolutionary way to harvest more energy and reduce vibration of host structure. (3) The technology of multifunctional smart structure with functions of energy harvesting, structure health monitoring, and vibration control has a broad applications. A specific application is for aircraft wings. The energy harvested from ambient vibration during flights can be used to power damage detection units and vibration control units. Especially for unmanned aircrafts, the feature of battery-free can reduce a lot of the weight of the aircraft, which is very important for the unmanned aircrafts.

1.5 DISSERTATION ORGANIZATION

Chapter 2 presents and investigates a novel piezoelectric-based energy harvester with double-beam structure, which broadens the bandwidth and significantly increases the energy harvested from the ambient vibration. Chapter 3 presents the energy harvesting technologies from multilayer PZT ceramic stack with force amplification frame. Chapter 4 presents and investigates an admittance-based damage detection method with high-order resonant circuit, which greatly improves the signal-to-noise ratio and increases the damage detection sensitivity. Chapter 5 presents and investigates a self-powered vibration control system for flexible structures, with both functions of minimizing the structure vibration and harvesting energy. Chapter 6 presents a vibration and wave propagation attenuation method for metamaterials with periodic piezoelectric arrays shunted by high-order resonant circuit, which can generate broader attenuation bandwidth or produce two separate bandgaps. Chapter 7 states the conclusion.

Chapter 2 Efficient Vibration Energy Harvester with Multi-mode Dynamic Magnifier

2.1 MOTIVATION

Though relative few, some research methods were developed to achieve both enhancing power/efficiency and widening the bandwidth of the operation. Cornwell et al. [116] connected the tuned energy harvester as an auxiliary beam to a three-story building like structure and magnified the power over a wider bandwidth around the first natural frequency. Recently, Ma, *et al.* [117], Aldraihem and Baz [118] and Aladwani, *et al.* [119] proposed a dynamic magnifier to increase the power output and widen the bandwidth around a single resonance using an additional mass with spring between the harvester and the vibration base. Tang and Zuo [120] gave an analytical solution of parameter optimization for the dual-mass energy harvesting system for enhanced energy harvesting. However, harvesters with dynamic magnifier in all literature above [116-120] only perform well around the first natural frequency region. In this paper we propose new type of harvester with a multiple mode dynamic magnifier which is able to enhance the power and widen the operation bandwidth over virtually all natural frequencies of the harvesting beam. The idea is to tune all the modes of the beam harvester to the modes of the intermediate beam connected between the vibration base and the harvesting beam. Therefore, all the vibration modes of the harvester beam will be magnified by the resonances of the intermediate beam.

This concept of the coupled beams can also be extended and is applied to multi-mode vibration damping, which offer significant advantage over the traditional Tuned Mass Damper (TMD). The typical TMD is composed of a spring, mass and damper to damp only one mode of the vibration [121, 122]. Den Hartog [121] developed the analytical frequency and damping tuning rules of the mass and damper using the fixed-point method for the SDOF TMD. For better vibration mitigation, multiple TMDs were also proposed [123, 124], where each absorber is tuned near the resonance of a single DOF primary system in parallel. Zuo and Nayfeh [125, 126] proposed multiple-DOF TMD and series TMDs, which are proved more effective than traditional or parallel TMDs for single mode vibration. To damp more than one mode of a MDOF primary system, usually several SDOF TMDs were used [127, 128], of which each one is tuned to the individual modes of the primary structure. Zuo and Nayfeh [129, 130] also proposed a MDOF TMD, and experimentally demonstrated that a single (rigid) reaction mass with multiple degrees

of freedom can be used to damp as many as six modes of the primary system. The concept proposed in this paper is actually an infinite DOF continuous TMD (beam) which can damp virtually all the modes of the primary beam structure is designed properly.

2.2 PRELIMINARY DESIGN

The concept of dynamic magnifier is essentially a dual of the tuned mass damper, where in the former case an intermediate mass is inserted between the vibration base and the vibration harvester system to amplify the vibration of the harvester Figure 2.1a, and in the latter case Figure 2.1b an auxiliary mass is attached to primary structure to reduce the vibration of the primary structure.

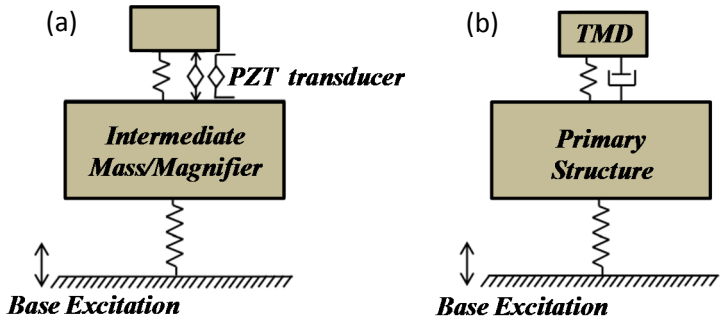

Figure 2.1 (a) Energy harvester with single-mode dynamic magnifier, (b) Classic TMD for a structure

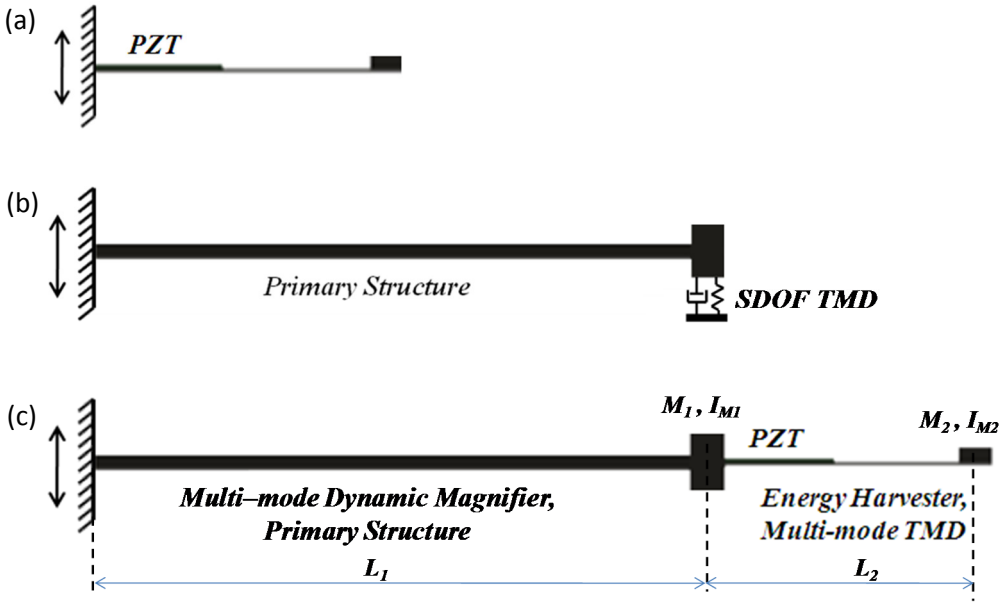

Figure 2.2 (a) A typical energy harvester, (b) the classical TMD for a beam, and (c) the proposed multi-mode double-beam harvester or TMD

A typical harvester is composed of a cantilever beam with tip mass at the end and PZT film on the beam surface, which operate mainly around the first natural frequency (Figure 2.2a). A traditional TMD is composed of a single-DOF mass attached to the primary structure to reduce the dynamic response near the TMD resonance. Figure 2.2b shows the TMD to suppress one vibration mode of a beam. The proposed vibration energy harvester with multi-mode dynamic magnifier or multi-mode TMD is shown in Figure 2.2c. Please note that though a similar double beam configuration has been used for harvester by Baz [131] and beam-type of TMD has been investigated by Dahlberg [132], they only consider a single mode of the system. Our innovation here is to take advantage of the fact that the beams have infinite vibration modes as the mechanism of energy harvesting and vibration control.

An intuitive is to design the two beams with tip masses having the same natural frequencies. So, we firstly treated them as two separate beams for the preliminary design to develop some guideline. A more accurate modeling and analysis is presented in the next section.

The mode shape of a uniform beam [133] is

$$W(x) = C_1\cos(\beta_n x) + C_2\sin(\beta_n x) + C_3\cosh(\beta_n x) + C_4\sinh(\beta_n x) \tag{2.1}$$

The corresponding natural frequency ω_n of the nth mode is

$$\omega_n = {\beta_n}^2\sqrt{\frac{EI}{\rho A}} \quad , \quad n = 1, 2, 3, \cdots \tag{2.2}$$

where E is the Young's modulus, I is the area moment of inertia; ρ is the beam density; A is the cross-section area of the beam, and $C_1 \sim C_4$ are constants dependent on the boundary conditions.

For the cantilever beam with a tip mass, the boundary conditions for the two ends are

$$W(x)|_{x=0} = 0 \tag{2.3}$$

$$\frac{dW(x)}{dx}|_{x=0} = 0 \tag{2.4}$$

$$EI\frac{d^2W(x)}{dx^2}|_{x=L} = 0 \tag{2.5}$$

$$-\frac{d}{dx}\left[EI\frac{d^2W(x)}{dx^2}\right] = {\omega_n}^2 MW(x)|_{x=L} \tag{2.6}$$

where L is the length of the beam, and M is the mass of the tip mass.

Substituting Eq. (2.1) and Eq. (2.2) into Eqs. (2.3)~(2.6), the following equation can be obtained.

$$\frac{M}{m}\alpha_n(sin\alpha_n cosh\alpha_n - sinh\alpha_n cos\alpha_n) = 1 + cos\alpha_n cosh\alpha_n \tag{2.7}$$

where

$$\alpha_n = \beta_n L \tag{2.8}$$

m is the mass of the beam.

Substituting Eq. (2.8) into Eq. (2.2), we obtain the natural frequency of a uniform beam of thickness t and b

$$\omega_n = (\frac{\alpha_n}{L})^2 \sqrt{\frac{EI}{\rho A}} = (\frac{\alpha_n}{L})^2 \sqrt{\frac{E\frac{1}{12}bt^3}{\rho bt}} = (\alpha_n)^2 \frac{t}{L^2}\sqrt{\frac{E}{12\rho}} \tag{2.9}$$

Therefore, as long as the mass and dimensions satisfy

$$\frac{M_1}{m_1} = \frac{M_2}{m_2} \tag{2.10}$$

and

$$\frac{\mathrm{t_1}}{\mathrm{L_1}^2}\sqrt{\frac{\mathrm{E_1}}{\rho_1}} = \frac{\mathrm{t_2}}{\mathrm{L_2}^2}\sqrt{\frac{\mathrm{E_2}}{\rho_2}} \tag{2.11}$$

the two cantilever beams will have the same natural frequencies and mode shapes.

If the two uniform beams are made of the same material, the Eq. (2.11) becomes

$$\frac{t_1}{{L_1}^2} = \frac{t_2}{{L_2}^2} \tag{2.12}$$

2.3 THEORETICAL ANALYSIS OF COUPLED DOUBLE-BEAM STRUCTURE

In the previous section, we consider the two beams independently and develop some approximate design guideline making these two beams have the same natural frequencies. Such a guideline will reasonably work if the second beam is much smaller than the first beam. Generally, when the two beams are coupled together as shown in the Figure 2.2c, the double beam structure will have natural frequencies different from that of the independent beams. In this section, an analytical modeling is created to calculate the mode frequency and mode shapes of the coupled double-beam structure, so as to understand the multimode dynamic magnifier or multi-mode TMD.

The equation for the mode shapes of the double beam structure is

$$W(x) = W_1(x)H(L_1 - x) + W_2(x - L_1)\,H(x - L_1) \tag{2.13}$$

where $H(x)$ is a unit step function, $W_1(x)$ and $W_2(x)$ are the shapes of the multi–mode dynamic magnifier (intermediate beam) and energy harvesting beam, respectively.

$$W_1(x) = C_1\cos(\beta_{1n}x) + C_2\sin(\beta_{1n}x) + C_3\cosh(\beta_{1n}x) + C_4\sinh(\beta_{1n}x) \tag{2.14}$$

$$W_2(x) = D_1 cos(\beta_{2n}x) + D_2 sin(\beta_{2n}x) + D_3 cosh(\beta_{2n}x) + D_4 sinh(\beta_{2n}x) \tag{2.15}$$

where β_{1n} and β_{2n} are defined similarly as Eq. (2.2).

At the n[th] vibration mode of the coupled structure, we have $\omega_{1n} = \omega_{2n} = \omega_n$, so the following relationship can be obtained for two uniform beam of the same materials.

$$\beta_{1n}^2 t_1 = \beta_{2n}^2 t_2 \tag{2.16}$$

If we choose the beam thickness-length according to Eq. (2.12), we have

$$\beta_{1n} L_1 = \beta_{2n} L_2 \tag{2.17}$$

The double-beam system will have the following boundary conditions at $x = 0$, and L_2

$$W_1(x)|_{x=0} = 0 \tag{2.18}$$

$$\frac{dW_1(x)}{dx}|_{x=0} = 0 \tag{2.19}$$

$$EI_2 \frac{d^3W_2(x)}{dx^3}|_{x=L_2} = -{\omega_{2n}}^2 M_2 W_2(x)|_{x=L_2} \tag{2.20}$$

$$EI_2 \frac{d^2W_2(x)}{dx^2}|_{x=L_2} = I_{M2}{\omega_{2n}}^2 \frac{dW_2(x)}{dx}|_{x=L_2} \tag{2.21}$$

and the following transition conditions at $x = L_1$

$$W_1(x)|_{x=L_1} = W_2(x)|_{x=0} \tag{2.22}$$

$$\frac{dW_1(x)}{dx}|_{x=L_1} = \frac{dW_2(x)}{dx}|_{x=0} \tag{2.23}$$

$$EI_1 \frac{d^3W_1(x)}{dx^3}|_{x=L_1} - EI_2 \frac{d^3W_2(x)}{dx^3}|_{x=0} = -{\omega_{1n}}^2 M_1 W_1(x)|_{x=L_1} \tag{2.24}$$

$$EI_1 \frac{d^2W_1(x)}{dx^2}|_{x=L_1} - EI_2 \frac{d^2W_2(x)}{dx^2}|_{x=0} = I_{M1}{\omega_{1n}}^2 \frac{dW_1(x)}{dx}|_{x=L_1} \tag{2.25}$$

where I_{M1}, I_{M2} are the mass moment of inertia of the tip masses on the multi mode dynamic magnifier and the energy harvester, respectively.

By plugging Eq. (2.13) into the boundary conditions Eqs. (2.18)~(2.21) and the transition conditions Eqs. (2.22)~(2.25), we can obtain an eigenvalue problem regarding the coefficients $d = [C_1, C_2, C_3, C_4, D_1, D_2, D_3, D_4]^T$ and β

$$K(\beta_1, \beta_2)d = 0 \tag{2.26}$$

where $K(\beta_1, \beta_2)$ is a 8×8 matrix, and β_1 and β_2 satisfy Eq. (2.16).

$$K(\beta_1, \beta_2) = \begin{bmatrix} 1 & 0 & 1 & 0 & 0 & 0 & 0 & 0 \\ 0 & 1 & 0 & 1 & 0 & 0 & 0 & 0 \\ 0 & 0 & 0 & 0 & k_{35} & k_{36} & k_{37} & k_{38} \\ 0 & 0 & 0 & 0 & k_{45} & k_{46} & k_{47} & k_{48} \\ k_{51} & k_{52} & k_{53} & k_{54} & -1 & 0 & -1 & 0 \\ k_{61} & k_{62} & k_{63} & k_{64} & 0 & k_{66} & 0 & k_{68} \\ k_{71} & k_{72} & k_{73} & k_{74} & 0 & k_{76} & 0 & k_{78} \\ k_{81} & k_{82} & k_{83} & k_{84} & k_{85} & 0 & k_{87} & 0 \end{bmatrix} \tag{2.27}$$

where

$$k_{51} = \cos(\beta_1 L_1) \tag{2.*}$$

$$k_{61} = -\beta_1 \sin(\beta_1 L_1)$$

$$k_{71} = EI_1\beta_1^3 \sin(\beta_1 L_1) + \frac{M_1}{m_1} EI_1\beta_1^4 L_1 \cos(\beta_1 L_1)$$

$$k_{81} = -EI_1\beta_1^2 \cos(\beta_1 L_1) + \frac{I_{M1}}{m_1} EI_1\beta_1^5 L_1 \sin(\beta_1 L_1)$$

$$k_{52} = sin(\beta_1 L_1)$$

$$k_{62} = \beta_1 cos(\beta_1 L_1)$$

$$k_{72} = -EI_1\beta_1^3 cos(\beta_1 L_1) + \frac{M_1}{m_1} EI_1\beta_1^4 L_1 sin(\beta_1 L_1)$$

$$k_{82} = -EI_1\beta_1^2 \sin(\beta_1 L_1) - \frac{I_{M1}}{m_1} EI_1\beta_1^5 L_1 \cos(\beta_1 L_1)$$

$$k_{53} = \cosh(\beta_1 L_1)$$

$$k_{63} = \beta_1 \sinh(\beta_1 L_1)$$

$$k_{73} = EI_1\beta_1^3 \sinh(\beta_1 L_1) + \frac{M_1}{m_1} EI_1\beta_1^4 L_1 \cosh(\beta_1 L_1)$$

$$k_{83} = EI_1\beta_1^2 \cosh(\beta_1 L_1) - \frac{I_{M1}}{m_1} EI_1\beta_1^5 L_1 \sinh(\beta_1 L_1)$$

$$k_{54} = sinh(\beta_1 L_1)$$

$$k_{64} = \beta_1 cosh(\beta_1 L_1)$$

$$k_{74} = EI_1\beta_1^3 \cosh(\beta_1 L_1) + \frac{M_1}{m_1} EI_1\beta_1^4 L_1 \sinh(\beta_1 L_1)$$

$$k_{84} = EI_1\beta_1^2 sinh(\beta_1 L_1) - \frac{I_{M1}}{m_1} EI_1\beta_1^5 L_1 cosh(\beta_1 L_1)$$

$$k_{35} = EI_2\beta_2^3 \sin(\beta_2 L_2) + \frac{M_2}{m_2} EI_2\beta_2^4 L_2 \cos(\beta_2 L_2)$$

$$k_{45} = -EI_2\beta_2^2 \cos(\beta_2 L_2) + \frac{I_{M2}}{m_2} EI_2\beta_2^5 L_2 \sin(\beta_2 L_2)$$

$$k_{85} = EI_2\beta_2^2$$

$$k_{36} = -EI_2\beta_2^3 cos(\beta_2 L_2) + \frac{M_2}{m_2} EI_2\beta_2^4 L_2 sin(\beta_2 L_2)$$

$$k_{46} = -EI_2\beta_2^2 \sin(\beta_2 L_2) - \frac{I_{M2}}{m_2} EI_2\beta_2^5 L_2 \cos(\beta_2 L_2)$$

$$k_{66} = -\beta_2$$

$$k_{76} = EI_2\beta_2^3$$

$$k_{37} = EI_2\beta_2^3\sinh(\beta_2 L_2) + \frac{M_2}{m_2}EI_2\beta_2^4 L_2\cosh(\beta_2 L_2)$$

$$k_{47} = -EI_2\beta_2^2\cosh(\beta_2 L_2) - \frac{I_{M2}}{m_2}EI_2\beta_2^5 L_2\sinh(\beta_2 L_2)$$

$$k_{87} = -EI_2\beta_2^2$$

$$k_{38} = EI_2\beta_2^3 cosh(\beta_2 L_2) + \frac{M_2}{m_2}EI_2\beta_2^4 L_2 sinh(\beta_2 L_2)$$

$$k_{48} = EI_2\beta_2^2\sinh(\beta_2 L_2) - \frac{I_{M2}}{m_2}EI_2\beta_2^5 L_2\cosh(\beta_2 L_2)$$

$$k_{68} = -\beta_2$$

$$k_{78} = -EI_2\beta_2^3$$ (from 2.* to here is 2.28)

By solving the equation of the determinant of K equal to zero, i.e. $|K(\beta_1, \beta_2)| = 0$, the β_1 and β_2 values for all the modes in Eqs. (2.14) and (2.15) can be obtained. Correspondingly, the mode shapes for the coupled beam structure can be plotted after we obtain the eigenvector d, which will be shown in the next section.

2.4 Results of Illustrative Example

2.4.1 Results of Theoretical Analysis

The material properties of Aluminum beams used in the example are: Young's Modulus 69×10^9 N/m^2, density 2712 kg/m^3, Poisson's ratio 0.33. The mass and dimensions of the double beam system are selected based on the approximate guideline of double-beam design in Eqs. (2.10) and (2.11), as shown in Table 2.1.

The tip mass ratio was initially chosen to be $\frac{M_2}{M_1} = 5\%$, and the length of the energy harvesting beam was initially chosen to be 177.8 mm based on the preliminary design guideline. It was found in the simulation that additional adjustment of the length and the tip mass of the auxiliary beam was needed. Through trial and error, the length of the energy harvesting beam are finally selected to be 160.0 mm, and the tip mass increased to be 16.0 g, as shown in Table 2.1.

Based on Eq. (2.26), the natural frequencies and the corresponding mode shapes can be obtained. The first six modes are shown in Figure 2.3. The blue dash line represents the multi-mode dynamic magnifier/primary beam. The red solid line represents the energy harvester

beam/auxiliary beam. The results show that the vibration of the energy harvesting beam is much larger and that of the dynamic magnifier/primary beam is properly damped at all the six modes.

Table 2.1 The initial dimensions and the refined dimensions of the double-beam structure for the theoretical analysis

Beam	Width, b (mm)	Thickness, t (mm)	Length, L (mm)		Tip mass M_1 & M_2 (g)	
			Initial value	Refined value	Initial value	Refined value
Dynamic Magnifier	45.47	3.18	396.2	396.2	165	165
Energy Harvester	25.40	0.64	177.8	172.7	8.25	16.0

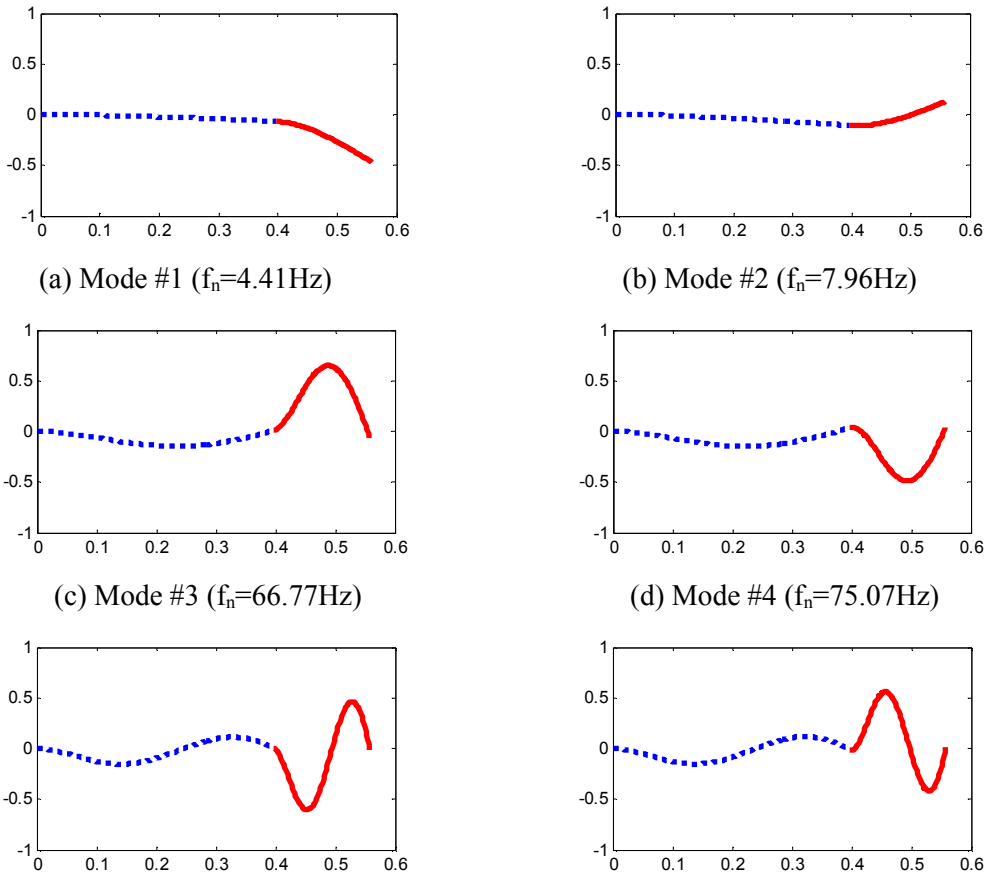

(a) Mode #1 (f_n=4.41Hz) (b) Mode #2 (f_n=7.96Hz)

(c) Mode #3 (f_n=66.77Hz) (d) Mode #4 (f_n=75.07Hz)

(e) Mode #5 (f_n=192.8Hz) (f) Mode #6 (f_n=202.9Hz)

Figure 2.3 The first six mode shapes of the double-beam structure obtained from the theoretical analysis

2.4.2 Finite Element Analysis

For the energy harvesting purpose, a piezoelectric film, with length less than the auxiliary beam, is adhered to the end part of the auxiliary beam to harvest the vibration energy, where the

strain is the largest. The material properties and the dimensions of the PZT film are shown in Table 2.2. The above closed form analytical solution for the coupled double beam is valid when the PZT film doesn't contribute much to the stiffness or mass of the harvester beam. For more general case, finite element method (FEM) analysis is performed in ANSYS. The FEM model with nodes and elements is shown in the Figure 2.4. A very fine mesh is used for generating accurate results for the higher order mode shapes and frequencies. The analysis is performed by considering the beam material as the linear isotropic material and the piezoelectric effect is only effective in 31 mode during the vibration. Using ANSYS the structure is tuned by varying the tip mass and the length of the energy harvesting beam and keeping the dimensions of the dynamic magnifier constant. Finally we achieved large vibration amplitude of the energy harvesting beam by damping the vibration of the dynamic magnifier/primary beam. Using the parameters of the double-beam system shown in Table 2.3, the results, i.e. the mode shapes for the first six natural frequencies, are obtained and shown in Figure 2.5, where it reveals that the energy harvesting beam has large vibration and the dynamic magnifier has very less when compared to it.

Table 2.2 The material properties and dimensions of the PZT film

Material properties	Young's modulus (E_p , N/m^2)	Piezoelectric constant (d_{31} , m/V)	Dielectric constant (ε_{33} , F/m)	Density (ρ, K/m^3)	Poisson's ratio	L × b × t (mm×mm×mm)
PZT	62×10^9	-320×10^{-12}	336×10^{-10}	7800	0.3	73.7 × 25.4×0.19

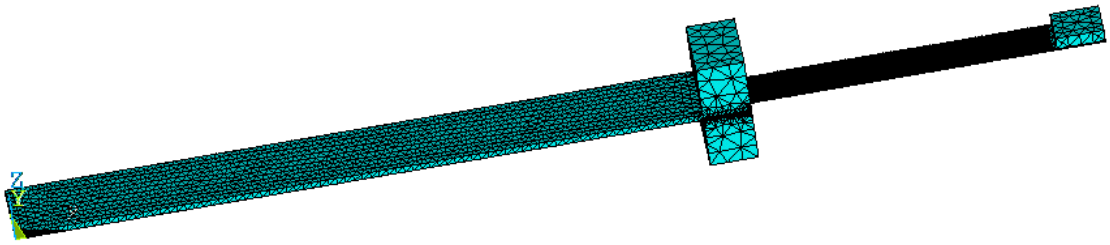

Figure 2.4 ANASYS finite element model of the Double beam harvester

Table 2.3 The initial dimensions and the refined dimensions of the double-beam structure for the FEM analysis

Beam	Width b (mm)	Thickness t (mm)	Length L (mm)	Tip mass M_1 & M_2 (g)
Dynamic Magnifier	45.47	3.18	401.3	165
Energy Harvester	25.40	0.64	185.4	11.15

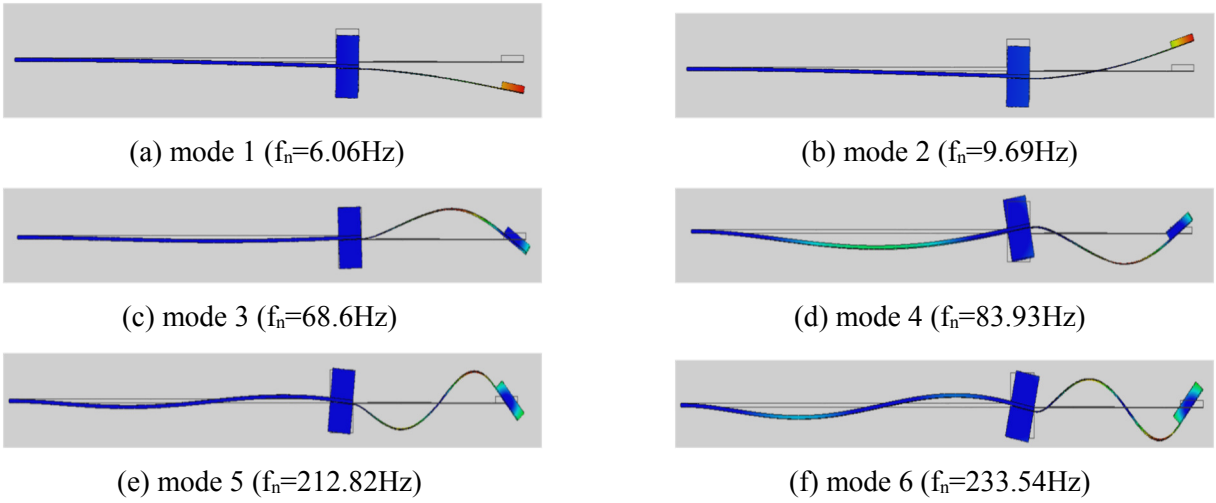

(a) mode 1 (f_n=6.06Hz)

(b) mode 2 (f_n=9.69Hz)

(c) mode 3 (f_n=68.6Hz)

(d) mode 4 (f_n=83.93Hz)

(e) mode 5 (f_n=212.82Hz)

(f) mode 6 (f_n=233.54Hz)

Figure 2.5 First six mode shapes from ANASYS simulation results

2.5 EXPERIMENTS

2.5.1 Experiment Setup

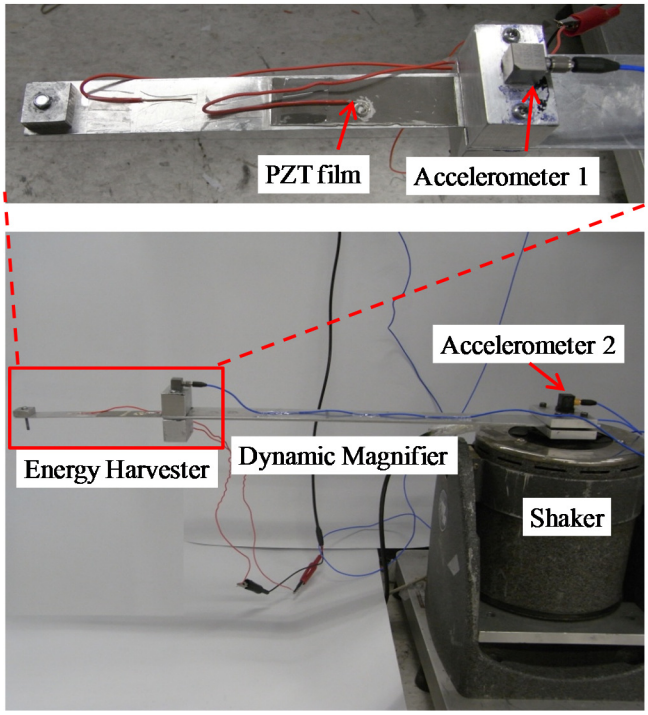

Figure 2.6 Experiment Setup

A prototype of the energy harvester with multi-mode dynamic magnifier is built with double aluminum (3300 alloy) beams. The prototype is built in such a way that the lengths L_2 and the tipmass M_2 of the energy harvester can be refined easily during the experiment. The experiment setup shown in Figure 2.6 is comprised of the double beam energy harvester, the

vibration shaker with power amplifier, accelerometer, four channel HP 35670A dynamic signal analyzer. The piezoelectric film is adhered to the energy harvesting beam at the end.

2.5.2 Experiment Results

Two sets of experiments are conducted. One is without PZT, and the other is with PZT. To validate the theoretical modeling in section 2.3, the experiments are conducted to measure the natural frequencies of the first six modes for the double-beam structure without PZT film. The vibration shaker excited the double beam energy harvester in swept sine mode in the frequency range of 3 Hz~300 Hz. One accelerometer is placed on the shaker to measure the input acceleration. Another accelerometer is placed at the tip of the primary beam to measure the response excited by the shaker input. The mass of the accelerometer is considered to be the part of the tip mass of the primary beam. The frequency response from the base acceleration to the tip acceleration of the primary beam was obtained and the first six natural frequencies are compared to the theoretical values and FEM results in Table 2.4. It can be seen that the relative errors of all the six natural frequencies are smaller than 6.6%. Table 4 also lists the natural frequency obtained by using FEM, where the relative errors of all the six natural frequencies are smaller than 8.2%.

The errors of the theoretical values and FEM values of the six natural frequencies when comparing with the experiment values in Table 2.4 and 2.5 are mainly due to the measurement errors of the dimensions used in the experiment, for example, the tip mass cannot be chosen to be exactly the same value as that used in the theoretical analysis, and the same case for the length of the beams.

Table 2.4 Comparison of the theoretical and measured natural frequencies of the double beam system without PZT

Mode	Experiment Results (Hz)	Theoretical Analysis		FEM Analysis	
		Theoretical value (Hz)	Relative error	FEM value (Hz)	Relative error
1	4.599	4.405	4.22%	4.71	2.41%
2	7.468	7.962	6.61%	7.71	3.24%
3	63.4	66.77	5.32%	66.90	5.52%
4	74.17	75.07	1.21%	80.24	8.18%
5	190.1	192.78	1.41%	200.97	5.72%
6	207.1	202.88	2.04%	212.98	2.84%

To validate the claims that this novel double-beam energy harvester 1) can improve the harvester efficiency and also widen the bandwidth for multimode, 2) can damp multimode of the

primary beam, experiments were carried out to measure the voltage generated from the harvester beam and the tip acceleration of the primary beam. Then, the frequency responses of the voltage and the acceleration were obtained by taking the shaker acceleration as the vibration input.

Table 2.5 Comparison of the FEM and measured natural frequencies of the double beam system when PZT is adhered

Mode	Theoretical value (Hz)	Experiment results (Hz)	Relative error
1	6.06	5.95	1.85%
2	9.69	9.38	3.30%
3	68.6	66.17	3.67%
4	83.93	78.52	6.89%
5	212.82	204.13	4.26%
6	233.54	222.37	5.02%

Figure 2.7 shows the frequency response measured at the tip of the primary beam with and without the energy harvesting beam. It can be seen that the vibration of the primary beam is effectively reduced around all the first three natural frequencies. This concludes that the design of continuous beam as multi-mode TMD can effectively damp the multiple modes of the primary structure.

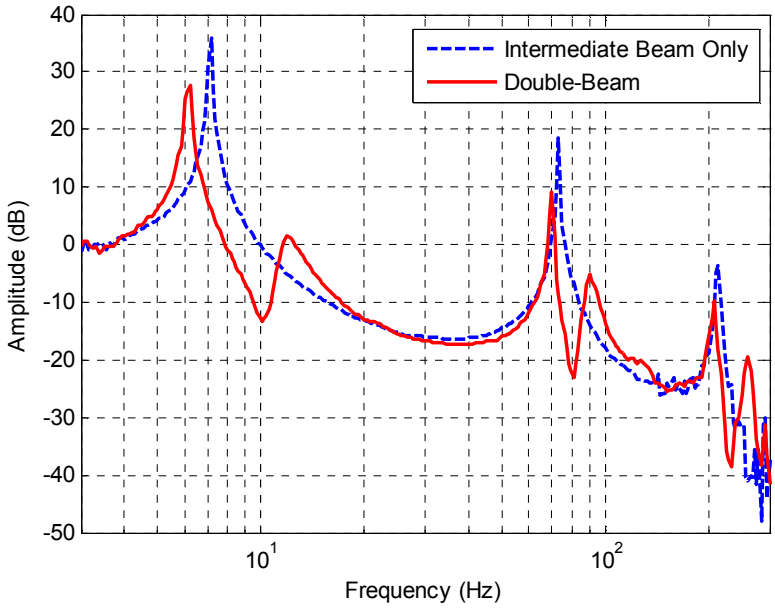

Figure 2.7 Frequency responses of $\frac{a_{primary\ beam}}{a_{base}}$

Figure 2.8 shows the measured frequency response of the open-circuit voltage generated from the PZT film with and without the dynamics magnifier (intermediate beam). Since the energy is proportional to the square of the voltage, by examining the integration of the voltage square of the curves in Fig 8, we conclude that the total energy harvested in the frequency range

of 3Hz to 300 Hz is 25.5 times more than that by the single-beam harvester. Also the energy harvesting bandwidth at every resonance frequency of the harvesting beam is substantially widened in the double-beam configuration. The ratio of the harvested energy using the proposed device over the single cantilever beam is shown in Fig. 9. It shows that near all the three resonances of the harvester beam, the energy harvested (square of voltage) is increased by a factor of 100 or more, even 1000 near the first mode.

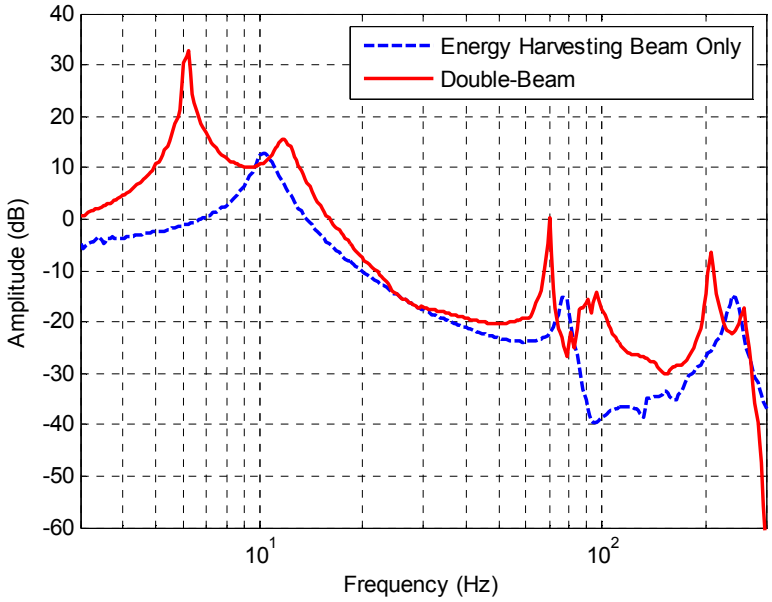

Figure 2.8 Frequency responses of $\frac{V}{a_{base}}$ in Volt/(m•s^{-2})

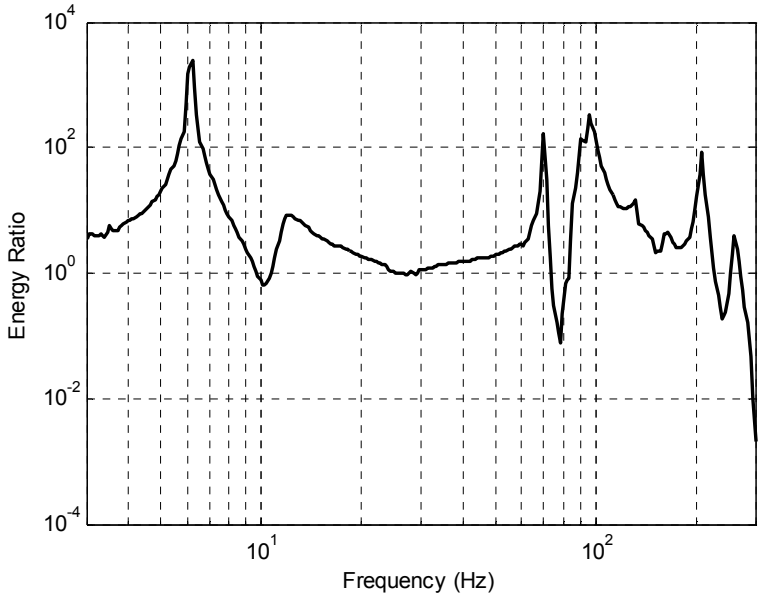

Figure 2.9 Ratio of harvested energy using double-beam structure over single cantilever beam

Although only the first three modes of single-beam were shown here, virtually all the modes can be tuned in theory as long as the dimensions and the tip mass are well designed.

2.6 CONCLUSIONS

A novel design of double-beam structure applicable for both efficient energy harvesting and multi-mode TMD vibration mitigation is proposed here. The preliminary design for finding the design parameters, like length, width, thickness of beam, and weight of the tip masses, is obtained by considering the two beams separately. Then, the theoretical analysis is conducted for the coupled beams by considering the interaction of one beam to the other. From the mode shapes of the first six resonant frequencies of the coupled structure drawn from the theoretical and FEM analyses, it shows that the voltage generated by the energy harvesting beam is dramatically magnified in larger bandwidth and the vibration of the primary beam is mitigated. The experiment result also shows the TMD effect for all the first three modes of the single beam. Virtually, all the modes can be tuned, as long as the dimensions of the two beams and the weight of the tip masses are well chosen. It is experimentally demonstrated that 25.5 times more energy can be harvested in frequency of 3Hz-300Hz from the energy harvesting beam by adding a multi-mode dynamic magnifier. The energy harvesting is increased even 100 times or more near these resonances. The ongoing work is designing the external circuit to further increase the harvester power and better damp the multiple modes of the double-beam structure.

Chapter 3 Piezoelectric Multilayer Stack Energy Harvester with Force Amplification

3.1 MOTIVATION

The current piezoelectric energy harvesting technologies can only harvest electrical power in the level of μW ~ mW, usually at a specific resonance frequency, with energy conversion efficiency less than 7.5% [134-137].

A significant problem that challenges us is how to harvest electrical power in the level of 10s mW to W in a broadband frequency range for devices requiring comparatively large power. 31-mode (stress is perpendicular to the dipole aligned direction) piezoelectric transducer has been developed [138]. Since the mechanical-to-electrical energy conversion efficiency of 33-mode (stress is in parallel with the dipole aligned direction) piezoelectric transducer is 3~5 times larger than that of 31-mode. In addition, a 33-mode piezoelectric transducer can produce twice more electrical charges than a same-size 31-mode piezoelectric transducer for the same level of stress/force. Feenstra, *et. al.* [139] proposed to use 33-mode piezoelectric transducer-based flextensional PEH. However, it has not been widely applied because the generated electrical power was only 1.9 mW, which is even not as high as the Cymbal piezoelectric energy harvester [134, 135]. Xu, *et. al* [140-142] invented several advanced PEHs utilizing 33-mode piezoelectric transducer. Theoretical results show that the proposed 33-mode flextensional PEHs can generate more electrical power than the Cymbals piezoelectric transducer.

Electromechanical properties of piezoelectric materials, such as piezoelectric coefficient, dielectric constant, and capacitance are strongly dependent on dynamic stress at quasi static frequencies [143-145]. At resonance frequency, in addition to the stress dependent properties, the mechanical impedance makes the problem even more complex. It makes the characterization of PEHs more difficult and the theoretical model more complex. Although the trial-and-error method to find the maximum value of the electrical power delivered to a resistive load is one of the most popular methods for piezoelectric energy harvesting study, the energy delivery ratio from a PZT stack to a matched resistive load and unmatched resistive loads have not been established so far.

A comprehensive study on 33-mode PZT multilayer stack-based flextensional energy harvester (PZT-Stack-FEH) has been carried out. The design has the ability of converting orders more mechanical energy to the piezoelectric transducer.

3.2 33-Mode PZT-Stack-FEH

3.2.1 Design Diagram

The diagram of PZT-Stack-FEH is shown in Figure 3.1. A 33-mode multilayer PZT ceramic stack is fixed inside a stainless steel flextensional frame, which has the function of converting the vertically applied force to a much larger horizontal force on the axial direction of the center PZT stack. Denote the vertically applied force as F_Z, the horizontal force applied on the axial direction of PZT stack is

$$F_X = \cot(\theta)\, F_Z = M F_Z \tag{3.1}$$

where θ is the angle of each beam among the four beams to the horizontal direction, as denoted in Figure 1a, M is the amplification factor, i.e., $M = \cot(\theta)$.

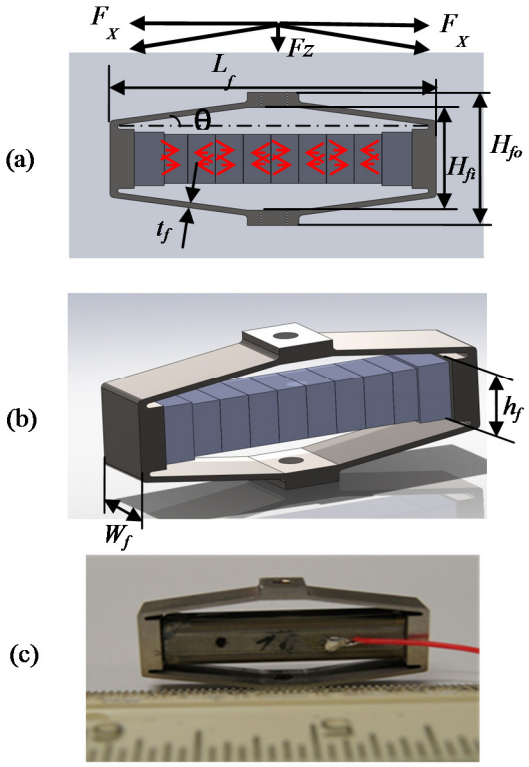

Figure 3.1 PZT-Stack-FEH (a) 2D diagram, (b) 3D diagram, (c) real picture

The PZT stack is composed of 300 layers of Navy Type II (CeramTec SP505) PZT plates with thickness of 0.1 mm, alternating with silver internal electrodes (301 layers) with thickness

of 0.1 μm. There is also a passive layer without electrodes at each end. The weight of the PZT stack is 12 grams and dimensions are 32.4 mm × 7 mm × 7 mm. The Young's Modulus of the PZT material is 106 GPa. The capacitance of the PZT stack is 2.5 μF. More details about the PZT stack can be found in reference [140]. The polarization direction of each layer of the stack is shown as the small arrows in Figure 1a. The length of the PZT stack was designed slightly longer than the length of the space inside the frame so that the stack is under a compressive stress when fixed into the frame to increase the reliability. When a vertical force is compressing the PZT-Stack-FEH, the center PZT stack will be stretched. When a vertical force is stretching the PZT-Stack-FEH, the center PZT stack will be compressed.

3.2.2 Optimal Design of Force Amplification Frame

Denote the effective spring constant of the PZT-Stack-FEH as k_H, the input mechanical energy into the PZT-Stack-FEH under the applied force in the vertical direction, F_Z, can be expressed as

$$U_{H,mech} = \frac{1}{2} k_H (\frac{F_Z}{k_H})^2 = \frac{F_Z^2}{2k_H} \tag{3.2}$$

Similarly, the transmitted mechanical energy into the center PZT stack can be expressed as

$$U_{S,mech} = \frac{1}{2} k_S (\frac{F_X}{k_S})^2 = \frac{F_X^2}{2k_S} \tag{3.3}$$

where F_X is the axial force applied on the stack, k_S is the elastic constant of the PZT stack, which can be expressed as [146]

$$k_S = \frac{E_S A_S}{L_S} \tag{3.4}$$

where E_S is Young's Modulus of PZT material, A_S is cross-section area of the stack, L_S is length of the stack.

According to Eq. (3.1), Eq. (3.3) can be written as

$$U_{S,mech} = \frac{M^2 F_Z^2}{2k_S} \tag{3.5}$$

The mechanical energy transmission ratio of the elastic frame is

$$\alpha = \frac{U_{S,mech}}{U_{H,mech}} = \frac{k_H M^2}{k_S} \tag{3.6}$$

Absolutely, the energy transmission ratio is smaller than 1, i.e., $\alpha < 1$. In order to get large mechanical-to-electrical efficiency, α should be designed as large as possible. That means when θ is chosen and the PZT stack is designed, we should have large spring constant of the

PZT-Stack-FEH, k_H. However, if the elastic frame is too stiff, the external force cannot be fully transmitted to the stack. Therefore, we design $\alpha \cong 0.5$. For a specific application, α should be determined based on the vibration level, the vibration source properties, and the requirement of the generated electrical energy. Finite element software is an effective way to determine α for industry design.

The dimensions of the frame are designed as shown in Table 3.1. The Young's Modulus of the steel material is 195 GPa. The weight of the frame is 6 grams. The frame was designed by Solidworks software and fabricated by a Wire-cut Electric Discharge Machining. The force amplification factor is $M = 5.5$.

Table 3.1 Parameters of the steel frame

Parameter	L_f	W_f	H_{fo}	H_{fi}	h_f	t_f
Value (mm)	38.0	8.0	17.5	9.7	7.0	0.70

3.3 THEORETICAL MODELING OF PZT-STACK-FEH

3.3.1 Electrical power generation

Assume the external force is

$$F_Z(t) = F_0 \sin(\omega t) \tag{3.7}$$

the generated voltage from the PZT stack can be expressed as [14]

$$V(t) = \frac{d_{eff}}{C_p} F_0 \sin(\omega t - \varphi) = V_0 \sin(\omega t - \varphi) \tag{3.8}$$

where C_p is piezoelectric capacitance, φ is phase difference between applied force and generated voltage, V_0 is the peak voltage, i.e.,

$$V_0 = \frac{d_{eff}}{C_p} F_0 \tag{3.9}$$

d_{eff} is the effective piezoelectric coefficient of the multilayer PZT stack, which can be expressed as

$$d_{eff} = Mcnd_{33} \tag{3.10}$$

where n is the number of piezoelectric layers, d_{33} is the piezoelectric coefficient in 33-direction, c is a constant, which is determined by the constraint effect from electrodes, the ratio of electrode area over the total area of the piezoelectric plate, the side electrodes, and the encapsulation layer of the multilayer stack. c is 95% for the co-fired PZT Stack used in this study.

The generated electrical energy can be expressed as

$$U_{elec}(t) = \frac{1}{2}C_p V^2(t) = \frac{d_{eff}^2 F_0^2}{2C_p} sin^2(\omega t - \varphi) = \frac{d_{eff}^2 F_0^2}{2C_p} \frac{1-\cos(2\omega t - 2\varphi)}{2} \quad (3.11)$$

By doing derivative, the generated power is

$$P_{elec}(t) = \frac{dU_{elec}(t)}{dt} = \frac{\omega d_{eff}^2 F_0^2}{2C_p} \sin(2\omega t - 2\varphi) \quad (3.12)$$

Combining with Eq. (3.9), Eq. (3.12) can be expressed as

$$P_{elec}(t) = \frac{\omega C_p V_0^2}{2} \sin(2\omega t - 2\varphi) \quad (3.13)$$

3.3.2 Mechanical-to-electrical efficiency

Considering the external force expressed as Eq. (3.7), the input mechanical energy to the PZT-Stack-FEH is

$$U_{mech}(t) = \frac{1}{2}k_H(\frac{F_Z(t)}{k_H})^2 = \frac{F_0^2}{2k_H} sin^2(\omega t) = \frac{F_0^2}{2k_H} \frac{1-\cos(2\omega t)}{2} \quad (3.14)$$

According to the definition of mechanical-to-electrical efficiency that average mechanical energy over average electrical energy, integrating Eq. (3.11) and Eq. (3.14), the mechanical-to-electrical efficiency of PZT-Stack-FEH is

$$\eta = \frac{\bar{U}_{elec}}{\bar{U}_{mech}} = \frac{d_{eff}^2 k_H}{C_p} \quad (3.15)$$

where $\bar{U}_{elec}$, $\bar{U}_{mech}$ are the average mechanical energy and the average electrical energy, respectively.

From Eq. (3.15) we can see that the mechanical-to-electrical efficiency is independent of the external excitation. It only relates to the parameters of the PZT-Stack-FEH structure.

3.3.3 Power delivery ratio to a resistive load

Many studies have been carried on the power delivery ratio [148-150], which is defined as the electrical power dissipated on the resistor over the total electrical power generated by the piezoelectric transducer. Their modeling predicted that the maximum power delivery ratio could attain 75% to a complex conjugate matching load. However, the practical situation cannot achieve the maximum, especially in the frequency ranges far from resonant frequency.

The equivalent circuit of PZT stack with a resistor is shown in Figure 3.2. PZT stack can be modeled as a dependent current source connected with a capacitor in parallel.

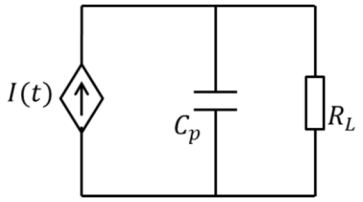

Figure 3.2 Equivalent circuit of PZT stack with a resistive load

The generated electrical charge is [147]

$$Q(t) = d_{eff}F_0\sin(\omega t - \varphi) \tag{3.16}$$

By doing derivative of charge, the current of dependent current source is

$$I(t) = \frac{dQ(t)}{dt} = \omega d_{eff}F_0\cos(\omega t - \varphi) \tag{3.17}$$

The voltage of PZT stack when connected to a resistive load is

$$V(t) = \frac{R_L}{\sqrt{1+(\omega C_p R_L)^2}}\omega d_{eff}F_0\cos(\omega t - \varphi + \theta) \tag{3.18}$$

where θ is the phase of impedance of C_p and R_L in parallel, i.e.,

$$\theta = -tan^{-1}(\omega C_p R_L) \tag{3.19}$$

The average power of total generated power from PZT stack is

$$\bar{P}_{total} = V_{RMS}I_{RMS} = \frac{R_L}{\sqrt{1+(\omega C_p R_L)^2}} \cdot (\frac{\omega d_{eff}F_0}{\sqrt{2}})^2 \tag{3.20}$$

where V_{RMS} is the root mean square value of $V(t)$ in Eq. (3.18), I_{RMS} is the root mean square value of $I(t)$ in Eq. (3.17).

The current passing through R_L is

$$I_{R_L} = \frac{1}{\sqrt{1+(\omega C_p R_L)^2}}\omega d_{eff}F_0\cos(\omega t - \varphi + \theta) \tag{3.21}$$

The electrical power dissipated on the resistive load is

$$P_{R_L} = \frac{R_L}{1+(\omega C_p R_L)^2}(\omega d_{eff}F_0)^2\, cos^2(\omega t - \varphi + \theta) = \frac{R_L}{1+(\omega C_p R_L)^2}(\omega d_{eff}F_0)^2\frac{\cos(2\omega t - 2\varphi + 2\theta)+1}{2} \tag{3.22}$$

The average power on the resistor is

$$\bar{P}_{R_L} = \frac{1}{2}\frac{R_L}{1+(\omega C_p R_L)^2}(\omega d_{eff}F_0)^2 \tag{3.23}$$

By combining Eq. (3.20) and Eq. (3.23), the power delivery ratio is

$$\sigma = \frac{\bar{P}_{R_L}}{\bar{P}_{total}} = \frac{\frac{1}{2}\frac{R_L}{1+(\omega C_p R_L)^2}(\omega d_{eff} F_0)^2}{\frac{R_L}{\sqrt{1+(\omega C_p R_L)^2}}\cdot(\frac{\omega d_{eff} F_0}{\sqrt{2}})^2} = \frac{1}{\sqrt{1+(\omega C_p R_L)^2}} \tag{3.24}$$

According to the impedance matching theory, the maximum power will be delivered to the resistive load when

$$R_L = \frac{1}{\omega C_p} \tag{3.25}$$

Substituting Eq. (3.25) into Eq. (3.24), the maximum power delivery ratio is

$$\sigma = \frac{1}{\sqrt{2}} = \frac{\sqrt{2}}{2} \tag{3.26}$$

From Eq. (3.26) we can see that the maximum power delivery ratio is about 70% when the resistive load matches the impedance of piezoelectric capacitor, which will be proved in the following experiment results.

3.4 EXPERIMENTS

3.4.1 Experiment Setup

The experiment setup for testing the performance of PZT-Stack-FEH is as shown in Figure 3.3. It includes a MB-100 shaker to generate mechanical vibration, a specially designed fixture frame to fix the top of the PZT-Stack-FEH and reduce the environmental unwanted vibrations, a PCB 208C02 force sensor to detect external force applied on PZT-Stack-FEH, two Polytech Laser vibrometers (OFV-056 and OFV-512 Fiber Interferometer, respectively) to detect the relative vibration displacement between top and bottom frames of PZT-Stack-FEH, and a HP 35670A dynamic signal analyzer to record data. For a more precise measurment, the following improvements have been applied: (1) in order to reduce the bending of the connection beam between the PZT-Stack-FEH and the top fixture frame, a stainless beam with the cross section of 2'' × 2'' was designed; (2) in order to reduce the deformation from the sensor adapters, 1.5'' hexagon stainless steel components and a 1'' diameter stainless steel thread were used; (3) in order to detect the real vibration of PZT-Stack-FEH, two Polytech laser vibrometers were employed to measure the top displacement and the bottom displacement of the PZT-Stack-FEH simultaneously.

A force sensor was fastened to the top of the PZT-Stack-FEH to measure the applied force from the shake vibration. The bottom of PZT-Stack-FEH was fixed to the shaker. The four channels of HP 35670A dynamic signal analyzer were set to record applied force, voltage, two

displacements, respectively. In addition, a group of power resistors were used for the electrical power delivery and impedance matching investigations. A EHC-601 (PIEZO SYSTEMS, INC, Woburn, MA) energy harvesting circuit with 6,600 μF capacitor was used to store electrical energy.

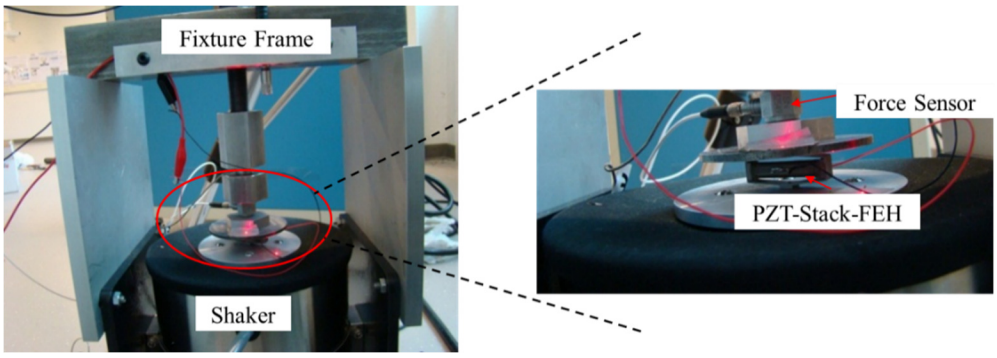

Figure 3.3 Experiment setup for PZT-Stack-FEH

The experiment setup for the study of vibration performance of the PZT-Stack-FEH with a proof mass is shown in Figure 3.4. The bottom of the PZT-Stack-FEH is fastened on the shaker (MB-100 Shaker), while the top end is connected with a proof mass. A PCB 356A17 accelerometer is used to measure the acceleration of the shaker vibration.

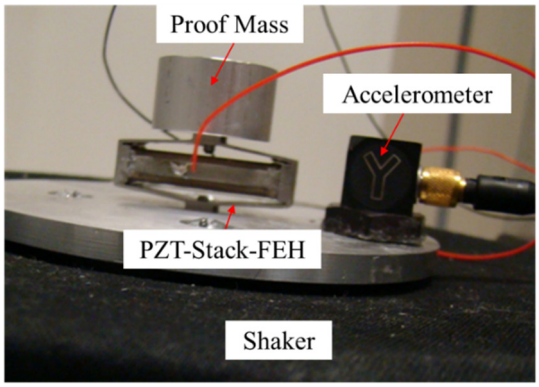

Figure 3.4 Experiment setup of PZT-Stack-FEH with a proof mass

3.4.2 Experiment Results

3.4.2.1 Power generation of PZT-Stack-FEH

Under the sinusoidal force excitation of $52N_{rms}$ in 250Hz, the generated voltage and energy from PZT-Stack-FEH are shown in Figure 3.5. From Figures 3.5(b) and 3.5(c), we can see that theoretical values of generated voltage based on Eq. (3.8) and theoretical values of generated energy based on Eq. (3.11) match well with the experiment results. The peak-to-peak value of generated voltage is 38.1V. The average energy is 300μJ. A 6,600μF supercapacitor is

used to store the electrical energy generated from PZT-Stack-FEH. The charging process is shown in Figure 3.6. It takes 1.6s to charge the supercapacitor from 0V to 7V. The total stored energy is 160mJ. Based on the relationship between electrical energy and charge, i.e.,

$$E = \frac{1}{2}VQ = \frac{1}{2}CV^2 \tag{3.27}$$

the stored electrical charge is 45.7mC.

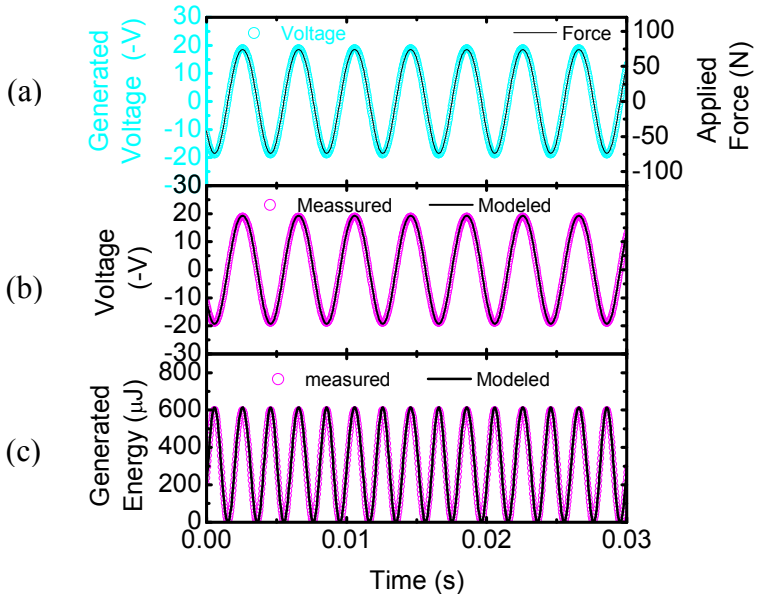

Figure 3.5 Generated voltage and energy from PZT-Stack-FEH under 52N_{rms} force in 250Hz, (a) Generated voltage v.s. Applied force, (b) Measured voltage v.s. Theoretical value, (c) Measured energy v.s. Theoretical value

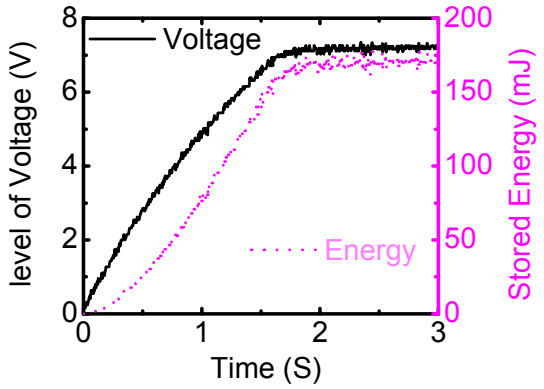

Figure 3.6 Accumulated voltage and energy stored in 6,600μF super-capacitor

The frequency responses of applied force, generated voltage, and effective piezoelectric coefficient under different force levels are shown in Figure 3.7. The generated voltage is 13.3V_{rms} under 50N_{rms}. We can see from Figure 3.7(a) that the generated voltage is proportional to the applied force. The effective piezoelectric coefficients under different force levels are

shown in Figure 3.7(c). The average effective piezoelectric coefficients at 10 Hz are 7.68 × 10^5 pC/N for 10 N_{rms}, 8.21 × 10^5 pC/N for 30 N_{rms}, and 8.73 × 10^5 pC/N for 50 N_{rms}, respectively. It means the effective piezoelectric coefficient increases along with the increasing of applied force, which is consistent with the conclusions in references [144,145,151].

Since the mechanical power is the product of applied force and vibration velocity of PZT-Stack-FEH, the measurement result of applied mechanical power is shown in Figure 3.7(a). Since the electrical power is the derivative of the electrical energy, i.e.,

$$P_{elec} = \frac{dU_{elec}(t)}{dt} = \frac{d}{dt}\left(\frac{1}{2}C_p V^2(t)\right) = C_p V(t)\dot{V}(t) \tag{3.28}$$

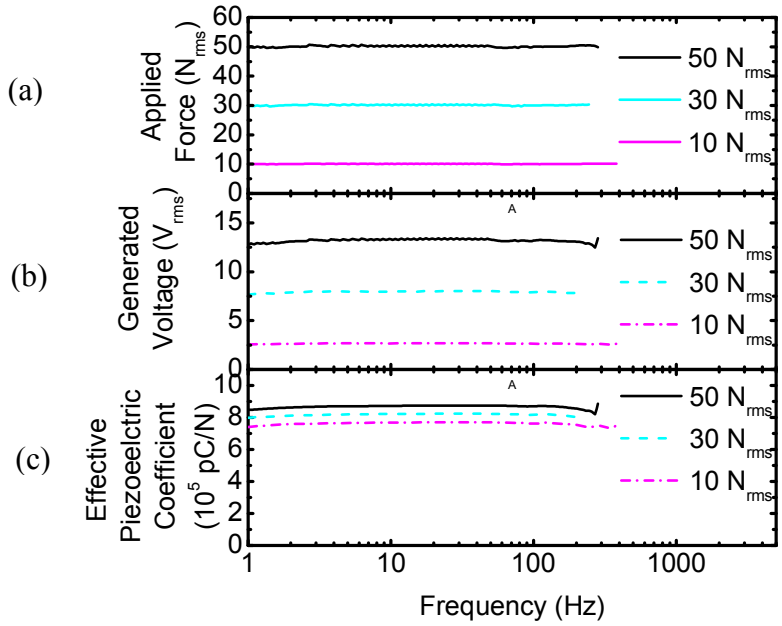

Figure 3.7 Frequency response of (a) Applied force, (b) Generated voltage, and (c) Effective piezoelectric coefficient

The generated electrical power is measured as shown in Figure 3.8(b). The mechanical-to-electrical energy conversion efficiency of PZT-Stack-FEH under different force levels is shown in Figure 3.8(c). Under force level of 50N_{rms}, the abnormal part of mechanical power in Figure 3.8(a) is due to the natural frequency of shaker at around 100Hz and the applied force is too large. From Figure 3.8(c) we find that the energy conversion efficiency is about 19% at different force levels in the frequency range of 1~100Hz. It is 2.5 times higher than the state-of-the-art piezoelectric harvesters.

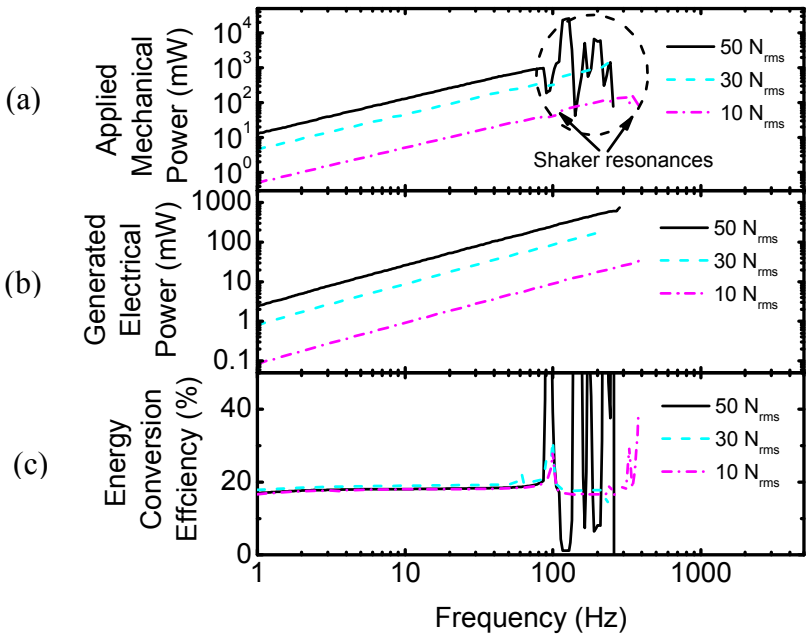

Figure 3.8 Frequency response of (a) mechanical power, (b) electrical power, and (c) energy conversion efficiency

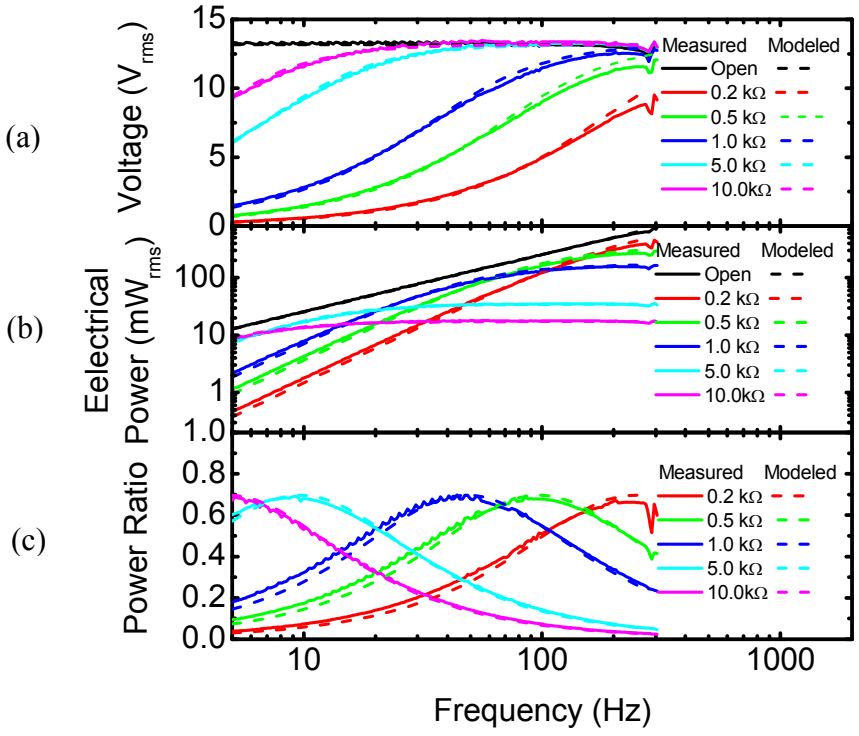

Figure 3.9 Frequency response of (a) generated voltage, (b) electrical power, and (c) power delivery ratio with different resistors

Under the force level of $50N_{rms}$, the generated voltage, the electrical power, and the power delivery ratio when connecting different resistors are shown in Figure 3.9. The theoretical

values are compared with the experiment results. Since the resistance of digital signal analyzer is about 2~3MΩ, we use 1MΩ to represent open-circuit. We can see from Figure 3.9 that the theoretical values match with the experiment results well. From Figure 3.9(c) we know that 70% of electrical energy from the PZT-Stack-FEH can be delivered to resistive load when the impedance of the electrical load matches with the impedance of the piezoelectric transducer, which is consistent with the theoretical analysis in section 3.3.3. Since the weight of the PZT-Stack-FEH is 18 grams and the volume is 4.0 cm^3, the power density of the PZT-Stack-FEH is 41.4W/kg or 186kW/m^3 at 303Hz under the force level of 50 N_{rms}.

3.4.2.2 Comparison between PZT-Stack-FEH and PZT stack

The comparison between the proposed PZT-Stack-FEH and the center PZT multilayer stack is shown in Figure 3.10. Under the same force level of 30N_{rms}, the generated voltage from PZT-Stack-FEH is 7.98V_{rms} in the frequency range of 1~100Hz, which is 4.84 times higher than 1.65V_{rms} generated from the PZT stack. The effective piezoelectric coefficient of PZT-Stack-FEH is 8.21×10^5 pC/N, which is 5.47 times larger than 1.50×10^5 pC/N of the PZT stack. From Figure 3.10(d~f) we can see that under the same force level of 30N_{rms}, the PZT-Stack-FEH can absorb 48.6 times more mechanical power and generate 26.5 times more electrical power than the PZT stack.

3.4.2.3 Vibration of PZT-Stack-FEH with a proof mass

The vibration performances of PZT-Stack-FEH with different proof masses under the excitation acceleration of 1g_{rms} are shown in Figure 3.11. We can see a peak for each proof mass in Figures 3.11(b)-(d), which corresponds to the natural frequency of the PZT-Stack-FEH structure with the proof mass. In Figure 3.11(a), it shows the shaker cannot provide 1g_{rms} acceleration at the natural frequency. Thus, Figure 3.11(d) of generated power over acceleration illustrates the normalized performance of the PZT-Stack-FEH structure. The peak power/acceleration for different proof masses are shown in Table 3.2. It can be seen from Figure 3.11 and Table 3.2 that the heavier proof mass, the more power can be generated at the same acceleration and the smaller the natural frequency will be.

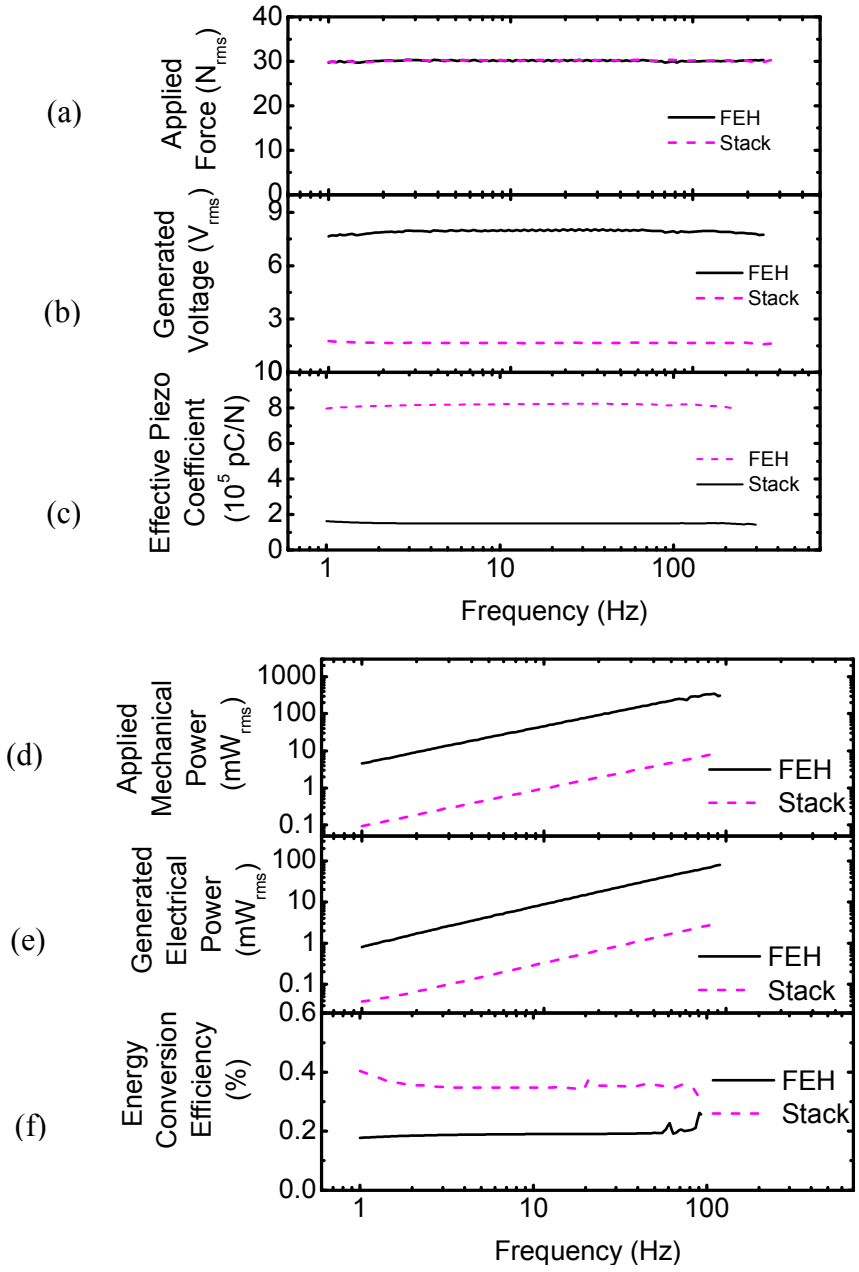

Figure 3.10 Comparison between PZT-Stack-FEH and PZT stack

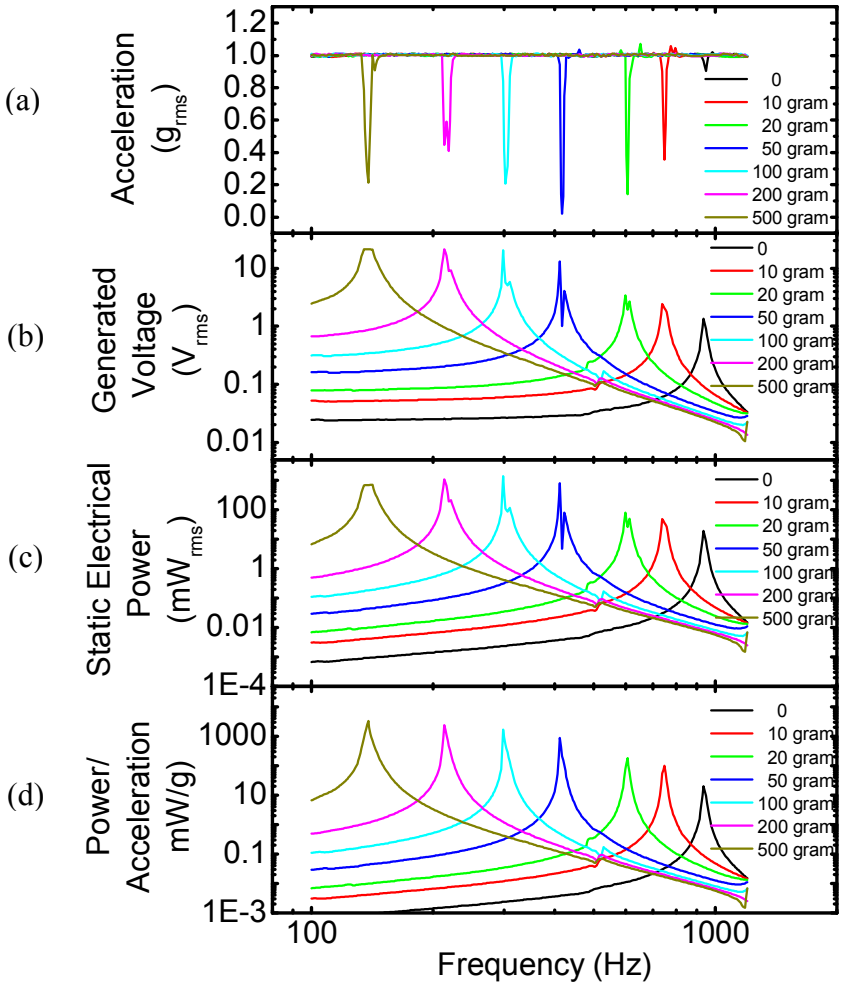

Figure 3.11 Frequency response of (a) excitation acceleration, (b) generate voltage, (c) electrical power, and (d) power/acceleration for PZT-Stack-FEH with different proof masses

Table 3.2 Peak of power/acceleration for different proof masses

Proof Mass (gram)	Peak Power/Acceleration (mW/g)	Natural Frequency (Hz)
0	20.0	936.0
10	100.0	748.4
20	179.9	605.9
50	860.9	412.2
100	1656.1	298.4
200	2398.7	213.4
500	3283.4	138.1

3.5 CONCLUSION

A high performance piezoelectric PZT multilayer stack based flextensional energy harvester (PZT-Stack-FEH) was proposed. An optimally designed elastic frame for force amplification is used to transmit more mechanical energy to the center PZT stack. It can absorb 48.6 times more mechanical energy to the PZT stack and generate 26.5 times more electrical

power than the PZT stack without force amplification frame. A 33-mode PZT stack was employed to increase the mechanical-to-electrical energy conversion efficiency, which is 19%. The maximum power delivery ratio of electrical power dissipated by resistive load over the total generated electrical power from PZT stack is about 70%, when the resistive load matches with the impedance of PZT stack. Experiment results match well with theoretical modeling results on generated electrical power, power delivery ratio to a resistive load, etc.. Since the weight of the PZT-Stack-FEH is 18 grams and the volume is 4.0 cm^3, the power density of the PZT-Stack-FEH is 41.4W/kg or 186kW/m^3 at 303Hz under the force level of 50 N_{rms}. Under the same force level of 30N_{rms}, the generated voltage from PZT-Stack-FEH is 4.84 times higher and the effective piezoelectric coefficient of PZT-Stack-FEH is 5.47 times larger than that of the PZT stack. The peak power/acceleration can attain 2398.7mW/g when the PZT-Stack-FEH is with a proof mass of 200 grams, and 3283.4 mW/g with a proof mass of 500 grams.

Chapter 4 Sensitivity-Enhanced Admittance-Based Structure Health Monitoring using A Higher-Order Resonant Circuit

4.1 MOTIVATION

Based on Peairs et al. [152]'s low cost measurement circuit, Wang and Tang [153] introduced an inductive circuitry to the electromechanical system by connecting a tunable inductor, a resistor and the piezoelectric element in series. The serial connection of the inductor and the piezoelectric capacitor creates an additional frequency resonant to the mechanical structure. It can greatly increase the admittance magnitude and the admittance sensitivity. The peak admittance magnitude with the inductive circuitry is increased by 28dB when comparing with the traditional one without the inductance, i.e., first-order circuit system. The admittance change is increased by 17, 25, and 33dB for the damage severity level of 0.2%, 1%, and 3%, respectively. They also introduced a negative capacitor to the electromechanical system [154], which can broaden the circuitry resonance to a much wider frequency range, so that the admittance magnitude is increased in a much wider frequency range.

Inspired by the Wang and Tang's method [153] using a second order circuit, and our series tuned mass dampers [155], we proposed a higher-order resonant circuit with clear physical insights for the piezoelectric-mechanical system to significantly improve the damage detection sensitivity. To do that, we first investigate the physical insights of Wang and Tang's method, with the understanding that the second order circuit is equivalent to adding a nontraditional tuned mass damper (TMD) to the mechanical system and the admittance measurement is to measure the velocity of the TMD mass under a given force on it. The admittance change is magnified at the resonant frequencies and thus the sensitivity of damage detection is increased. Since the series TMDs can further amplify the oscillation multiple times, we propose a methodology to design and optimize the higher order circuit in analogy with series TMD to achieve significant enhanced sensitivity.

4.2 THEORETICAL ANALYSIS

This section will briefly describe the modeling of the electromechanical system, look into the interesting physical insights with 2nd order circuit for damage detection, then present the higher order electrical circuit in analogy with the mechanical series TMDs.

4.2.1 Modeling of the electromechanical system without external circuit

The modeling of the base electromechanical system composed of a long beam and a piezoelectric transducer adhered on it at one vibration mode without external force can be expressed as

$$m_b\ddot{q} + c_b\dot{q} + k_b q = \theta V \tag{4.1}$$

$$\theta q + C_p V = Q \tag{4.2}$$

where q is the corresponding generalized mechanical displacement, V and Q are the voltage output and the electric charge between the two terminals of the piezoelectric transducer, respectively. C_p is the capacitance of the piezoelectric transducer. The modal mass m_b (kg), modal stiffness k_b (N/m), and electromechanical coupling coefficient θ (N/V) can be obtained using the energy method [156] as

$$m_b = \int_v \rho W^2 \, dv \tag{4.3}$$

$$k_b = E \int_v y^2 W''^2 \, dv \tag{4.4}$$

$$\theta = \int_{v_p} \frac{e}{t_p} y_p W'' \, dv_p \tag{4.5}$$

where W is the mode shape expression of the specific mode. W'' is the second derivative of W. v and v_p is the volume of the host beam and the piezoelectric transducer, respectively. ρ is the density of the host beam. E is the Young's modulus of the host beam material. y and y_p are the distance from the neutral axis in the host beam and in the piezoelectric transducer, respectively. e is the piezoelectric coupling coefficient (no dimension). t_p is the thickness of the piezoelectric transducer. We don't consider the expression for the modal damping c_b (N•s/m) above. The inherent damping of the metal based structure is generally 0.1%.

(a) (b)

Figure 4.1 Modeling of the structure with piezoelectric transducer in the modal space, (a) Base structure with piezoelectric transducer, and (b) Modeling in modal space

The modeling of the main structure with piezoelectric transducer in the modal space is as shown in Figure 4.1. It shows the interaction between the mechanical base structure and the

piezoelectric-based electrical circuit. The hypothesis is that the change of mechanical parameters may cause amplified change in electrical circuit, so that it is much easier to monitor the mechanical change by detecting the electrical change.

4.2.2 Physical insights of health monitoring with second-order circuit

Peairs *et al.* [152] brought up a method of measuring the voltage drop across a resistor which is connected serially with the piezoelectric transducer to obtain the impedance or admittance information. Based on Peairs *et al.*'s design, Wang and Tang [153] introduced a tunable inductor connected in series with the resistor as the external circuit of the piezoelectric transducer, as shown in Figure 4.2. In this subsection, instead of review Wang and Tang's work, we look into important physical insights that help us to present our higher order resonant circuit. There is an analogous relation between mechanical elements and electrical elements [157]. For example, mechanical force causes velocity, just as electrical voltage causes current. A damper dissipates mechanical energy, just as a resistor dissipates electrical energy. Springs and masses store mechanical energy, just as capacitors and inductors store electrical energy. The electrical-mechanical analogy is listed in Table 4.1.

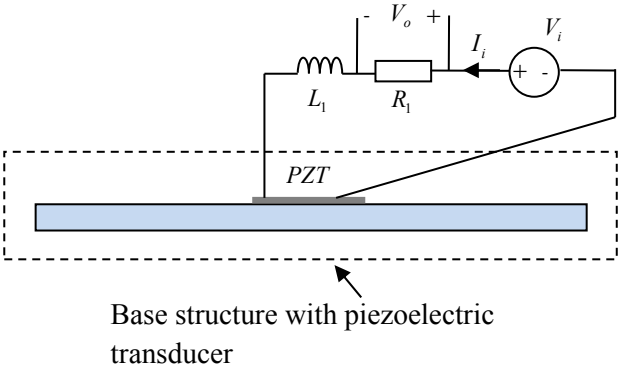

Figure 4.2 Second-order circuit system of admittance (I_i/V_i) based health monitoring [153]

Table 4.1 Electrical-mechanical analogy

Mechanical Elements	F (Force)	$\dot{x}$ (Velocity)	x (Displacement)	m (Mass)	k (Stiffness)	c (damping)
Electrical Elements	V (Voltage)	I (Current)	Q (Charge)	L (Inductor)	$\frac{1}{C}$ (reciprocal of Capacitance)	R (Resistor)

Using the analogous relation between mechanical elements and electrical elements, the modeling of the host structure with piezoelectric transducer in Eqs. (4.1) and (4.2) can be expressed as a pure electrical model shown in the dashed circle in Figure 4.3. The relationships

between the mechanical components and the electrical components are

$$L_b = \frac{m_b}{\theta^2}\,,\; L_1 = \frac{m_1}{\theta^2} \tag{4.6}$$

$$R_b = \frac{c_b}{\theta^2}\,,\; R_1 = \frac{c_1}{\theta^2} \tag{4.7}$$

$$C_b = \frac{\theta^2}{k_b} \qquad ,\; C_p = \frac{\theta^2}{k_1} \tag{4.8}$$

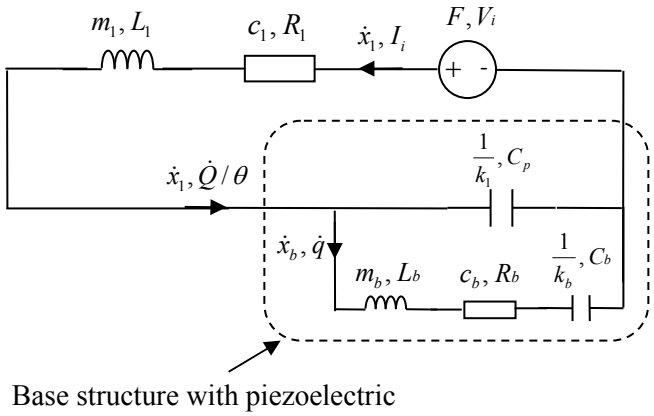

Figure 4.3 Equivalent circuit model of the piezoelectric structure in Figure 4.2, where the electrical admittance is I_i/V_i

The admittance of the system is $Y_1 = \frac{I_i}{V_i}$. For better comparison, the admittance is normalized with respect to the admittance of a stand-alone piezoelectric transducer, i.e., $\hat{Y}_1 = \frac{Y_1}{C_p s}$.

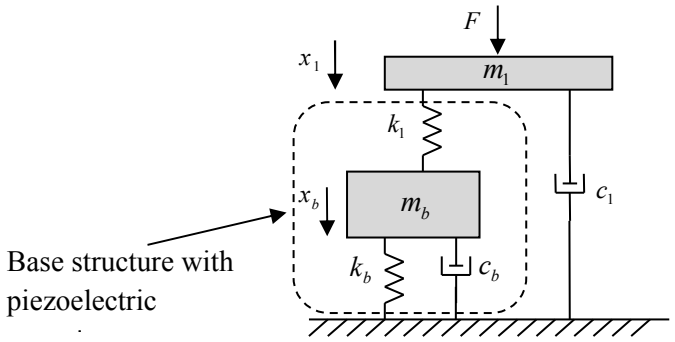

Figure 4.4 Equivalent pure mechanical model of Figure 4.2 as a nontraditional TMD, where the mechanical admittance we concern is the velocity $\dot{\boldsymbol{x}}_1$ for a given force F.

According to Table 4.1, the equivalent pure mechanical model of the circuit in Figure 4.3 is shown in Figure 4.4. The displacements of the two masses in Figure 4.4, i.e., x_b and x_1, correspond to the charges in Figure 4.3, or q and Q/θ in the modeling equations 4.1 and 4.2. Based on this analysis, we see the physical insights of the design in paper [153] is to add a non-traditional TMD to the base structure. We use "non-traditional" because the damper is not

directly connected to the base mass. The electrical admittance is equivalent to the velocity of the top mass m_1 under the unit external force excitation, i.e., $\frac{\dot{x}_1}{F}$. Under the same level of force excitation, the vibration of the top mass is much larger in the TMD system than vibration of the single-mass system with force *F*. Therefore, the overall admittance magnitude can be greatly increased. It also broadens the frequency range with large signal-to-noise ratio and high damage detection sensitivity.

It should be noted that Hagood and von Flotow [158] theoretically analytically interpreted and experimentally proved that piezoelectric shunt with a RL circuits will act as a TMD. However, the physical insight of shunt damping is significantly different from the admittance-based damage detection. In shunt damping, the concern is vibration of the base structure, and in damage detection we are taking advantage of amplified vibration at the absorber mass, or the amplified signal in the electrical circuit.

4.2.3 Sensitivity-enhanced health monitoring with higher-order resonant circuit

Since the second order circuit can enhance the sensitivity, one may expect that there is an opportunity to significantly increase the admittance magnitude and the admittance change by using higher order circuit when comparing with the second-order circuit system. However, how to design the higher-order circuit and how to determine the parameter are not trivial. Keeping in mind that the second order circuit has physical insights of adding a TMD to the beam system, we are inspired to design a type of series TMDs system and realize series TMDs in a higher-order admittance circuit, because series TMDs can further amplify the oscillation [155].

Since the resistor R_1 in the external circuit in Figure 4.2 is used to measure the current information, such a resister R_1 is not needed in the series TMDs design. Instead, another resister R_2 is added in the circuit at different position for current measurement. Correspondingly c_1 is ignored in the series TMDs system. A pure mechanical model with a non-traditional series two TMDs is shown in Figure 4.5. The mechanical admittance is the velocity of the top mass under unit force excitation, i.e., $\frac{\dot{x}_2}{F}$. Under the same level of force excitation, the vibration of the top mass m_2 in the series TMDs system in Figure 4.5 will be much larger than the vibration of the top mass m_1 in the single TMD system in Figure 4.4. Therefore, the admittance magnitude is expected to be significantly increased by using the series TMDs. According to the relationship of mechanical and electrical elements in Table 4.1, the pure mechanical system in Figure 4.5 can be

realized in electrical domain in Figure 4.6 using a higher order circuit and piezoelectric transducer on the host structure. The relationships between the mechanical and the electrical domains are

$$L_2 = \frac{m_2}{\theta^2} \tag{4.9}$$

$$R_2 = \frac{c_2}{\theta^2} \tag{4.10}$$

$$C_2 = \frac{\theta^2}{k_2} \tag{4.11}$$

The normalized admittance can be expressed as

$$\hat{Y}_2 = \frac{Y_2}{C_p s} = \frac{N_2(s)}{D_2(s)} \tag{4.12}$$

where

$$N_2(s) = C_2C_bL_1L_bs^4 + C_2C_bL_1R_bs^3 + \left[C_2C_b\frac{L_1+L_b}{C_p} + C_2L_1 + C_bL_b\right]s^2 + \left[C_2C_b\frac{R_b}{C_p} + C_bR_b\right]s + \frac{C_2+C_b}{C_p} + 1 \tag{4.13}$$

$$D_2(s) = C_2C_bC_pL_1L_2L_bs^6 + C_2C_bC_pL_1(L_2R_b + L_bR_2)s^5 + \left[C_2C_bL_2(L_1 + L_b) + C_2C_pL_1L_2 + C_bC_pL_b(L_1 + L_2) + C_2C_bC_pL_1R_2R_b\right]s^4 + \left[C_2C_b(L_1R_2 + L_2R_b + L_bR_2) + C_2C_pL_1R_2 + C_bC_p(L_1R_b + L_2R_b + L_bR_2)\right]s^3 + [C_2L_2 + C_bL_1 + C_bL_2 + C_pL_1 + C_pL_2 + C_bL_b + C_bR_2R_b(C_2 + C_p)]s^2 + \left(C_2R_2 + C_bR_2 + C_pR_2 + C_bR_b\right)s + 1 \tag{4.14}$$

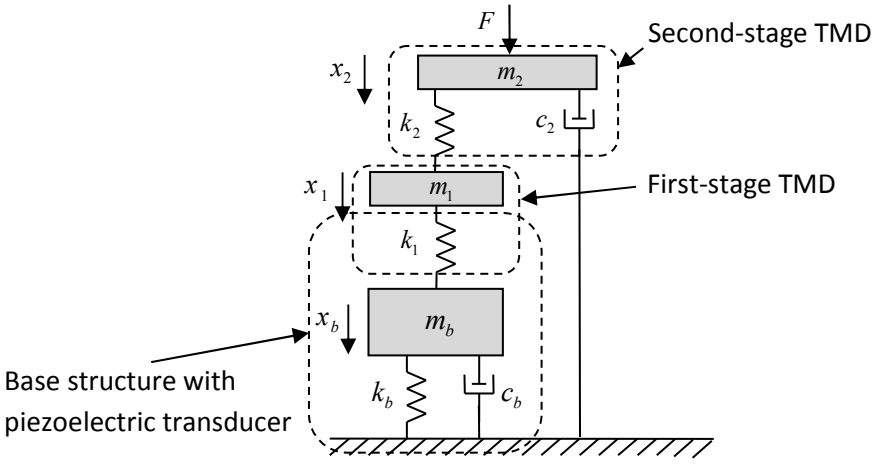

Figure 4.5 Pure mechanical model with a non-traditional double-mass series TMD system, where the mechanical admittance we concern is the velocity $\dot{\boldsymbol{x}}_2$ for a given force F.

The damage detection sensitivity can be reflected by the change rate of the admittance magnitude to the stiffness change. Based on Taylor series expansion, the admittance change of the second-order circuit system and that of the higher-order circuit system can be expressed respectively as

$$\Delta\hat{Y}_1 = \frac{\partial\hat{Y}_1}{\partial k_b}\cdot\Delta k = \delta\hat{Y}_1\cdot\Delta k \tag{4.15}$$

$$\Delta\hat{Y}_2 = \frac{\partial\hat{Y}_2}{\partial k_b}\cdot\Delta k = \delta\hat{Y}_2\cdot\Delta k \tag{4.16}$$

where Δk is the stiffness change of the host structure due to the damages. $\delta\hat{Y}_1$ and $\delta\hat{Y}_2$ represent the sensitivities of the damage detection methods with second-order circuit system and with higher-order circuit system, respectively. Similar expression for the mass change of the host structure can also be obtained.

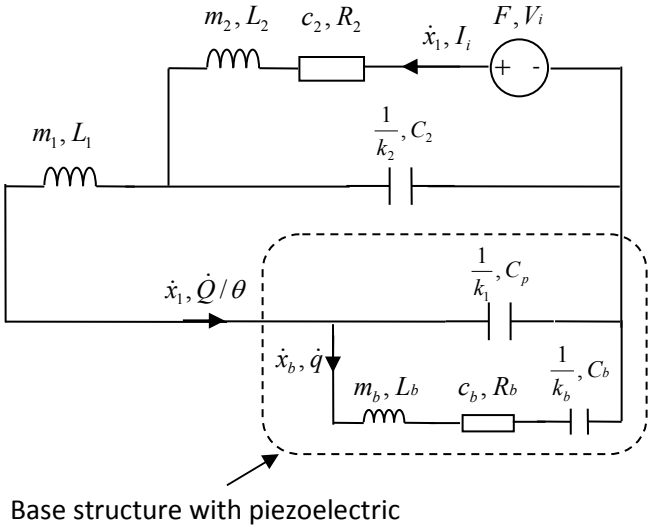

Figure 4.6 Equivalent pure electrical circuit of the mechanical system in Figure 4.5, where the electrical admittance is I_i/V_i

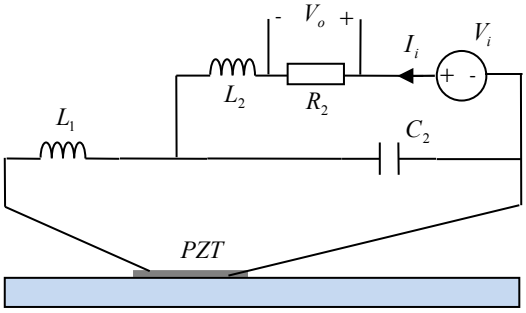

Figure 4.7 Proposed sensitivity-enhanced structure health monitoring using higher-order circuit

According to Figure 4.6, the higher-order external circuit for damage detection can be implemented as shown in Figure 4.7. It is critically important to determine the parameters in the proposed circuit to achieve the enhanced admittance and damage sensitivity. We will discuss in the next section.

4.3 PARAMETER DETERMINATION OF THE HIGHER ORDER CIRCUIT

4.3.1 Preliminary Parameter Selection

In this study, the same data of material properties and geometric parameters of beam and piezoelectric transducer in paper [153], as shown in Table 4.2, are used to illustrate the parameter selection and to verify the feasibility of the proposed method. The same methodology can also be used to other structures with different parameters. The 17th mode is also studied here. By substituting the parameters in Table 4.2 to Eqs. (4.3)~(4.5), the modal mass, stiffness, and the electromechanical coupling coefficient can be obtained, i.e., $m_b = 0.04051\ kg$, $k_b = 5.982 \times 10^7\ N/m$, $\theta = 0.01038\ N/V$. Since the structural damping ratio is generally $\xi = 0.001$, the modal damping is $c_b = 2\xi m_b \omega_n = 3.113\ N \cdot s/m$. According to Eq. (4.8), $k_1 = \theta^2/C_p = 0.01038^2/(8.875 \times 10^{-9}) = 1.214 \times 10^4\ N/m$.

Table 4.2 Material properties and geometric parameters of beam and piezoelectric transducer

	Young's modulus (N/m^2)	Density (kg/m^3)	Length (mm)	Width (mm)	Thickness (mm)	d_{31} (m/V)	ε_{33}^T (F/m)
Beam	73.1×10^9	2780	607.8	7.62	3.175	———	———
Piezoelectric Transducer	66×10^9	7800	17	7.62	0.191	-190×10^{-12}	1.6×10^{-8}

Since the mass ratios are very small, we expect the optimal damping of non-traditional series TMDs will be small. Then the vibration amplitude of x_2 will be much larger than the amplitude of x_1. In this sense, the effect of a small damper c_2 connected to the host base will have a similar effect as that connected to the middle mass m_1, which is the traditional series TMD. Therefore, we can use the parameters optimized for the traditional series TMD in [155] as the initial selections of the tuning parameters. Keep in mind that the optimal parameters Zuo [155] designed is to minimize the vibration (amplitude, velocity, or acceleration) of host structure m_b under the force excitation to the host structure, while the purpose in this paper is to improve the detection sensitivity, or the velocity of the top mass m_2 under force *F* excitation on m_2. Therefore, the parameters will be finally determined based on the tradeoff of sensitivity and practical constraints. It will be explained in detail in the following text.

If the mass ratio ($\mu = \frac{m_1+m_2}{m_b}$) is very small, the optimal tuning ratios for the first-stage TMD and the second-stage TMD in the series two TMDs system are both close to 1 [155]. That

is to say, the natural frequency of the host beam, the natural frequency of the first-stage TMD, the natural frequency of the second-stage TMD, should be equal to each other in the 17th mode, i.e.,

$$\sqrt{\frac{k_b}{m_b}} = \sqrt{\frac{k_1}{m_1}} = \sqrt{\frac{k_2}{m_2}} \tag{4.17}$$

From Eq. (4.17), m_1 can be obtained, i.e., $m_1 = \frac{m_b}{k_b} k_1 = \frac{0.04051}{5.982\times10^7} \times 1.214 \times 10^4 = 8.221 \times 10^{-6}\ kg$. Since m_2 is much smaller than m_1, the mass ratio is $\mu = \frac{m_1+m_2}{m_b} \approx \frac{m_1}{m_b} = 0.0203\%$. According to the method in paper [155], the optimal mass distribution of the two masses in the two TMDs is $\frac{m_2}{m_1+m_2} = 0.04\%$. Therefore, $m_2 = 3.289 \times 10^{-9} kg$. Based on Eq. (4.17), the stiffness in the second-stage TMD is $k_2 = \frac{k_b}{m_b} m_2 = \frac{5.982\times10^7}{0.04051} \times 3.289 \times 10^{-9} = 4.857\ N/m$.

From the method in paper [155], we can get the damping ratios optimized for host beam performance of the second-stage TMD $\xi_2 = 0.01215$. According to the relationship between the damping coefficient and the damping ratio, i.e., $c = 2\xi m\omega_n$, where ω_n is the natural frequency in rad/s^2, we can get the damping $c_2 = 3.071 \times 10^{-6}\ N \cdot s/m$. Thus, according to Eqs. (4.6), (4.9)~(4.11), the initially optimized values for all the electrical components in Figure 4.7 are determined, i.e., $L_1 = 76.30mH$, $L_2 = 30.53\mu H$, $R_2 = 0.0285\Omega$, $C_2 = 22.18\mu F$.

Since the parameter determination method in paper [155] is aimed at minimizing the vibration of the host beam with the constraint of the total mass ratio, the parameters obtained above for the second-stage TMD, i.e., R_2, L_2, C_2, can be viewed as initial values, which can be denoted as $R_2^* = 0.02850\Omega$, $L_2^* = 30.53\mu H$, $C_2^* = 22.18\mu F$. The final values to achieve higher damage detection sensitivity will be discussed in the following section.

4.3.2 Parameter Fine Tuning

As stated above, Zuo's method to determine the optimal parameters is minimizing the "performance output" of the host structure, while the admittance we measure is at the top mass. Therefore the parameters of the electrical components, i.e., R_2, L_2, C_2, still need to be fine tuned in order to achieve the best damage detection performance. We will discuss the effect of R_2 first, then discuss L_2 and C_2.

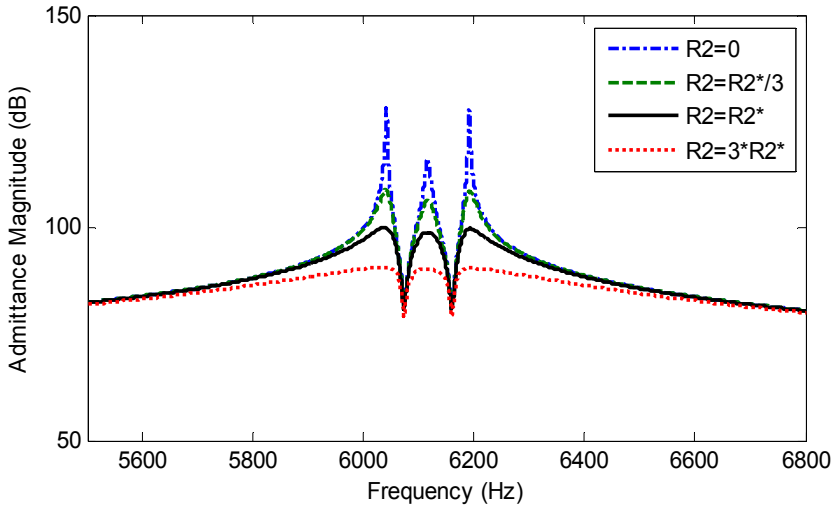

Figure 4.8 Normalized admittance magnitude of higher-order circuit with different $\boldsymbol{R_2}$ (when $\boldsymbol{L_2 = L_2^*}$)

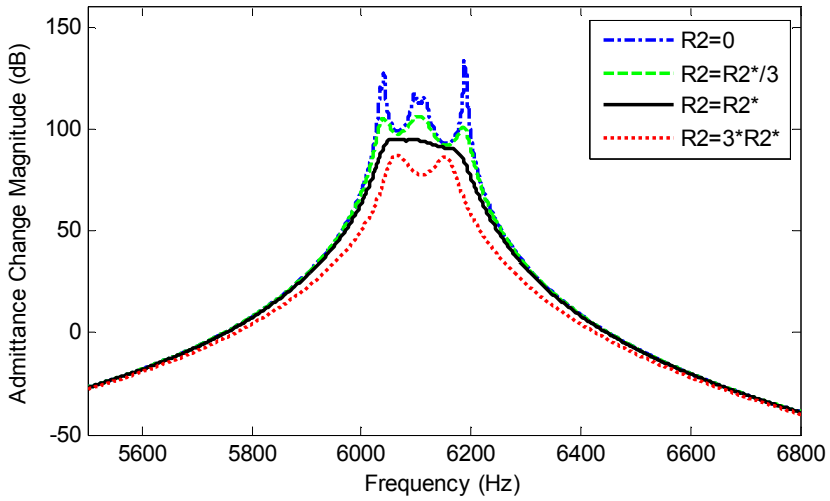

Figure 4.9 Normalized admittance change magnitude of higher-order circuit with different $\boldsymbol{R_2}$ (when $\boldsymbol{L_2 = L_2^*}$ with -1% stiffness change)

The smaller the damping coefficient in the second-stage TMD, i.e., c_2, the sharper the admittance magnitude will be, and the more sensitive to damages the method will be. The comparison of the admittance magnitudes and the comparison of the admittance changes with -1% stiffness change of the higher-order circuit with different resistances R_2 in the second stage are shown in Figure 4.8 and Figure 4.9, respectively. The effect of series two TMDs with three peaks can be seen in the traces for higher-order circuit in Figures 4.8 and 4.9. The comparison of admittance change magnitude with -1% stiffness change in Eqs. (4.15) and (4.16), is shown in Figure 4.9. The different resistances of R_2 correspond to different damping ratios in the second-stage TMD. By comparing the admittance magnitudes of the higher-order circuit with different

resistances, we can conclude that the smaller the resistor in the second-stage TMD, the better the system performs. Since resistor corresponds to damping in the mechanical system, it means we should set the damping coefficient in the second-stage TMD to be as small as possible. However, if the resistor is too small, not only it is hard to realize, but also create the difficulty, such as low signal noise ratio, to measure the electrical current through the voltage drop across it. Overall, the resistance in the second-stage TMD, i.e., R_2, should be small but practical for current measurement.

To study the effect of inductance L_2 or capacitance C_2, in Figures 4.10 and 4.11 we plot the admittance magnitudes and the admittance change magnitudes with -1% stiffness change of the higher-order circuit with a fixed R_2 value and different inductances L_2, i.e., $L_2 = L_2^*/3, L_2^*, 3L_2^*$. Note that C_2 will change correspondingly to keep frequency tuning to be the same as the structure resonance, i.e., $C_2 = 3C_2^*, C_2^*, C_2^*/3$. The different inductance of L_2 corresponds to different mass in the second-stage TMD. We can see from Figure 4.11 that when the second-stage TMD has the parameters of $R_2 = R_2^*$ and $L_2 = L_2^*$ the admittance change magnitude is flat in a large frequency range around the resonance. That is to say, when $L_2 = L_2^*$, the admittance change magnitude is robust to the excitation frequency. Therefore, the inductance in the second-stage TMD is chosen to be $30.53\mu H$, i.e., $L_2 = L_2^*$. Correspondingly, $C_2 = C_2^* = 22.18\mu F$.

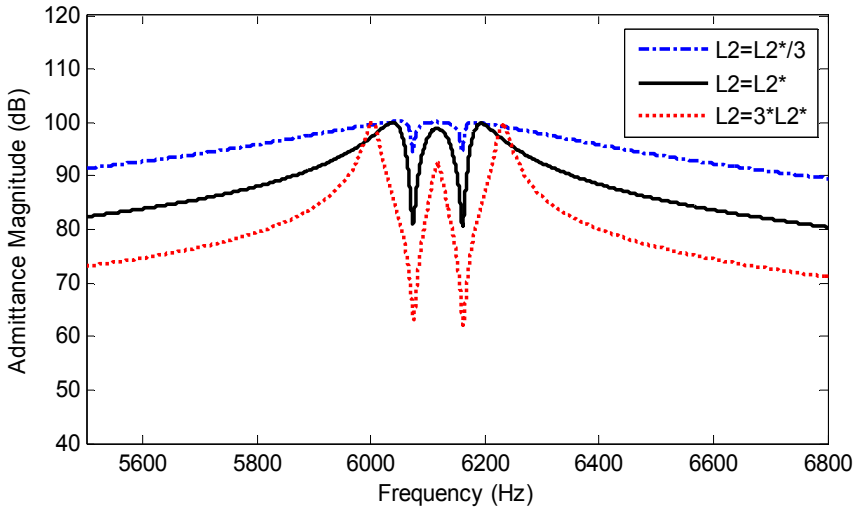

Figure 4.10 Normalized admittance magnitude of higher-order circuit with different $\boldsymbol{L_2}$

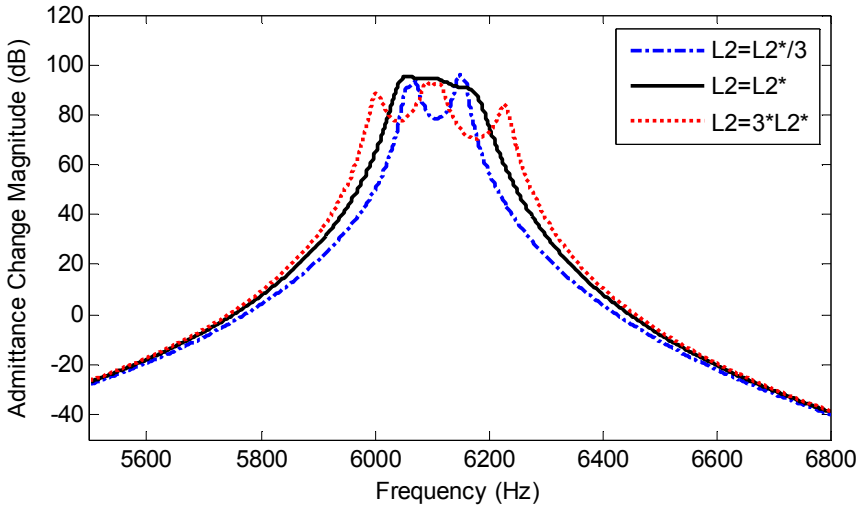

Figure 4.11 Normalized admittance change magnitude of higher-order circuit with different $\boldsymbol{L_2}$

4.4 CASE STUDY

Case Studies are conducted by taking the beam in Section 4.3.1 as an example and assuming small stiffness change due to the damage. The results of the proposed higher order circuit are compared with the second order circuit in reference [153] and the traditional admittance method in reference [152].

Given -1% stiffness change, the normalized admittance magnitudes of the undamaged structure and the damaged structure by using the proposed higher-order circuit with $R_1 = 0\Omega$ and $R_2 = R_2^*$ are shown in Figure 4.12, along with the results of the second-order circuit without electrical damping ($R_1 = 0\Omega$ in Figure 4.2) and the first-order circuit with only resistor in the external circuit. It can be seen that the peak of the admittance magnitude is increased by 74dB when using the proposed higher order circuit with $R_2 = 0\Omega$ and 46dB with $R_2 = R_2^*$, by comparing with the second order circuit in reference [153]. It means that under the same voltage excitation, the current measured in the higher-order circuit with $R_2 = R_2^*$ can be 200 times larger, or 5000 times larger with $R_2 = 0$, than that measured in the second-order circuit. Therefore the signal-to-noise ratio has been greatly improved.

In order to compare the damage detection sensitivities, the normalized magnitudes of admittance changes due to the stiffness change of -0.5% and -1% are shown in Figure 4.13, by using the three methods. The damage detection sensitivity can be increased by 33dB and 36dB by using the proposed method with $R_2 = R_2^*$ for the stiffness changes of -0.5% and -1%, respectively, when comparing with the second order circuit. It means that the damage detection

sensitivity when using the higher-order circuit is 45 times and 63 times higher than using the second-order circuit in the conditions that damage causes -0.5% and -1% stiffness changes, respectively. Figures 4.12 and 4.13 indicate that the admittance magnitude and the admittance change are both much larger in the electromechanical system with the proposed higher-order circuit than that with second-order circuit in paper [153], not to mention that with the first-order circuit in reference [152]. It is verified that the damage detection ability is significantly improved by using the proposed higher-order resonant circuit.

From Figure 4.12 we see that the admittance magnitude of the higher-order circuit system in the off-resonant frequency is also significantly higher than that with the second-order circuit system. The reason is that the external force excitation and velocity measurement in the mechanical system, which corresponds to the external voltage source and current measurement, are at two different locations for the two systems, i.e., the external force is applied on the second-stage TMD mass in the system with higher-order circuit, while the force is applied on the first-stage TMD mass in system with the second-order circuit. Similar physical insight can also be seen in the admittance change magnitude in Figure 4.13.

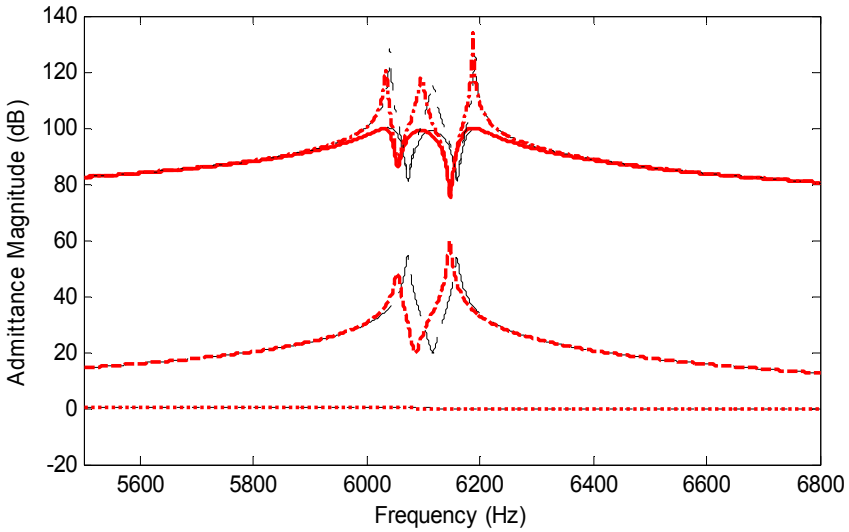

Figure 4.12 Normalized admittance magnitudes of the three methods: traditional first-order circuit for undamaged case (thinner dot) and damaged case (thicker dot) without damping of $\boldsymbol{R_1 = 0\Omega}$, second-order circuit for undamaged case (thinner dash) and damaged case (thicker dash) without damping of $\boldsymbol{R_1 = 0\Omega}$, proposed higher-order circuit for undamaged case (thinner dash-dot) and damaged case (thicker dash-dot) with $\boldsymbol{R_2 = 0\Omega}$, and proposed higher-order circuit for undamaged case (thinner solid) and damaged case (thicker solid) with $\boldsymbol{R_2 = R_2^*}$

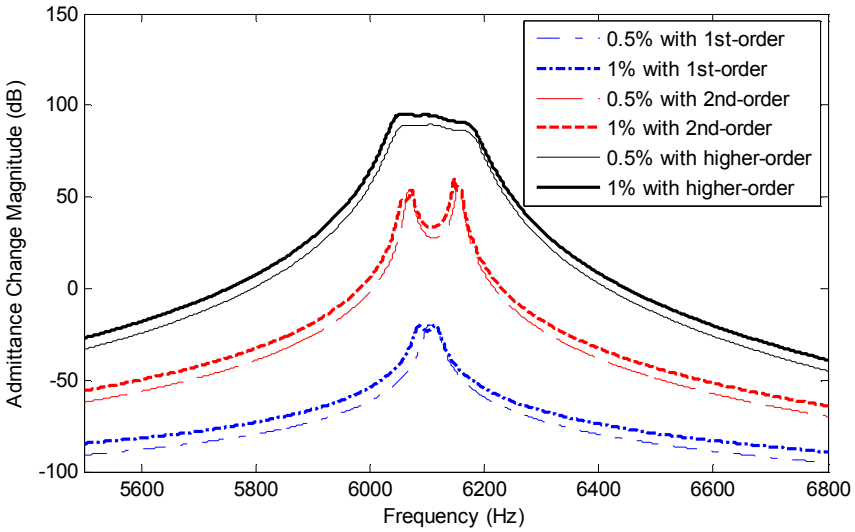

Figure 4.13 Normalized admittance change magnitudes of the three methods, i.e., higher order circuit with $\boldsymbol{R_2 = R_2^*}$, second order circuit, and traditional first order circuit

4.5 SENSITIVITY ANALYSIS

There are four electrical components in the proposed higher-order circuit, i.e., R_2, L_2, C_2 and L_1, as shown in Figure 4.7. Since inaccuracy exists in the nominal value of the electrical components, mainly due to parameter tolerance or temperature drift, sensitivity analysis to the electrical element parameters is necessary for the practical application of the structure health monitoring or damage detection method.

There are many kinds of resistors with different tolerances. For example, the common resistors have a tolerance ±5%. The metal film resistors can achieve the tolerance of ±0.5%, and are more stable under temperature and vibration extremes. The inaccuracies of inductors and capacitors are usually larger than that of resistors. The typical tolerance of inductance and capacitance values can be ±10% or more. However, precision inductors and capacitors are available with small tolerance. For example, the inductors with ferrite core can have ±1% tolerance, which is especially suitable for high frequency, even 20MHz, and can work in -40ºC~125 ºC. Polyphenylene sulfide (PPS) film capacitors are highly-precise, stable and reliable capacitors, which can attain ±1% tolerance. It can work up to 100kHz and in -55ºC~105 ºC.

Once an electrical component is selected for the circuit, the error of the real value compared with the nominal value due to the tolerance is fixed and will be the same in the measurements before and after damage. Therefore, the parameter tolerance itself will not really create artifacts. To illustrate this, we plot the admittance change due to 1% stiffness damage in

the system with 1% parameter tolerance, in comparison with the admittance change in the nominal system. It can be seen that the tolerance of R_2 has little influence, and difference due to the change of L_1 is relatively large.

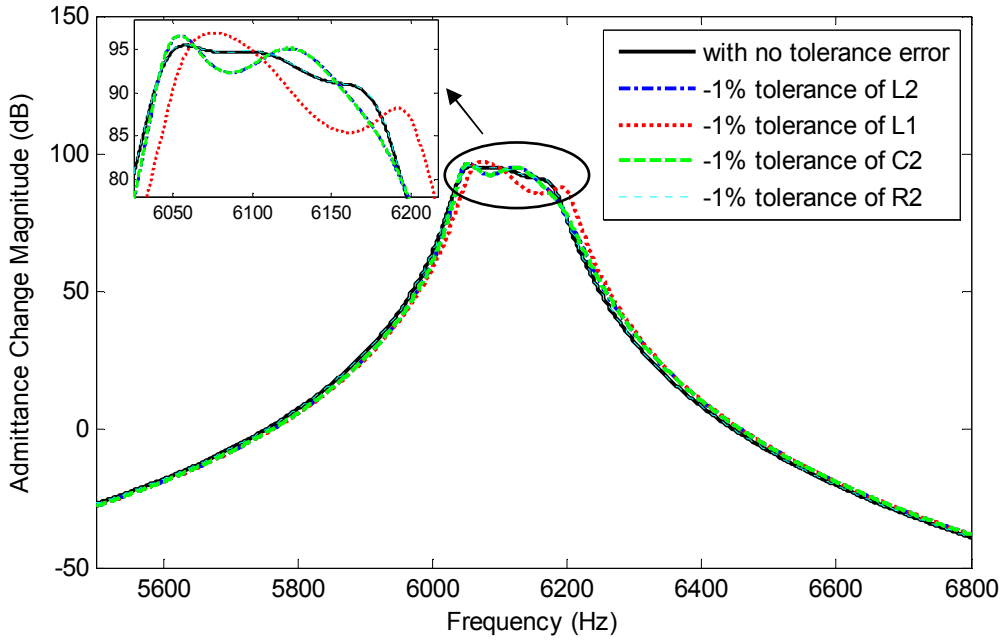

Figure 4.14 Normalized admittance change due to 1% stiffness damage in the nominal system and systems with parameter tolerances of electrical components

For practical application, the main concern is the parameter change of the electrical component during the measurement, such as due to the temperature drift. "Temperature coefficient" is used to represent the thermal stability of electrical component, with unit of "ppm/ ºC". 1 ppm/ ºC means the parameter value changes 0.0001% when the temperature changes 1 ºC. Temperature coefficient varies with different types of resistors. For example, thin film resistors have temperature coefficients of 5~25 ppm/ ºC, metal film resistors with 50~100 ppm/ ºC, and a type of ultra-precision foil resistors even have temperature coefficients of 0.14ppm/ ºC, in the temperature range of -55 ºC ~ +155 ºC. Different kinds of capacitors also have different temperature coefficient. The capacitance change of X5R capacitors is ±15% in the temperature range of -55 ºC ~ +85 ºC. However, NPO capacitors have temperature coefficient of 30ppm/ ºC with operation temperature of -55 ºC ~ +125 ºC [159]. The phenomenon of various temperature coefficient also exists in inductors. Some kinds have the temperature coefficient of 60ppm/ ºC, while others are with 30ppm/ ºC or even smaller in the operating temperature range of -55 ºC ~ +125 ºC [160]. Please note that the temperature coefficient is also a function of the temperature,

for most of the electrical elements, such as resistors, capacitors, and inductors, the temperature coefficient is much smaller in the temperature range around climate temperature (for example, -25 ^{o}C ~ +40 ^{o}C) than the extreme temperature. Therefore, we can find resistors, capacitors, inductors with small temperature drift in air temperature. For example, 30ppm/ ^{o}C literally represents less than 0.2% value drift with temperature change from -25 ^{o}C to +40 ^{o}C.

The sensitivity analysis of the normalized admittance change magnitude for R_2, L_2, C_2 and L_1, all with 0.2% change during the measurement, is shown in Figure 4. It compares the admittance change caused by the -1% stiffness change of the host structure due to damages. It can be seen from Figure 5 that the admittance change magnitude caused by the stiffness damages is much larger than that caused by the parameter change (such as temperature drift) of the electrical components in a broad range around the natural frequency. The peak admittance change magnitude caused by the -1% stiffness damage is 10dB (or 3 times) larger than that caused by the -0.2% parameter drift of the electrical components. The figure also indicates that the influence of R_2 value drift is small and thus R_2 doesn't need to be chosen with high temperature stability. We should choose the inductor L_1 with good thermal stability to ensure good damage detection and small artifact. Therefore, the proposed higher-order circuit will still performs well in large temperature range with careful selection of precision electrical components, especially the inductor L_1.

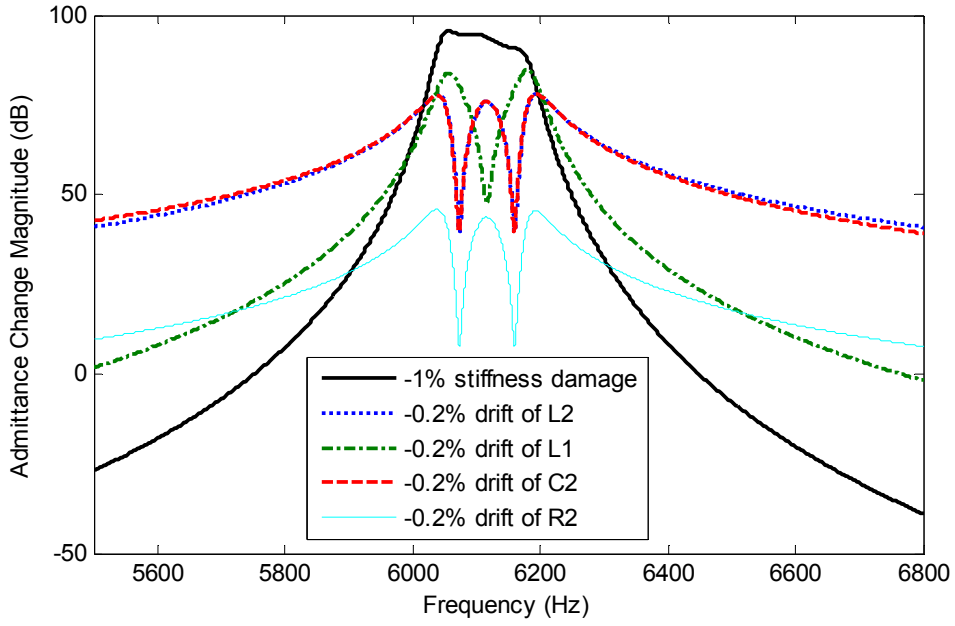

Figure 4.15 Comparison of normalized admittance change due to damage and due to temperature drift of the electrical components

4.6 EXPERIMENT

4.6.1 Experiment Setup

The whole experiment setup system is shown in Figure 4.16. The object is an Aluminum beam with free-free ends, which was hung by two flexible rubbers. The more flexible the rubbers are, the more environmental noise can be eliminated. The detailed structure of the beam with PZT is enlarged. A small piece of piezoelectric (PZT) film (PSI-5A4E) is adhered on the beam, with two soft wires connected to the PZT film and the Aluminum beam, respectively. The conductive wires should be as soft as possible, because hard wires will introduce unexpected external force to the beam.

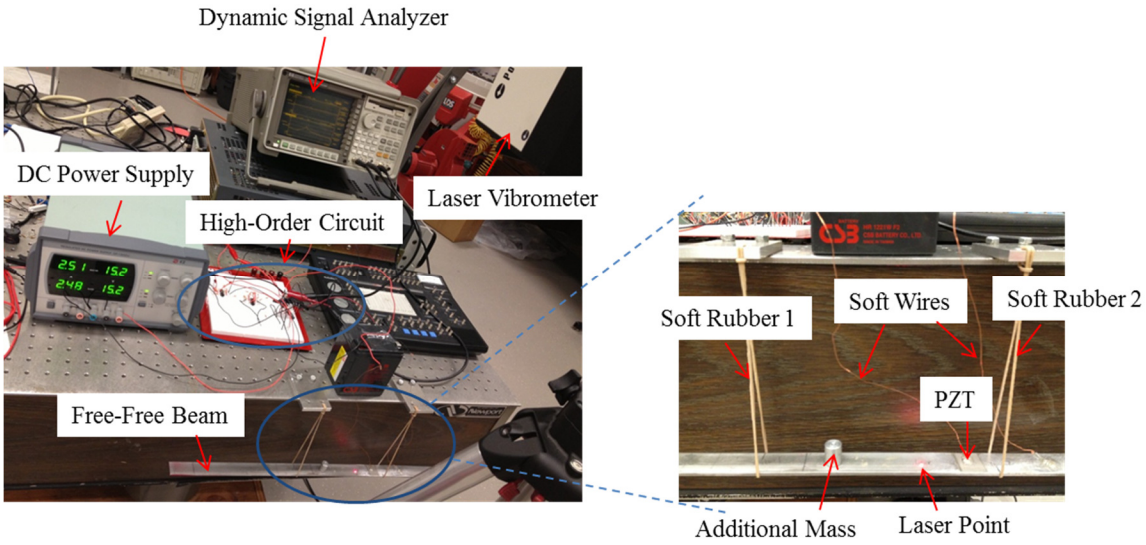

Figure 4.16 Experiment Setup

The material properties and geometric parameters of beam and piezoelectric transducer are listed in Table 4.3. The additional mass is used to mimic a kind of damage on the beam, which causes the stiffness change of the host structure. An HP 35670A dynamic signal analyzer is used to both generate excitation voltage and measure admittance of the system. The dynamic signal analyzer is a powerful instrument with the function of getting frequency domain information directly by using swept sine measurement mode. The high-order resonant circuit is built on a breadboard. Since the inductances in the circuit should be tuned to get resonances with the PZT capacitance and the other capacitor in the circuit, synthetic inductors should be built for adjustable inductances, which are composed of op-amps, capacitors, fixed resistors and adjustable resistors, etc. The details of synthetic inductor will be described in the next section. The DC power supply is used to provide DC voltage source for op-amps in the synthetic

inductors. A laser vibrometer (Polytec OFV-056) is used as a non-contact method to measure the vibration of the beam.

Table 4.3 Material properties and geometric parameters of beam and piezoelectric transducer

	Young's modulus (N/m^2)	Density (kg/m^3)	Length (mm)	Width (mm)	Thickness (mm)	d_{31} (m/V)	ε_{33}^{T} (F/m)
Beam	73.1×10^{9}	2780	609	25.4	3.175	———	———
Piezoelectric Transducer	66×10^{9}	7800	17	25.4	0.191	-190×10^{-12}	1.6×10^{-8}

Referring to the mode shape of the 17th vibration mode, the hung soft rubbers should be located at the places with zero vibration amplitude, while the PZT film, the additional mass, and the laser point should be located at the places with peak vibration amplitude. The detailed locations and the dimensions of the beam-PZT structure are shown in Figure 4.17.

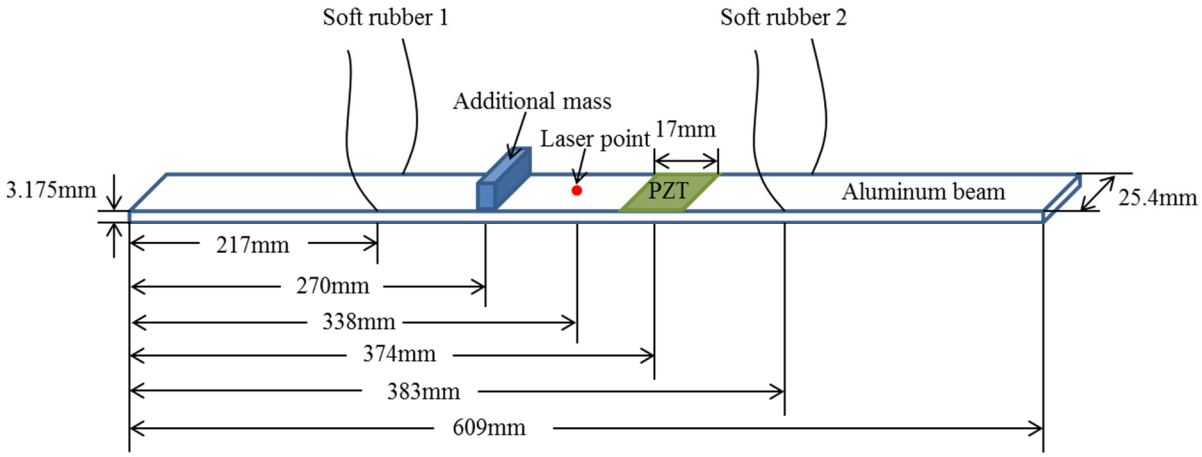

Figure 4.17 Beam measurement configuration

4.6.2 Synthetic Inductor

Since the regular inductors are all with fixed inductances, a method of generating adjustable inductance is highly required by the high-order resonant circuit with to-be-tuned inductors. Synthetic inductor is an effective solution to get the adjustable inductance performance. The configuration of synthetic inductor is shown in Figure 4.18. R is fixed resistor. R_T is adjustable resistor. C is fixed capacitor. The equivalent inductance of the synthetic inductor is

$$L = R_T RC \tag{4.18}$$

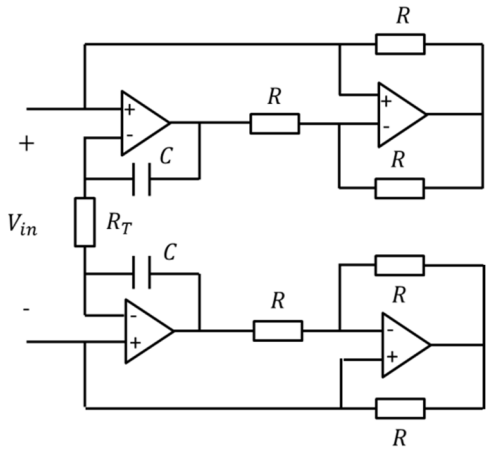

Figure 4.18 Configuration of synthetic inductor

From Eq. (4.18), we know that the realized inductance can be adjusted by changing the adjustable resistor. While doing experiments, we found several critical points we should pay attention, i.e., (1) the output of op-amp should be smaller than the maximum allowance limited by the DC voltage source; (2) there should be a discharging loop for the capacitor C, such as connecting a resistor in parallel. The resistor should be comparatively larger than the other fixed resistors R, but which should make the time constant of the discharging loop small enough so that the discharging process can be completed in a short time.

4.6.3 Experiment Results

According to the theoretical analysis method in section 4.2, the values of parameters in the high-order circuit are $L_1 = 22.86mH$, $R_2 = 0.00855\Omega$, $L_2 = 9.159\mu H$, $C_2 = 73.93\mu F$. The admittance of the beam-PZT structure with external circuit is obtained by measuring the current across a serially connected resistor over the input voltage excitation for R-shunt 1st-order circuit, RL-shunt 2nd-order circuit (as shown in Figure 4.2), and for high-order circuit (as shown in Figure 4.7). Assuming the complex admittance is $Adm(s)$, where $s = j\omega$, angular frequency $\omega = 2\pi f$, where f is the working frequency, the normalized admittance is defined as

$$NAdm(s) = \frac{Adm(s)}{C_p s} \tag{4.19}$$

Firstly, we built a synthetic inductor to realize L_1 and compared the normalized admittance magnitude of 2nd-order circuit with that of 1st-order circuit. The experiment results are shown in Figure 4.19. We can see that the normalized admittance magnitude measured from the beam-PZT with 2nd-order inductive circuit is much larger than that from the beam-PZT with

1st –order resistive circuit, and the admittance is very sensitive to the inductance, even 1 mH inductance change may cause more than 50 Hz frequency shift and amplitude change. The inductances of synthetic inductor, i.e., 27.5mH, 28.6mH, and 29.6mH, corresponds to the adjustable resistances of 1835Ω, 1906Ω, and 1972Ω, respectively. It indicates that the admittance-based damage detection method has high requirement for the accuracies of electrical components, and small inductance change, which cannot be realized by regular inductors, can be accomplished by synthetic inductor. The corresponding beam vibrations with different inductances in 2nd-order circuit are shown in Figure 4.20. It can be seen that the best tuned inductance for 2nd-order circuit is 28.6mH with two equal-height vibration peaks.

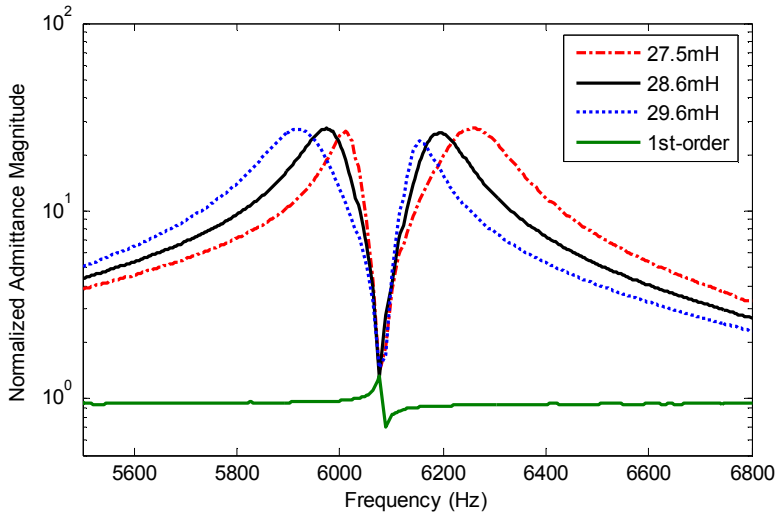

Figure 4.19 Comparison of normalized admittance magnitude of 2nd-order circuit and 1st-order circuit

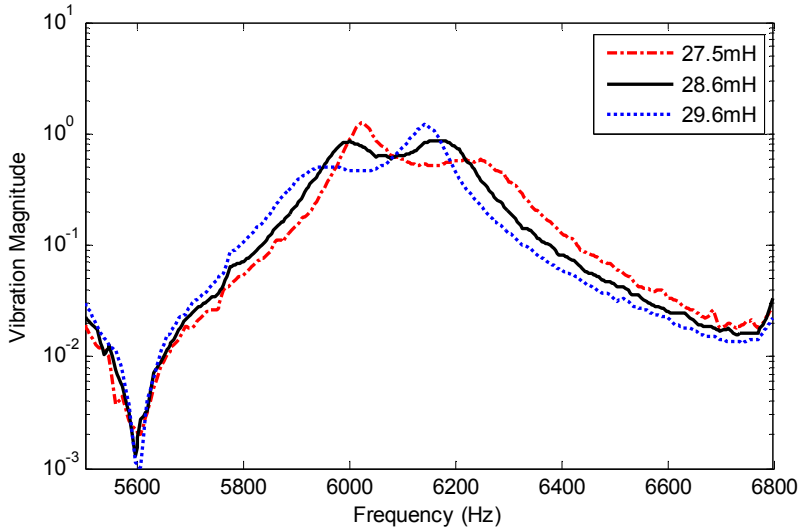

Figure 4.20 Corresponding beam vibration to different inductances

Secondly, we used an additional mass to mimic the kinds of damages which may cause the stiffness change of the host structure. The location of the additional mass is shown in Figure 4.16 and Figure 4.17. The beam vibrations before damage and after damage are shown in Figure 4.21, from which we can see the natural frequency has been changed from 6077Hz to 5974 Hz, i.e., -1.69% stiffness change. Lastly, we built the proposed high-order circuit system. Since the optimal value $R_2 = 0.00855\Omega$ is too small to be realized, we used a 0.02Ω resistor as R_2. Due to the evitable resistance in inductor, the total resistance of $L_2 - C_2$ resonant circuit is about 0.25Ω. For the $R_2 - L_2 - C_2$ resonant circuit, the damping ratio is

$$\zeta = \frac{R_2}{2}\sqrt{\frac{C_2}{L_2}} \tag{4.20}$$

Substituting the optimal values of L_2, C_2 and real resistance of 0.25Ω into Eq. (4.20), the damping ratio is 0.704. That is the reason why the three peaks in high-order circuit system is not obvious, as shown in Figure 4.22. The comparison of the normalized admittance magnitude of high-order resonant circuit system with 1st-order circuit system and 2nd-order circuit system is shown in Figure 4.22. We can see that the normalized admittance magnitude of the proposed structure health monitoring method with high-order resonant circuit is much higher than the 1st-order circuit and the 2nd-order circuit in Figure 4.2, which indicates that the signal-to-noise ratio is significantly increased and the damage sensitivity is also greatly improved. The results are consistent with the simulation results.

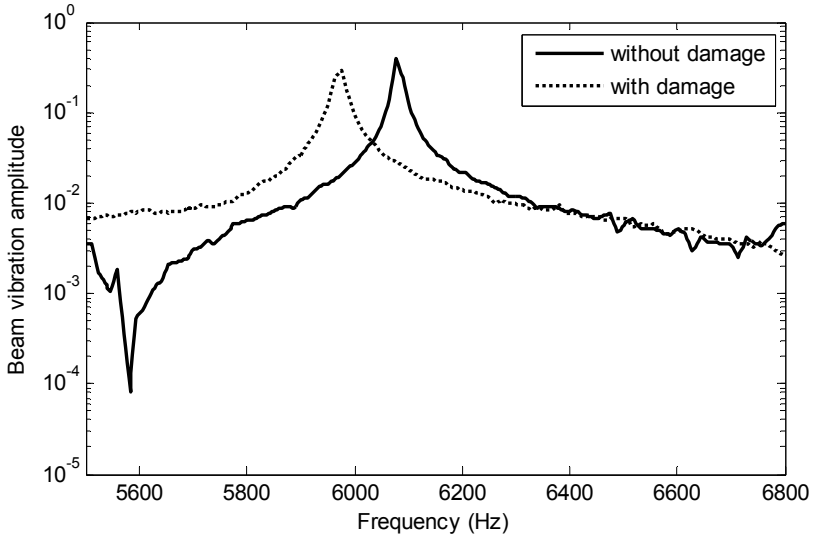

Figure 4.21 Beam vibration in the 17th mode

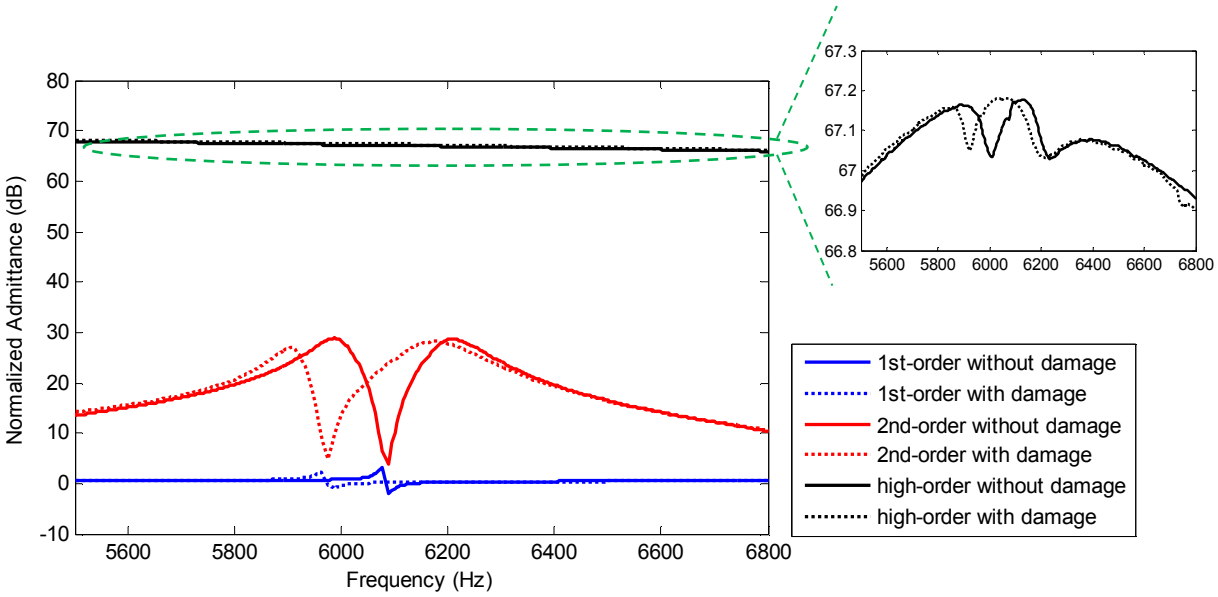

Figure 4.22 Normalized admittance magnitude of three types of circuit

4.7 CONCLUSIONS

Based on the electrical-mechanical analogy, a novel structure health monitoring technology with higher-order resonant circuit is proposed in this paper. A second-order circuit system with an inductive circuitry in the external circuit is also compared. We created an equivalent mechanical model of the damage detection with the second-order circuit and indicated that the physical insight is to add a TMD to the host mechanical system. Inspired by this insight, we proposed to design a higher-order resonant circuit to realize greatly high sensitivity in a way similar as a series two TMDs system. The simulation results verify that the damage detection sensitivity is significantly improved by using the higher-order resonant circuit than the second-order circuit and the traditional admittance method. The parameter selection of inductor, capacitor, and resistor of the circuit in the second stage TMD is also analyzed. The signal-to-noise ratio is increased by 74 to 46dB by using the designed higher-order resonant circuit and the damage detection sensitivity is increased by 33dB and 36dB for the stiffness change of 0.5% and 1%, respectively, when comparing with the second-order circuit system. The sensitivity of the performance to the parameter drifts of electrical components is also studied. It is concluded that the system can still maintain the high signal-to-noise ratio and the high damage detection sensitivity. Experiment verified the theoretical analysis and simulation results.

Chapter 5 A Self-Powered Piezoelectric Vibration Control System with Switch Pre-Charged Inductor (SPCI) Method

5.1 MOTIVATION

Guyomar, *et al.* [161, 162] proposed the synchronized switch damping (SSD) to efficiently suppress the structural vibration. Li et al. [163] extended an improved SSD technique based on an energy transfer scheme to damp the vibration of the target structure. However, regarding control method, the buck-boost converter or SSD method is essentially a passive or semi-active control, the control performance of which is not as good as active control. The synchronized switch method [164, 165] has a limitation that it only works for sinusoidal vibration, since the voltage converting process only occurs when the displacement of the structure attains the maximum or minimum. However, random vibration exists even more widely than sinusoidal vibration in reality. A universal vibration control method for all the kinds of vibrations, including random vibration, sinusoidal vibration, etc., is highly required. Moreover, the implementation of self-powered control is also a challenge.

This chapter focuses on development of an integrated system with simultaneous functions of random vibration control and energy harvesting. Inspired by the phenomenon in the L-C resonant circuit that the capacitor voltage can be inverted in a very short time, a so-called "Switch Pre-Charge Inductor" (SPCI) method is proposed to implement the desired control force through quickly controlling the capacitor voltage in a large range via pre-charging the inductor and controlling the switch between L and C. When the capacitor voltage attains its desired value, the remaining inductor current, which is converted from the structure vibration energy, will be transmitted to the energy storage unit. Another key advantage of this method is that it facilitates decent voltage tracking by employing discontinuous conduction, of which the switching frequencies is much lower than conventional PWM-based techniques.

5.2 MODELING OF FLEXIBLE-BEAM WITH PZT

A uniform cantilever beam with a tip mass, m, is shown in Figure 5.1. Since the stress in the fixed end of the cantilever beam is larger than the rest part in the dominant modes with low frequencies, we have a PZT film only covering a short segment of the beam at the fixed end, as shown in Figure 5.1. The structure is under the base excitation with dynamic acceleration of $a_{base}(t)$.

Figure 5.1 Flexible-beam structure with PZT film

The differential equation of motion of a uniform cantilever beam with no external force or base acceleration [166] is

$$EI\frac{\partial^4 w(r,t)}{\partial r^4}+\rho A\frac{\partial^2 w(r,t)}{\partial t^2}=0 \tag{5.1}$$

where $w(r,t)$ is the relative displacement of a point at position r on the beam in the beam coordinate, E is the Young's modulus, I is the area moment of inertia, ρ is the density, and A is the cross-section area.

Based on the modal superposition method, the deformation of the beam can be expressed as

$$w(r,t)=\sum_{n=1}^{\infty} W_n(r)q_n(t) \tag{5.2}$$

where $q_n(t)$ is the generalized coordinate in the n^{th} mode, $W_n(r)$ is the n^{th} normal mode,

$$W_n(r)=C_{1n}\cos(\beta_n r)+C_{2n}\sin(\beta_n r)+C_{3n}\cosh(\beta_n r)+C_{4n}\sinh(\beta_n r) \tag{5.3}$$

where $C_{1n}\ to\ C_{4n}$ are constants depending on the boundary conditions.

The corresponding natural frequencies of all the modes of the structure in Figure 1 is

$$\omega_n=\beta_n{}^2\sqrt{\frac{EI}{\rho A}}\quad,\quad n=1,2,3,\cdots \tag{5.4}$$

where β_n is obtained based on the boundary conditions for the structure.

Using the energy equilibrium method [167],

$$\int_{t_1}^{t_2}(\delta T+\delta U-f\delta w)\,dt=0 \tag{5.5}$$

where T is the kinetic energy, U is the potential energy, f is the d'Alembert force or inertia force per unit length dr at point r on the beam, i.e.,

$$f=\rho_b A_b a_{base}+\rho_p A_p a_{base}+m a_{base}\delta(r-L_b) \tag{5.6}$$

where ρ_b, A_b are the density and the cross-section area of beam, respectively; ρ_p, A_p are the density and the cross-section area of PZT film, respectively; $\delta(\cdot)$ is the Dirac delta function. Note that f is in the opposite direction as a_{base}, according to the definition of the inertia force.

Without considering mechanical damping in the system, the mechanical properties of the flexible-beam energy harvester for multi-mode can be expressed as

$$\begin{gathered}\sum_{j=1}^{n} M_{1j}\ddot{q}_j + \sum_{j=1}^{n} K_{1j}q_j - \theta_1 V_p + \int_r \ fW_1(r)\,dr = 0 \\ \vdots \\ \sum_{j=1}^{n} M_{ij}\ddot{q}_j + \sum_{j=1}^{n} K_{ij}q_j - \theta_i V_p + \int_r \ fW_i(r)\,dr = 0 \\ \vdots \\ \sum_{j=1}^{n} M_{nj}\ddot{q}_j + \sum_{j=1}^{n} K_{nj}q_j - \theta_n V_p + \int_r \ fW_n(r)\,dr = 0\end{gathered} \tag{5.7}$$

where

$$M_{ij} = M_b^{(ij)} + M_p^{(ij)} + mW_i(L_b)W_j(L_b) \tag{5.8}$$

$$K_{ij} = K_b^{(ij)} + K_p^{(ij)} \tag{5.9}$$

L_b is the length of beam-PZT, $M_b^{(ij)}$and $M_p^{(ij)}$ are the modal mass of beam and PZT film associated with mode shapes W_i and W_j, respectively, i.e.,

$$M_b^{(ij)} = \int_{v_b} \rho_b W_i W_j \, dv \tag{5.10}$$

$$M_p^{(ij)} = \int_{v_p} \rho_p W_i W_j \, dv \tag{5.11}$$

v_b and v_p are the volume of beam and PZT film, respectively; ρ_b and ρ_p are the density of beam and PZT film, respectively; $K_b^{(ij)}$and $K_p^{(ij)}$ are the modal stiffness of beam and PZT film associated with mode shapes W_i and W_j, respectively, i.e.,

$$K_b^{(ij)} = E_b \int_{v_b} y_b^2 W_i'' W_j'' \, dv \tag{5.12}$$

$$K_p^{(ij)} = E_p \int_{v_p} y_p^2 W_i'' W_j'' \, dv \tag{5.13}$$

E_b and E_p are the Young's modulus of beam and PZT film, respectively; y_b and y_p are the distance of the point on the beam and on the PZT film from the neutral axis of beam-PZT, respectively; θ_i is the electromechanical coupling coefficient associated with mode shape W_i,

$$\theta_i = \int_{v_p} \frac{e}{t_p} y_p W_i'' \, dv \tag{5.14}$$

e is the piezoelectric coupling coefficient, and t_p is the thickness of PZT film.

The electrical properties of the flexible-beam energy harvester for multi-mode can be expressed as

$$\sum_{i=1}^{n} \theta_i q_i + C_p V_p = Q \tag{5.15}$$

where C_p is piezoelectric capacitor, V_p is electrical voltage over PZT film, and Q is charge generated from PZT film.

The flexible-beam structure is vibrated by the base excitation. Since it's a distributed structure, the virtual work for a single mode caused by the inertia force from the base excitation can be expressed as

$$\int_r f W_i(r)\,dr = \int_0^{L_b} \rho_b A_b a_{base} W_i(r)\,dr + \int_0^{L_p} \rho_p A_p a_{base} W_i(r)\,dr + m a_{base} W_i(L_b) =$$
$$\left[\rho_b A_b \int_0^{L_b} W_i(r)\,dr + \rho_p A_p \int_0^{L_p} W_i(r)\,dr + m W_i(L_b)\right] a_{base} = \varphi_f^{(i)} a_{base} \quad (5.16)$$

where $\varphi_f^{(i)}$ is the coefficient associated with mode shape W_i:

$$\varphi_f^{(i)} = \left[\rho_b A_b \int_0^{L_b} W_i(r)\,dr + \rho_p A_p \int_0^{L_p} W_i(r)\,dr + m W_i(L_b)\right] \quad (5.17)$$

For multi-mode modeling of the flexible-beam, the state is chosen to be $x = [q_1, q_2, \cdots, q_n, \dot{q}_1, \dot{q}_2, \cdots, \dot{q}_n]^T$. Including the mechanical damping in the system, i.e., $\boldsymbol{C}_{n\times n}$, the multi-mode state-space model is

$$\dot{x} = \begin{bmatrix} \mathbf{0}_{n\times n} & \boldsymbol{I}_{n\times n} \\ -\boldsymbol{M}_{n\times n}^{-1}\boldsymbol{K}_{n\times n} & -\boldsymbol{M}_{n\times n}^{-1}\boldsymbol{C}_{n\times n} \end{bmatrix} x + \begin{bmatrix} \mathbf{0}_{n\times 1} & \mathbf{0}_{n\times 1} \\ \boldsymbol{M}_{n\times n}^{-1}\boldsymbol{\theta}_{n\times 1} & -\boldsymbol{M}_{n\times n}^{-1}\boldsymbol{\varphi_f}_{n\times 1} \end{bmatrix} \begin{bmatrix} V_p \\ a_{base} \end{bmatrix} \quad (5.18)$$

where $\boldsymbol{M_{n\times n}}$ is the mass matrix of n modes with the ij-th element in Eq. (5.8), $\boldsymbol{K_{n\times n}}$ is the stiffness matrix with the ij-th element in Eq. (5.9), $\boldsymbol{\theta}_{n\times 1}$ is the electromechanical coupling coefficient vector with the i-th element θ_i in Eq. (5.14), and $\boldsymbol{\varphi_f}_{n\times 1}$ is the force coefficient vector with the i-th element $\varphi_f^{(i)}$ in Eq. (5.17).

5.3 Vibration Control and SPCI Circuit Implementation

5.3.1 H_2 control

Since H_2 control is suitable for wide frequency range vibration control, such as random vibration excitation used in this paper. Note that the proposed SPCI method can also be used for the self-powered implementation of other control algorithms, including H_∞ control.

Referring to the state-space model in Eq. (5.18), the standard form for state-space control is

$$\dot{x} = Ax + B_1 w + B_2 u \quad (5.19)$$
$$z = C_1 x + D_{11} w + D_{12} u \quad (5.20)$$
$$y = C_2 x + D_{21} w + D_{22} u \quad (5.21)$$

where the state $x = [q_1, q_2, \cdots, q_n, \dot{q}_1, \dot{q}_2, \cdots, \dot{q}_n]^T$; the disturbance $w = a_{base}$; the "control force" $u = V_p$; the "cost output" z is chosen as the absolute acceleration of the tip on the beam-PZT, for the situations that we care more about minimizing the absolute vibration of the flexible structures, such as protecting human beings in a tall building during an earthquake, stabilizing cameras in a vibrating structure for clear images of the environment, etc.; the "measurement output" y is also the absolute acceleration of the tip on the beam-PZT, since it is an easily measured parameter that can reflect the vibration of the beam.

The control effect will be

$$u = K_f y \tag{5.22}$$

where K_f is the control matrix, which is used to determine the "control force" from the "measurement output".

The state-space output-feedback-control diagram is as shown in Figure 5.2. In order to minimize the vibration of flexible structures under a random vibration excitation, H_2 control algorithm is applied here, since the physical meaning of H_2 control is minimizing the root mean square values in random excitations.

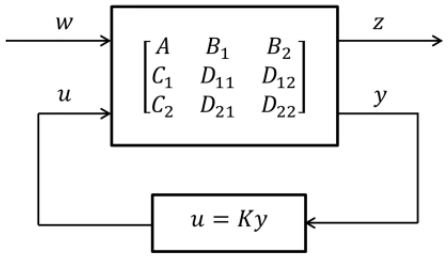

Figure 5.2 State-space control diagram

By using the output feedback H_2 control algorithm, the desired values of "control force", i.e., piezoelectric voltage, can be obtained. However, quite different from the regular control, how to implement such a desired control voltage in a manner of energy harvesting way is quite challenging. For this purpose, we presented switch pre-charged inductor (SPCI) circuit technique and a novel control implementation in the following sections.

5.3.2 SPCI technique principle

Considering a LC resonant circuit (as shown in Figure 5.3) with initial capacitor voltage $V_{initial}$ and initial inductor current $I_{initial}$, the expression of capacitor voltage V_c during the LC resonance process is

$$V_c(t) = V_{initial}\cos\left(\frac{1}{\sqrt{LC}}t\right) - I_{initial}\sqrt{\frac{L}{C}}\sin\left(\frac{1}{\sqrt{LC}}t\right) = \sqrt{{V_{initial}}^2 + {I_{initial}}^2\frac{L}{C}}\cdot\sin(\varphi - \frac{1}{\sqrt{LC}}t) \quad (5.23)$$

where $\varphi = tan^{-1}(\frac{V_{initial}}{I_{initial}}\sqrt{\frac{C}{L}})$.

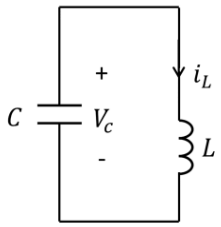

Figure 5.3 LC resonant circuit

We can find that the capacitor voltage can be controlled to be any value in the range of $-\sqrt{{V_{initial}}^2 + {I_{initial}}^2\frac{L}{C}}\ to\ \sqrt{{V_{initial}}^2 + {I_{initial}}^2\frac{L}{C}}$ by switching the circuit off at appropriate time. Moreover, the controllable range of capacitor voltage can be extended by setting the initial inductor current, $I_{initial}$, which can be realized by pre-charging the inductor.

Denote the desired capacitor voltage as $V_{desired}$, according to Eq. (5.23),

$$|V_{desired}| = \sqrt{{V_{initial}}^2 + {I_{initial}}^2\frac{L}{C}} \quad (5.24)$$

therefore, the inductor current should be pre-charged to

$$I_{initial} = \pm\sqrt{\frac{C}{L}({V_{desired}}^2 - {V_{initial}}^2)} \quad (5.25)$$

where "+" is for the situation when $V_{desired}\cdot V_{initial} < 0$, "-" is for the situation when $V_{desired}\cdot V_{initial} > 0$.

5.3.3 Circuit implementation with SPCI technique

In order to realize the desired "control force", i.e., piezoelectric voltage, we were inspired to build a LC resonant circuit with controllable pre-charging capability, where the capacitor C is the piezoelectric capacitor. A switch is connected in series with L and C to control the capacitor voltage to a desired value. The circuit is so-called "SPCI-based implementation circuit", which is integrated into the whole system. The schematic of the self-powered control system is shown in Figure 5.4.

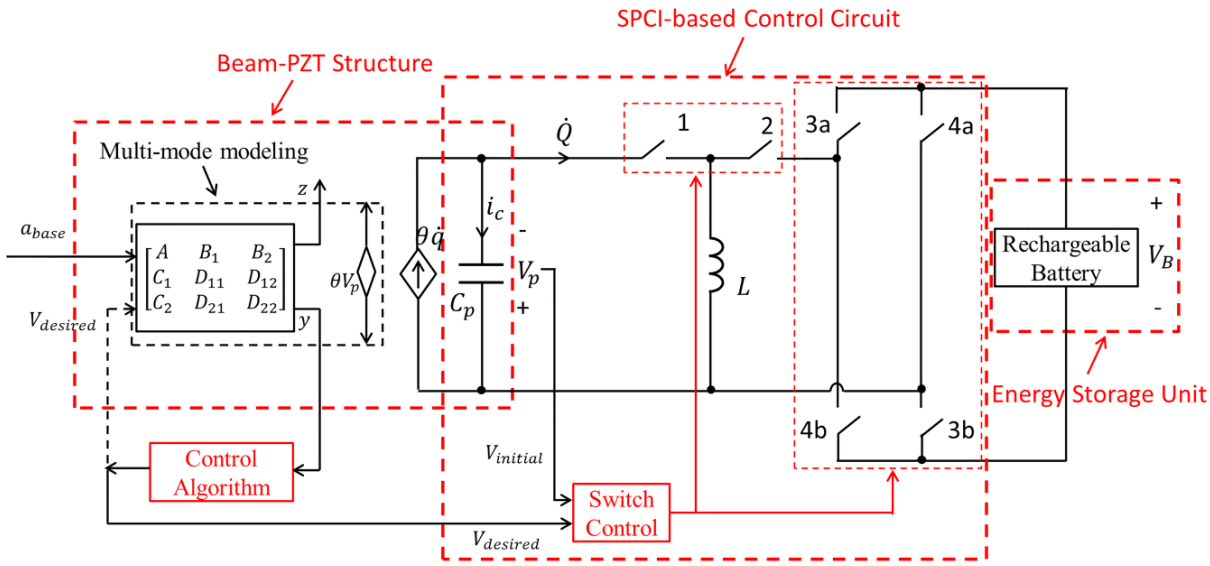

Figure 5.4 Schematic of the proposed system

The system is comprised of four parts, i.e., beam-PZT structure, H_2 control algorithm, SPCI-based implementation circuit, and energy storage unit. For the "beam-PZT structure" part, the multi-mode model is based on Eqs. (5.19)~(5.21) and Eq. (5.15), where $\theta\dot{q}$ is the current source dependent on the vibration dynamics of the beam-PZT structure. For the "H_2 control algorithm" part, the input is the measurement of the absolute acceleration of beam tip, and the output is the desired values of control voltage, which will be realized by the "SPCI-based implementation circuit". For the "SPCI-based implementation circuit" part, it is comprised of $L - C_p$ resonance circuit with switch 1, switch 2, a H-bridge with two groups of switches, i.e., 3a&3b, 4a&4b, and switch control logic. The switch control logic determines the on-off states of all the switches. The working principle of the control logic is shown in Figure 5.5. In Figure 5.5, the dependent current source with C_p is the equivalent electrical model of beam-PZT structure. There are three kinds of situations, i.e., (1) $V_{desired} \cdot V_{initial} < 0$ and $|V_{desired}| > |V_{initial}|$, (2) $V_{desired} \cdot V_{initial} > 0$ and $|V_{desired}| > |V_{initial}|$, (3) $|V_{desired}| < |V_{initial}|$. For Figure 5.5(b) and Figure 5.5(c), the inductor current is firstly pre-charged to $I_{initial}$, determined by Eq. (5.25). At $t = t_1$, the LC resonant circuit is controlled to start oscillating. When the inductor current crosses zero at $t = t_2$, $V_p = V_{desired}$, the switch between L and C is controlled to be open. For Figure 5.5(d), at $t = t_1$, the LC resonant circuit is controlled to start oscillating. Detecting the piezoelectric voltage, when $V_p = V_{desired}$, the switch between L and C is controlled to be open. For the "energy storage unit", it stores the electrical energy converted from the mechanical

vibration of the beam structure, and also provides electrical energy to pre-charge the inductor in the SPCI-based implementation circuit.

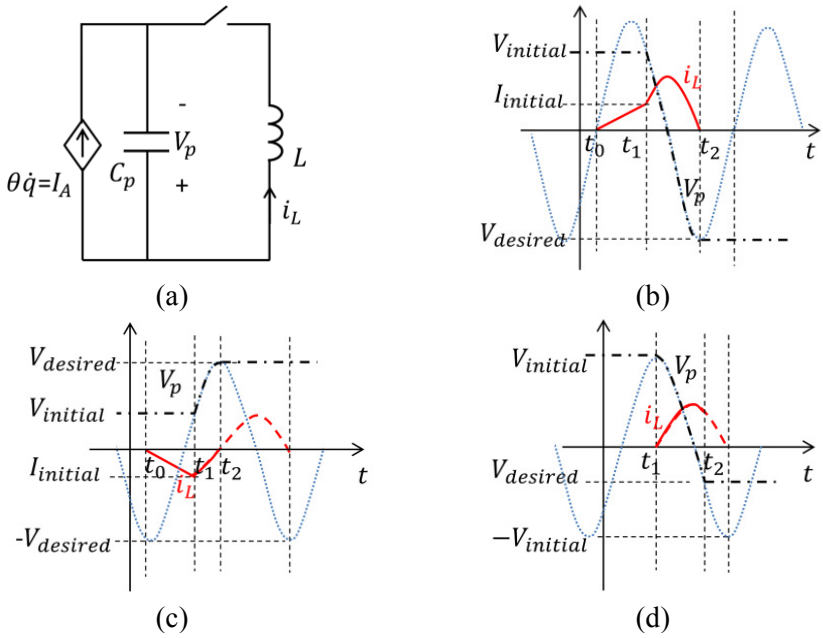

Figure 5.5 Control logic for SPCI-based circuit (a) in different situations, i.e., (b) if $\boldsymbol{V_{desired} \cdot V_{initial} < 0}$ and $|\boldsymbol{V_{desired}}| > |\boldsymbol{V_{initial}}|$, (c) if $\boldsymbol{V_{desired} \cdot V_{initial} > 0}$ and $|\boldsymbol{V_{desired}}| > |\boldsymbol{V_{initial}}|$, (d) if $|\boldsymbol{V_{desired}}| < |\boldsymbol{V_{initial}}|$. The sinusoidal dot line in (b)-(d) represents the capacitor voltage during the LC resonance process when the switch in (a) is always on, corresponding to Eq. (5.23). The dash-dot lines refer to the voltage on the capacitor C_p, and the solid lines refer to the current in the inductor L. The dash line in (c) and (d) represents the inductor current when the switch is always on.

According to SPCI technique principle, the piezoelectric voltage is controlled to desired value in less than half resonant period of LC resonant circuit, i.e., $\pi\sqrt{LC_p}$. The dominant modes of beam vibration are generally in the range of several Hz to several kHz, that is to say, the control bandwidth of the flexible structures is at the time scale of 10^{-3} sec. So we set the value of $\pi\sqrt{LC_p}$ much smaller by selecting the right L (we set 1mH in the following simulation) according to the piezoelectric capacitance C_p (298nF for the piezoelectric transducer used in the simulation) such as at time scale of 10^{-5} sec. Therefore, for each process of controlling the piezoelectric voltage from initial value to desired value, the vibration induced current source $\theta\dot{q}$ can be treated as constant, i.e., $\theta\dot{q} = I_A = constant$. The desired value of piezoelectric voltage in Figure 5.5(b) and Figure 5.5(c) is the peak value of capacitor voltage in the LC resonant circuit, which is captured by detecting the inductor current crossing zero. In Figure 5.5(d), the desired value of piezoelectric voltage is captured by directly detecting the capacitance voltage to

attain the desired value. In this way, the realization of control voltage will not be influenced by the uncertainties of circuit elements.

The switches in the system can be realized by using power MOSFETs, such as ZXMC10A816N8. Since the switches only need to be turned on or off when the capacitor voltage or the inductor current satisfy the conditions shown in Figure 5.5, the switching frequency can be lower than the conventional PWM-based techniques.

5.3.4 Energy balance analysis

The instant power to the piezoelectric transducer is

$$P = V_p \dot{Q} \tag{5.26}$$

where V_p is the piezoelectric voltage, and $\dot{Q}$ is the electric current passing through switch 1, as shown in Figure 5.4. At an instant time, the proposed SPCI based control can give energy to or harvest energy from the piezoelectric transducer. In order to analyze the self-powered ability of the proposed vibration control system, the accumulated energy given to the piezoelectric transducer should be evaluated. If accumulated energy in long term is negative, we harvest energy from the vibration structure, and the control system can be self-powered [168] with a self-starting or pre-charged circuit.

5.4 Results of Illustrative Example

5.4.1 Structural parameters

The material properties and the dimensions of the Aluminum beam and the PZT film are shown in Table 5.1. The tip mass on the beam is 0.0885kg.

Table 5.1 Material Properties and Dimensions

Material properties	**Young's modulus** (E_p , N/m^2)	**Piezoelectric strain coefficient** (d_{31} , m/V)	**Piezoelectric voltage coefficient** (g_{31}, Vm/N)	**Density** (ρ, kg/m^3)	**L × b × t** (mm×mm×mm)
PZT film (PSI-5H4E)	62×10^9	-320×10^{-12}	-9.5×10^{-3}	7800	72.4×25.4×0.19
Aluminum beam (Alloy 3003)	69×10^9	-	-	2740	406.4×25.4×3.2

5.4.2 Results of H_2 control

Assuming the mechanical damping in the flexible cantilever beam system is 0.5%, based on the H_2 control algorithm, the frequency response of the absolute acceleration of the beam tip

over the base excitation acceleration, i.e., $\frac{a_{beam\ tip}}{a_{base}}$, in the uncontrolled system and the controlled system are compared in Figure 5.6. The dominant first three modes are considered, which is in the frequency range of 1Hz~1kHz. It can be seen that the vibration of the beam is significantly reduced in the first three modes.

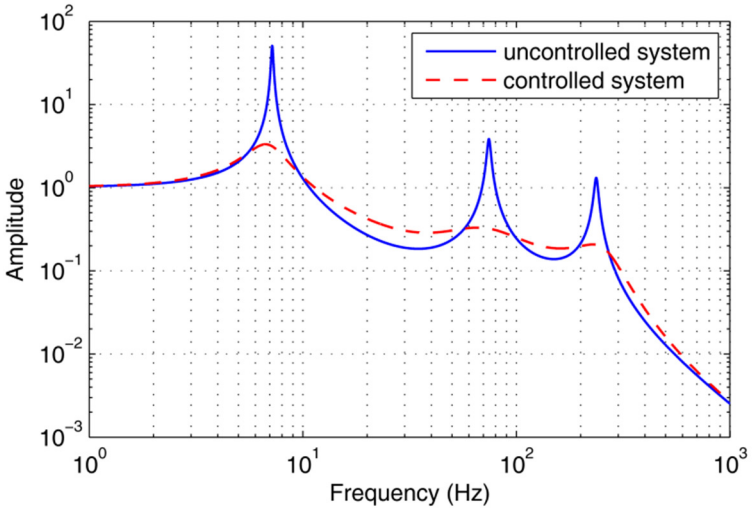

Figure 5.6 Frequency response of $\frac{a_{beam\ tip}}{a_{base}}$

5.4.3 Control Performance of the proposed system

Based on the dimensions of the piezoelectric transducer we chose, as listed in Table 5.1, the piezoelectric capacitance is 298nF. Based on the resonant circuit control time requirement stated in Section III.C, the inductor is chosen to be 1 mH.

In practical circuit, it is inevitable to have electrical loss, which might be caused by the parasitic resistance in inductor and on-resistance in switch. The typical parasitic resistance of 1mH inductor is 0.2 Ω, and the typical on-resistance of MOSFET switch with ns-level delay is 0.3 Ω, which can be seen in the datasheets of the electrical components.

Since H_2 control is to minimize vibration energy in a large frequency range, we choose a normally distributed white noise random signal as the base vibration excitation, as shown in Figure 5.7. The standard deviation of the acceleration of random excitation is 1.84 m/s^2.

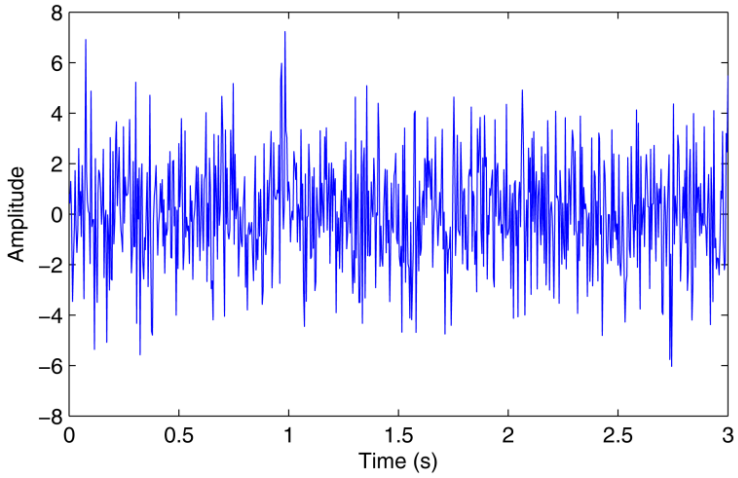

Figure 5.7 Random vibration excitation from the base

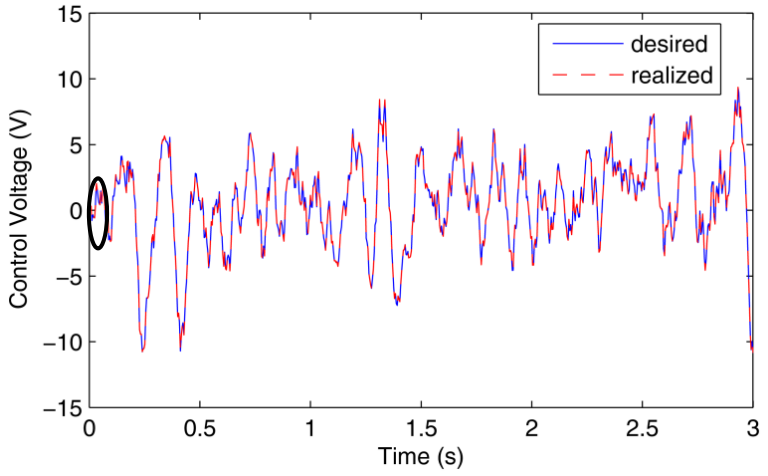

(a)

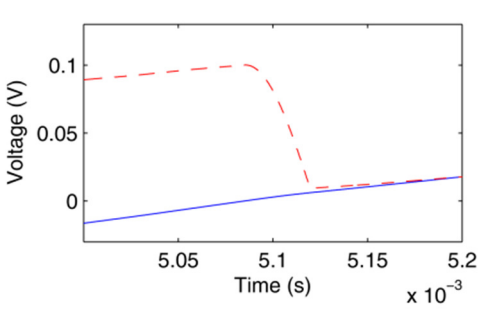

(b)

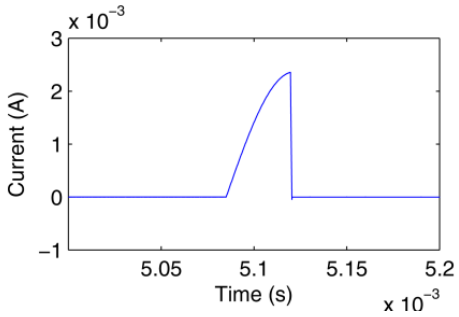

(c)

Figure 5.8 Desired control voltage v.s. Realized control voltage, (a) Tracking performance of control voltage by using SPCI-based method, (b) Enlarged control voltage $\boldsymbol{V_p}$, and (c) Enlarged Inductor current $\boldsymbol{i_L}$ of the circled portion in (a)

The comparison between the desired "control force" from H_2 control algorithm and the realized "control force" from the SPCI-based implementation circuit is shown in Figure 5.8. It

indicates that the realized "control force" tracks the values of desired "control force" very well, which verifies the feasibility of the proposed novel implementation method to generate desired capacitor voltage by using SPCI technique.

An enlarged process is shown in Figure 5.8(b) and Figure 5.8(c). Figure 5.8(b) shows the desired & the realized "control force", while Figure 5.8(c) shows the inductor current. From Figure 8b, we can see that the initial condition is: the piezoelectric voltage is larger than the desired value, corresponding to $|V_{desired}| < |V_{initial}|$. The process in Figure 5.8(b) and 5.8(c) matches the theoretical analysis in Figure 5.5(d). The comparison of the absolute accelerations of beam tip in the uncontrolled system and in the proposed control system is shown in Figure 5.9. We can see that the beam tip vibration has been effectively attenuated under the white-noise random excitation by using the proposed control method.

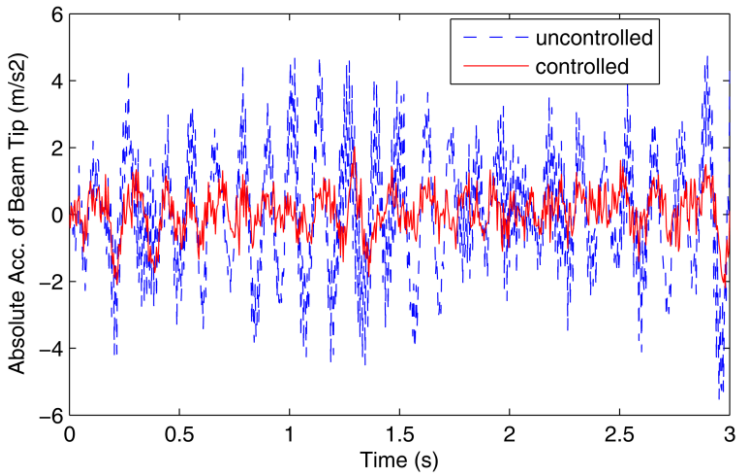

Figure 5.9 Acceleration of beam tip in uncontrolled system v.s. proposed control system

5.4.4 Results of self-power analysis

The accumulated energy given from the controller can be calculated by integrating the power expressed in Eq. (5.26). The dissipatedness can be seen in Figure 5.10. We can see that in the beginning time period the controller either gives or extracts energy, but overall the controller harvest more energy after some time. It indicates that the control system can realize self-power performance.

During the vibration process, the current charging the rechargeable battery and the accumulated energy harvested in the battery is shown in Figure 5.11. The positive parts of current represent the electrical energy converted from the mechanical vibration is harvested by charging the rechargeable battery, while the negative parts represent the battery pre-charges the

inductor in the system to make the control voltage track the desired values. It shows that at the beginning time the harvested energy is not enough for the energy consumption in the controller. But in long time the accumulated energy harvested from beam vibration is more than that consumed by the control circuit, and the electrical energy is increasing in the rechargeable battery. It matches the result in Figure 5.10. The slope of the energy curve represents the power, around 0.2mW under 1.84 m/s^2 standard deviation of random vibration for the flexible beam with dimensions shown in IV.A section. Thus, the proposed self-powered piezoelectric vibration control system can not only provide sufficient real-time energy for itself control use, but also store electrical energy for future use.

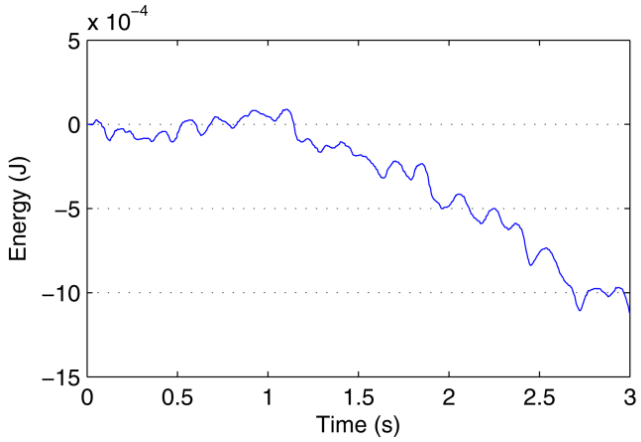

Figure 5.10 Accumulated energy given by the controller

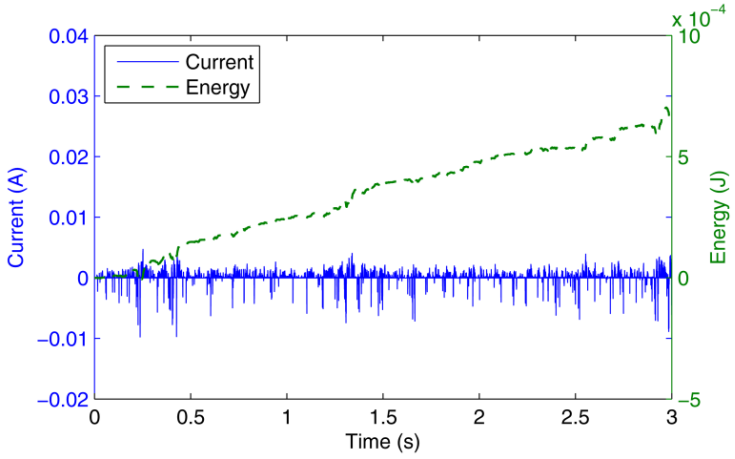

Figure 5.11 Charging battery current & harvested energy with small excitation

When the base excitation is increased, the harvested energy from the proposed system is supposed to be more. We doubled the base random excitation to that with the standard deviation of 3.68 m/s^2. The accumulated energy in the first three seconds are shown in Figure 5.12 in

comparison with smaller excitation (standard deviation = 1.84 m/s^2). With larger excitation, the power is around 0.7mW, while the power is 0.2mW with small excitation.

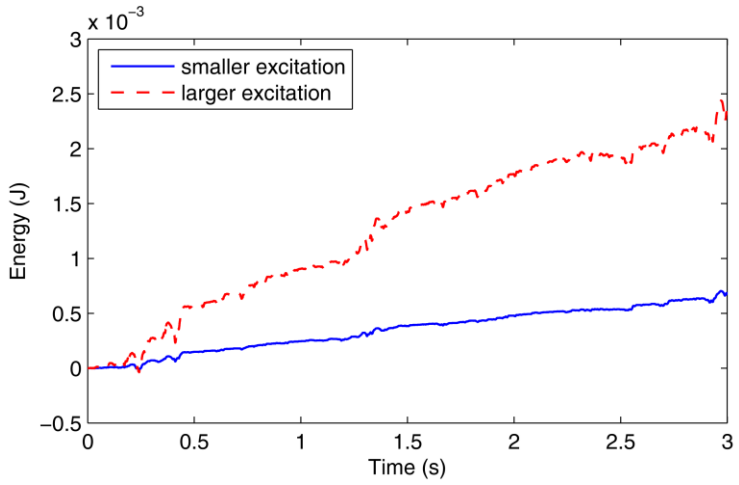

Figure 5.12 Comparison of accumulated energy with smaller excitation v.s. larger excitation

5.4.5 Energy loss study on parasitic resistances

Due to different properties of electronic components, the parasitic resistances in different kinds of switches and inductors exist. The influence of resistance on the proposed system is that larger resistance will result in slower charging and discharging processes in the R-L-series circuit, which may influence the voltage tracking bandwidth and values. The parasitic energy loss will also reduce the harvested energy. The power loss caused by one parasitic resistance can be expressed as

$$P_{loss} = \frac{\sum_{i=1}^{N} I_i^2}{N} R \tag{5.27}$$

where N is the number of sample points, which is the product of sampling frequency and record time, and R is the parasitic resistance.

The simulation study of energy loss in the proposed self-powered control system with different parasitic resistances is conducted. As mentioned in Section IV.C, the typical parasitic resistance of 1mH inductor is 0.2Ω and the typical on-resistance MOSFET switch with ns-level delay is 0.3Ω, we studied on four different resistances on both inductor and switches, i.e., $0.1 \times R_{typ}$, $1 \times R_{typ}$, $10 \times R_{typ}$, and $50 \times R_{typ}$, where R_{typ} represents typical resistance. In order to determine the influence of parasite resistances on the total accumulated energy in the self-powered system, four different parasitic resistances v.s. accumulated energy are compared in Figure 5.13. We can see that the accumulated energy and the harvested power are smaller with

larger resistance, which verifies that larger resistance consumes more energy. According to Eq. (5.27), the power loss with resistance of $10 \times R_{typ}$ is around 4μW, which is 2% of the total power generation, so it is not obvious in the figure, while the power loss with resistance of $50 \times R_{typ}$ is around 20 μW, which is 10% of the total power generation, so we can clearly see the difference.

However, the resistance cannot be too large. In the R-L-series circuit the inductor current can be expressed as

$$i_L(t) = -\frac{V_B}{R} e^{-\frac{R}{L}t} + \frac{V_B}{R} \tag{5.28}$$

where V_B is the battery voltage, which can be seen as constant, since it is assumed to be fully charged. From Eq. (5.28) we can know that the inductor current can only be charged to $\frac{V_B}{R}$. If R is too large, the inductor current cannot be pre-charged to desired value required by the desired control voltage in Eq. (5.25).

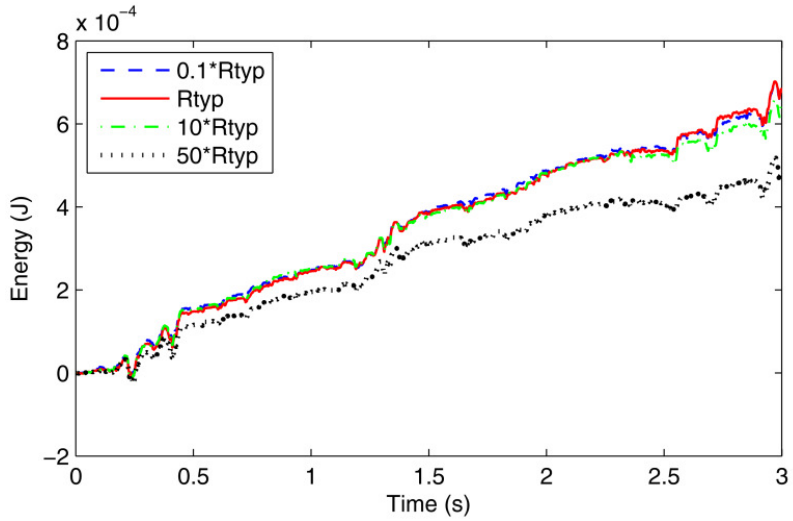

Figure 5.13 Comparison of harvested energy with different parasitic resistances

5.5 CONCLUSIONS

In this chapter, a self-powered piezoelectric vibration control system with switch pre-charged inductor (SPCI) technique is proposed. It can simultaneously minimize the vibration of the flexible beam and harvest the vibration energy. A novel SPCI-based circuit is presented to implement the desired "control force" in a self-powered manner, the values of which are obtained by using the output feedback H_2 control algorithm. The simulation results show that under a white-noise random excitation, the realized "control force" can track the desired values

very well, the vibration of the beam can be effectively attenuated, and the accumulated harvested energy is more than the consumed energy in the system. The harvested power is around 0.2mW under 1.84 m/s^2 and around 0.7mW under 3.68 m/s^2 standard deviation of white-noise random excitation for the studied flexible beam. In addition to the simultaneous vibration control and energy harvesting, a significant advantage of the proposed method over the PWM-based methods is that it facilities decent voltage tracking with switching frequencies much lower than PWM-based techniques, by employing discontinuous conduction and LC resonant circuit.

Chapter 6 Vibration and Wave Propagation Attenuation for Metamaterials by Periodic Piezoelectric Arrays with High-Order Resonant Circuit Shunts

6.1 MOTIVATION

Metamaterials, assemblies of multiple individual elements constructed into repeating patterns, have attracted more and more attention in recent years. The technology is originally developed for electromagnetic and optical wave propagation purpose and later extended to mechanical and acoustic waves. A type of phononic crystal with periodic arrangement for generating band gaps has been studied in the last decade. Wu, *et al.* [169] numerically and experimentally demonstrated the existence of complete bandgaps and resonances in a plate with a periodic stubbed surface. They designed a typical type of stubs with the height about three times the plate thickness, which has the ability of generating a bandgap between 114kHz to 145kHz. Later, researchers explored Wu's design by adopting piezoelectric materials into the periodic structure. Bergamini, *et al.* [170] introduced a phononic crystal that includes tunable stiffness elements to obtain a variable mechanical coupling between the substrate and the stubs on the beam. The phononic crystal is comprised of cylindrical stubs and piezoelectric discs. Each piezoelectric transducer is shunted through an inductive circuit in order to obtain the frequency dependent stiffness elements. The proposed structure has the ability of generating a pass band among the original stop bands, with the location determined by the inductive shunts. Casadei, *et al.* [171] investigated a tunable acoustic waveguide implemented within a two-dimensional phononic plate. The wave guide is equipped with a periodic array of piezoelectric transducers shunted through passive inductive circuits. The inductor in the RL-shunt with the piezoelectric capacitance can tune the wave propagation frequency. Carrara, *et al.* [172] exploited metamaterial-based and metamaterial-inspired electroacoustic wave energy harvesting. The metamaterial energy harvesting systems transform the incoming structure-borne wave energy into electrical energy by coupling the metamaterial and electroelastic domains. The metamaterial system is combined with piezoelectric energy harvesting for enhanced electricity generation from waves propagation in elastic structures.

Since piezoelectric is a special type of material which links mechanical characteristics with electrical characteristics, the shunt circuit plays a key role on the wave propagation and/or vibration control performance in the metamaterials. Thorp, *et al.* [173] periodically placed shunted piezoelectric patches along rods to control the longitudinal wave propagation in the rods.

The periodic structure is capable of filtering the propagation of waves over specified frequency bands, called "stop bands". They also extended the technology for attenuation of wave propagation in fluid-loaded shells with periodic shunted piezoelectric rings [174]. Beck, *et al.* [175] introduced negative capacitance to the periodic piezoelectric shunt. The negative capacitance shunt can be designed to control broadband flexural vibrations of a structure. Spadoni, *et al.* [176] employed periodic arrays of shunted, piezoelectric patches to control wave propagation and vibration over the surface of plate structures. Both R-shunt and RL-shunt were studied. Casadei, *et al.* [177] proposed a hybrid shunted piezoelectric arrays for plate vibration control, in which the combination of resonant RLC shunts and negative impedance converters on a two-dimensional plate, which provides both broadband attenuation in the high frequency regimes and the reduction of the amplitudes of the low frequency modes. Airoldi and Ruzzene [178] investigated the wave propagation control performance in beams through periodic, shunted piezoelectric patches. The patches are shunted through resonant circuits featuring a single and multiple resonances. However, the existing piezoelectric shunts for metamaterials are R-shunt, RL-shunt or negative impedance shunt. Few research has been conducted on high-order resonant shunt circuit in the metamaterial area.

This chapter introduces an innovative type of metamaterials with high-order resonant shunt circuit for the periodic piezoelectric arrays bonded on a beam. The high-order resonant shunt circuit will advance the metamaterials with conventional RL-shunt and R-shunt in two aspects. One is that it can generate broader attenuation bandwidth without sacrificing the attenuation amplitude by introducing two local resonances in series. The other is that the high-order resonant shunt circuit can generate two separate bandgaps with well-designed inductance ratio and damping ratio, achieving wave propagation or vibration attenuation at two desired frequency ranges.

6.2 THEORETICAL ANALYSIS

6.2.1 Finite element modeling of beam metamaterial with periodic piezoelectric arrays

The schematic diagram of beam metamaterial with piezoelectric shunts is shown in Figure 6.1. The beam is covered by periodically distributed piezoelectric films. Each piezoelectric film is shunted with the same external circuit. Different shunt circuits will result in different wave propagation attenuation performances. Therefore, the objective of this paper is to

investigate the vibration and wave propagation attenuation performances with different piezoelectric shunts.

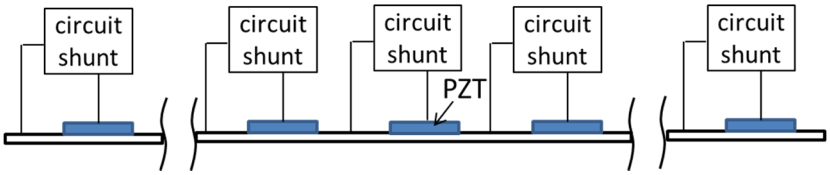

Figure 6.1 Schematics of beam metamaterial with periodic piezoelectric arrays

Note that the finite element modeling is for wave propagation and vibration in the transverse direction. The beam metamaterial in Figure 6.1 is comprised of many periodic unit cells. Each unit cell is as shown in Figure 6.2(a), which can be divided into *n* elements, each with two nodes. Each node has two coordinates: one is transverse coordinate, denoted as u, which represents the transverse displacement of the beam structure, and the other is rotational coordinate which represents the slope motion of the beam structure, denoted as $\frac{\partial u}{\partial x}$. Corresponding to the two coordinates at each node, u and $\frac{\partial u}{\partial x}$, there are two external forces, i.e., shear force and bending moment, respectively.

(a) (b)

Figure 6.2 Beam metamaterial, (a) unit cell, and (b) each element with two nodes, each node has two coordinates

Based on energy equilibrium analysis, the formulation of energy equations for the unit cell of the beam metamaterial can be expressed as

$$\Pi = \frac{1}{2}\int \rho \dot{\boldsymbol{u}}_c{}^T \dot{\boldsymbol{u}}_c \, dV + \frac{1}{2}\int \boldsymbol{\varepsilon_c^T \sigma} \, dV + \int \boldsymbol{\varepsilon_c^T \sigma_p} \, dV - \frac{1}{2}\int \boldsymbol{E}^T \boldsymbol{D} \, dV - W_e \tag{6.1}$$

where ρ is the density, $\boldsymbol{u}$ is the displacement vector, $\boldsymbol{\varepsilon}$ is strain, the subscript "$_c$" represents the unit cell, V is the volume of the unit cell, $\boldsymbol{\sigma}$ is stress in the beam, $\boldsymbol{\sigma_p}$ is stress in the piezoelectric material, $\boldsymbol{E}$ and $\boldsymbol{D}$ are electric field and electric charge of piezoelectric material, respectively. W_e is the work done by external force.

The constitutive equations for piezoelectric material are [179]

$$\begin{bmatrix} \sigma \\ D \end{bmatrix} = \begin{bmatrix} c^E & -e^\sigma \\ e & \epsilon^\varepsilon \end{bmatrix} \begin{bmatrix} \varepsilon \\ E \end{bmatrix} \tag{6.2}$$

where c^E is mechanical stiffness coefficient at constant electric field, e^σ is piezoelectric stress coupling coefficient at constant stress, ϵ^ε is permittivity coefficient at constant strain, e is piezoelectric stress coupling coefficient.

Electro-elastic matrix relations for a finite element are obtained by expressing continuous displacements, strains and electric potentials in terms of nodal values through a proper set of interpolation functions and their derivatives [180], as

$$\begin{aligned} \boldsymbol{u_e} &= \boldsymbol{N d_e} \\ \boldsymbol{\varepsilon_e} &= \boldsymbol{B_u d_e} \\ E &= -B_\phi \phi \end{aligned} \tag{6.3}$$

where $\boldsymbol{d}$ is the generalized nodal displacements, the subscript "e" represents the element, $\boldsymbol{d_e} = \left[u_1 \quad \frac{\partial u_1}{\partial x} \quad u_2 \quad \frac{\partial u_2}{\partial x}\right]^T$, u_1, u_2 are shown in Figure 6.2(b), $\boldsymbol{N}$ is the shape function matrix, with dimension of 4×4, $\boldsymbol{B_u}$ is the strain interpolation matrix, with dimension of 4×1, B_ϕ is the electric field interpolation matrix, ϕ is the electric potential over the piezoelectric film, which is opposite to the piezoelectric voltage, $\boldsymbol{u_e}$ is the displacement vector of element, with dimension of 4×1.

Since $E = -\frac{\phi}{t_p}$, from Eq. (6.3) we know that

$$B_\phi = \frac{1}{t_p} \tag{6.4}$$

where t_p is the thickness of the piezoelectric film.

Energy equilibrium is imposed by enforcing the total potential to be at a minimum,

$$\delta \Pi = 0 \tag{6.5}$$

Combining Eqs. (1) ~ (3) and substituting into Eq. (5), the modeling of the electro-elastic unit cell with *n* elements can be expressed as [176]

$$\boldsymbol{M_{uu\_c}} \ddot{\boldsymbol{d}}_c + \boldsymbol{K_{uu\_c} d_c} + \boldsymbol{K_{u\phi\_c}} \phi = \boldsymbol{f_c} \tag{6.6}$$

$$\boldsymbol{K_{\phi u\_c} d_c} + K_{\phi\phi} \phi = Q \tag{6.7}$$

where $\boldsymbol{d_c}$ is the generalized nodal displacements of all the nodes in the unit cell, with dimension of $2(n+1) \times 1$, the structural mass matrix of unit cell $\boldsymbol{M_{uu\_c}}$, with dimension of $2(n+1) \times 2(n+1)$, the structural stiffness matrix of unit cell $\boldsymbol{K_{uu\_c}}$, with dimension of $2(n+1) \times 2(n+1)$, and the electromechanical coupling vector of unit cell $\boldsymbol{K_{u\phi\_c}}$, with dimension of $2(n+1) \times 1$, are the sum and integration of mass matrix of element $\boldsymbol{M_{uu\_e}}$, with dimension of 4×4,

stiffness matrix of element $\boldsymbol{K_{uu\_e}}$, with dimension of 4×4, and electromechanical coupling vector of element, with dimension of 4×1, respectively,

$$\boldsymbol{M_{uu\_e}} = \int \rho \boldsymbol{N}^T \boldsymbol{N}\, dV \tag{6.8}$$

$$\boldsymbol{K_{uu\_e}} = \int \boldsymbol{B_u^T} \bar{c} \boldsymbol{B_u}\, dV \tag{6.9}$$

$$\boldsymbol{K_{\phi u\_e}^T} = \boldsymbol{K_{u\phi\_e}} = \int \boldsymbol{B_u^T} e \boldsymbol{B_\phi}\, dV \tag{6.10}$$

$$\bar{c} = \frac{1}{12} Y t^2 \tag{6.11}$$

where Y is the Young's Modulus, and t is the thickness of the beam structure.

The dielectric stiffness is equal and opposite to the piezoelectric capacitance, C_p, that is,

$$K_{\phi\phi} = -\int B_\phi^T \epsilon^\varepsilon B_\phi\, dV = -\frac{\epsilon^\varepsilon b_p l_p}{t_p} = -C_p \tag{6.12}$$

where b_p and l_p are the width and the length of each element in unit cell, respectively.

The vector $\boldsymbol{f_c}$ (with dimension of $2(n+1) \times 1$) in Eq. (6.6) is the external distributed force exerted on all the nodes in unit cell, which is comprised of shear force and bending moment. The Q in Eq. (6.7) is the electric charge accumulated on the piezoelectric transducer.

The relationship between the electric potential ϕ and the charge Q is

$$\phi = -Z_e \dot{Q} = -j\omega Z_e Q \tag{6.13}$$

Substituting Eq. (6.13) into Eq. (6.7), we can get

$$Q = \frac{1}{1 - j\omega K_{\phi\phi} Z_e} \boldsymbol{K_{\phi u\_c}} \boldsymbol{d_c} \tag{6.14}$$

Combining Eq. (6.6), Eq. (6.13) and Eq. (6.14), we can get

$$\boldsymbol{K_{uu\_c}} \boldsymbol{d_c} + \boldsymbol{K_{u\phi\_c}} \phi = \left[\boldsymbol{K_{uu\_c}} - j\omega \boldsymbol{K_{u\phi\_c}} \left(j\omega K_{\phi\phi} - Z_e^{-1}\right)^{-1} \boldsymbol{K_{\phi u\_c}}\right] \boldsymbol{d_c} = \boldsymbol{K_f} \boldsymbol{d_c} \tag{6.15}$$

Therefore, based on Eq. (6.6) and Eq. (6.15), the final integrated stiffness matrix of the unit cell is denoted as $\boldsymbol{K_{D\_c}}$, with dimension of $2(n+1) \times 2(n+1)$, which satisfies the following dynamic equation.

$$\boldsymbol{K_{D\_c}} \boldsymbol{d_c} = \left(\boldsymbol{K_f} - \omega^2 \boldsymbol{M_{uu\_c}}\right) \boldsymbol{d_c} = \boldsymbol{f_c} \tag{6.16}$$

6.2.2 Attenuation constant and beam vibration modeling

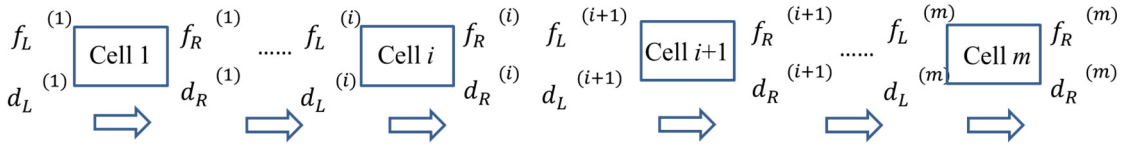

Figure 6.3 Wave/vibration propagation along the beam metamaterial

The schematic of wave/vibration propagation along the beam metamaterial is as shown in Figure 6.3. The motions $\boldsymbol{d}$ and the external forces $\boldsymbol{f}$ are propagated between adjacent unit cells. The arrows in the figure represent the wave/vibration propagation direction. For any unit cell *i*, the displacements and the forces at the left side are denoted as $\boldsymbol{d_L}$, $\boldsymbol{f_L}$, respectively, and the displacements and the forces at the right side are denoted as $\boldsymbol{d_R}$ and $\boldsymbol{f_R}$, respectively. The equation of dynamic motion of the unit cell, with only left-end node and right-end node, can be expressed in terms of the integrated stiffness matrix of the unit cell, $\widetilde{\boldsymbol{K}}_{\boldsymbol{D\_c}}$, with dimension of 4 × 4, as

$$\widetilde{\boldsymbol{K}}_{\boldsymbol{D\_c}}\widetilde{\boldsymbol{d}}_c = \tilde{\boldsymbol{f}}_c \tag{6.17}$$

where

$$\widetilde{\boldsymbol{K}}_{\boldsymbol{D\_c}} = \begin{bmatrix} \boldsymbol{\alpha_{LL}} & \boldsymbol{\alpha_{LR}} \\ \boldsymbol{\alpha_{RL}} & \boldsymbol{\alpha_{RR}} \end{bmatrix}, \widetilde{\boldsymbol{d}}_c = \begin{bmatrix} \boldsymbol{d_L} \\ \boldsymbol{d_R} \end{bmatrix}, \tilde{\boldsymbol{f}}_c = \begin{bmatrix} \boldsymbol{f_L} \\ \boldsymbol{f_R} \end{bmatrix} \tag{6.18}$$

For each unit cell, only the two end-nodes have non-zero external forces, while the forces of the other nodes are internal interactive forces which can be treated as zero. Thus, Eq. (6.16) can be rewritten as

$$\boldsymbol{K_{D\_c}}[\boldsymbol{d_L} \quad \boldsymbol{d_2} \quad \cdots \quad \boldsymbol{d_n} \quad \boldsymbol{d_R}]^T = [\boldsymbol{f_L} \quad \boldsymbol{0} \quad \cdots \quad \boldsymbol{0} \quad \boldsymbol{f_R}]^T \tag{6.19}$$

By reorganizing Eq. (6.19), we can get the terms in $\widetilde{\boldsymbol{K}}_{\boldsymbol{D\_c}}$.

In order to get the attenuation constant, we put the left side terms of unit cell, $\boldsymbol{d_L}$, $\boldsymbol{f_L}$, to one side of equator, and put the right side terms of unit cell, $\boldsymbol{d_R}$, $\boldsymbol{f_R}$, to the other side of equator [176]. Therefore, Eq. (6.17) can be rewritten as

$$\begin{bmatrix} \boldsymbol{d_R} \\ \boldsymbol{f_R} \end{bmatrix} = \boldsymbol{T} \begin{bmatrix} \boldsymbol{d_L} \\ \boldsymbol{f_L} \end{bmatrix} \tag{6.20}$$

where

$$\boldsymbol{T} = \begin{bmatrix} -\boldsymbol{\alpha_{LR}^{-1}\alpha_{LL}} & \boldsymbol{\alpha_{LR}^{-1}} \\ \boldsymbol{\alpha_{RR}\alpha_{LR}^{-1}\alpha_{LL} - \alpha_{RL}} & \boldsymbol{-\alpha_{RR}\alpha_{LR}^{-1}} \end{bmatrix} \tag{6.21}$$

The eigenvalue of matrix $\boldsymbol{T}$ is

$$eig(\boldsymbol{T}) = e^{\mu} \tag{6.22}$$

where μ is a complex number, $\mu = \delta + i\gamma$, is called "propagation constant". The real part δ is called "attenuation constant", which represents the decay of the vibration amplitude from one cell to the following one. The imaginary part γ is called "phase constant", which determines the

phase difference between two adjacent cells. Thus, δ can reflect the attenuation performance of the beam metamaterial with periodic unit cells.

Combining the integrated stiffness matrixes of all the unit cells (the number of unit cells is *m*), to form the overall integrated stiffness matrix of the whole beam, $\boldsymbol{K_D^{total}}$, with dimension of $2(mn+1) \times 2(mn+1)$,

$$\boldsymbol{K_D^{total}}[\boldsymbol{d_l} \quad \boldsymbol{d_1} \quad \cdots \quad \boldsymbol{d_{mn-1}} \quad \boldsymbol{d_r}]^T = [\boldsymbol{f_l} \quad \boldsymbol{f_1} \quad \cdots \quad \boldsymbol{f_{mn-1}} \quad \boldsymbol{f_r}]^T \tag{6.23}$$

where subscripts "l" and "r" represent the left-end and the right-end of the whole beam, respectively.

Taking cantilever beam as an example, the external force is only exerted on the fixed-end node, the shear force and the bending moment at the fixed-end are $\rho_b A_b L_b a_b$ and $\rho_b A_b \frac{L_b^2}{2} a_b$, respectively. Thus,

$$\boldsymbol{f_l} = [\rho_b A_b L_b a_b \quad \rho_b A_b \frac{L_b^2}{2} a_b]^T \tag{6.24}$$

where ρ_b, A_b, L_b are the density, the cross-section area, and the length of the cantilever beam, respectively.

From Eq. (6.23) we can get

$$[\boldsymbol{d_l} \quad \boldsymbol{d_1} \quad \cdots \quad \boldsymbol{d_{mn-1}} \quad \boldsymbol{d_r}]^T = (\boldsymbol{K_D^{total}})^{-1} \left[\rho_b A_b L_b a_b \quad \rho_b A_b \frac{L_b^2}{2} a_b \quad 0 \quad \cdots \quad 0 \quad 0\right]^T \tag{6.25}$$

By solving Eq. (6.25) we can get the relationship equation of the free-end transverse displacement over the base excitation acceleration, $\frac{u_r}{a_b}$.

6.3 High-Order Resonant Shunt Circuit Design

From the theoretical modeling of attenuation constant in the above section, we know that the attenuation constant is a parameter representing attenuation performance for beam metamaterial with any number of unit cells. Thus the shunt circuit design should also be applicable for *m*=1 case. The unit cell of beam metamaterial with RL-shunt is shown in Figure 6.4(a). For *m*=1 case, the base structure of beam can be modelled as traditional mass-spring-damper mechanical structure for any vibration mode, as shown in the dashed block in Figure 6.4(b). The piezoelectric transducer corresponds to spring k_1 in Figure 6.4(b), since piezoelectric material can be modeled as a capacitor, and mechanical spring is equivalent to electrical capacitor according to the electrical-mechanical analogy [181], with the spring stiffness

reciprocal of the capacitance. Based on the electrical-mechanical analogy, electrical resistor corresponds to mechanical damper, and electrical inductor corresponds to mechanical mass. Therefore, the mechanical model of RL-shunt is comprised of a damper, c_1, and a mass, m_1, as shown in Figure 6.4(b). f is the external force applied on the beam-PZT structure.

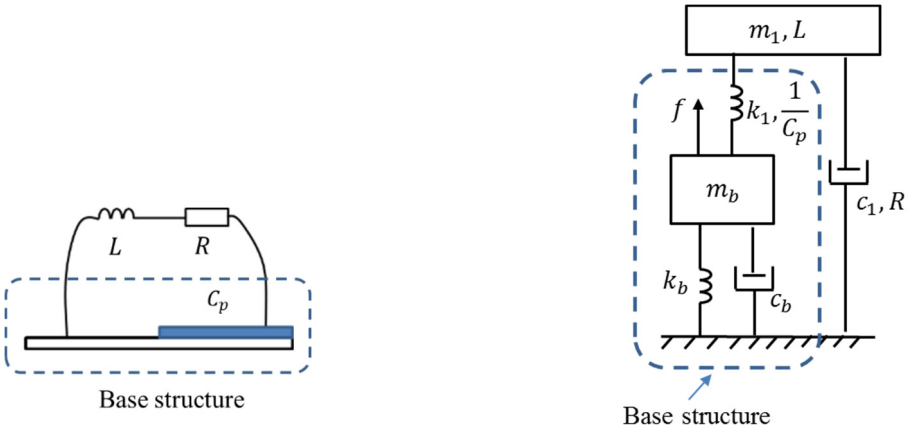

(a) (b)

Figure 6.4 Electrical-mechanical conversion, (a) unit cell with RL-shunt, (b) corresponding mechanical model.

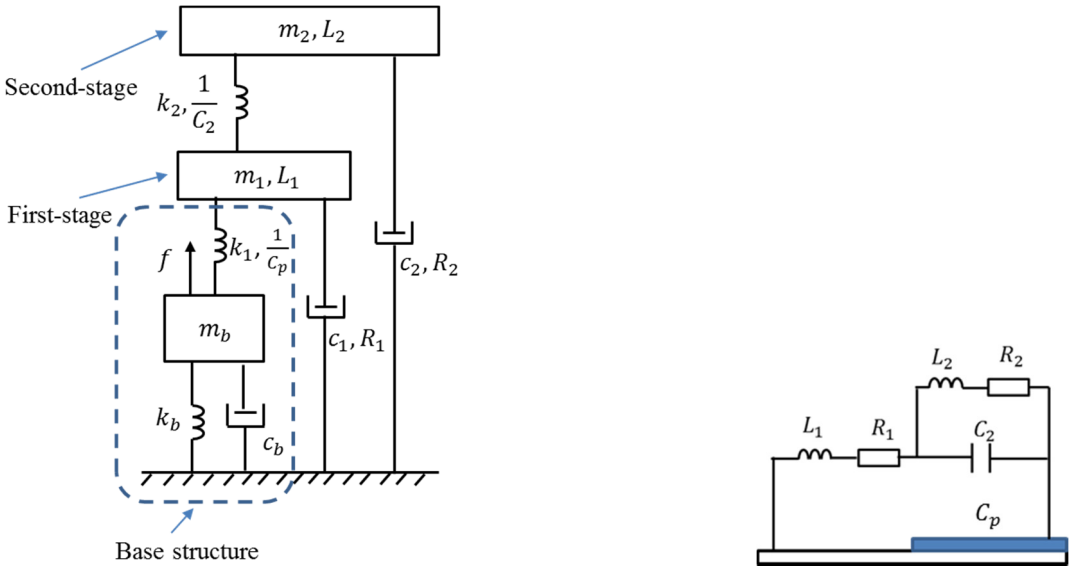

(a) (b)

Figure 6.5 Proposed high-order resonant shunt circuit, (a) mechanical model with two series resonators, (b) corresponding high-order resonant shunt circuit.

The RL-shunt design is more like a traditional tuned-mass-damper (TMD) design [182]. That is, if we choose proper L to make L-C_p have the resonant frequency the same as a natural frequency of the beam vibration, the RL-shunt will create a local resonance in the metamaterial.

Inspired by the observation that series TMDs using high-order resonant shunt circuit [183] or using double masses [184] can achieve better vibration reduction and broader attenuation bandwidth, we hypothesize that higher-order resonant shunt circuit in the metamaterials may attenuate the vibration and wave propagation better than RL-shunt, and achieve broader attenuation bandwidth. The higher-order resonant circuit shunted to piezoelectric transducer can be designed by taking electrical-mechanical analogy, as shown in Figure 6.5.

It shall be noted that shunt circuit design for beam metamaterial is not exactly TMD design since for TMD we care the frequency response but for metamaterials we care the attenuation constant of wave propagation. Another difference is: the bandgaps of wave propagation and vibration in metamaterial usually include several vibration modes or are independent on vibration modes, while TMD design always targets at certain vibration modes. Therefore, we can choose the tuning frequency to be any frequency for metamaterial, not limited to natural frequency of the whole structure.

6.4 SIMULATIONS

For the beam metamaterial with periodic piezoelectric arrays shown in Figure 6.1, the dimensions and parameters of unit cell in the simulation are: Aluminum solid with length 101.6mm, width 25.4mm, thickness 1mm, Young's Modulus 71GPa; Piezoelectric film (QuickPack QP16N) with length 50.8mm, width 25.4mm, thickness 0.254mm, Young's Modulus 69GPa, capacitance 125nF. Based on the theoretical analysis in Section 6.2, the attenuation constant of the beam metamaterial in short-circuit condition is shown in Figure 6.6.

The non-zero parts of attenuation constant represent that wave propagation and vibration will be attenuated at those frequencies. Higher amplitude means larger amount of attenuation. The bandgaps are due to the impedance mismatch caused by the adoption of piezoelectric transducer [173, 174]. The attenuation constant and vibration attenuation performances with different types of shunt circuit will be discussed in the following sections. Taking a cantilever beam with 20 unit cells, each unit cell with 8 elements as an example (m=20, n=8), based on Eq. (6.25), the vibration performance of the beam metamaterial is shown in Figure 6.7. We can clearly see bandgaps in the corresponding non-zero attenuation constant frequencies. For the other two smaller non-zero attenuation constants, the bandgaps are not obvious.

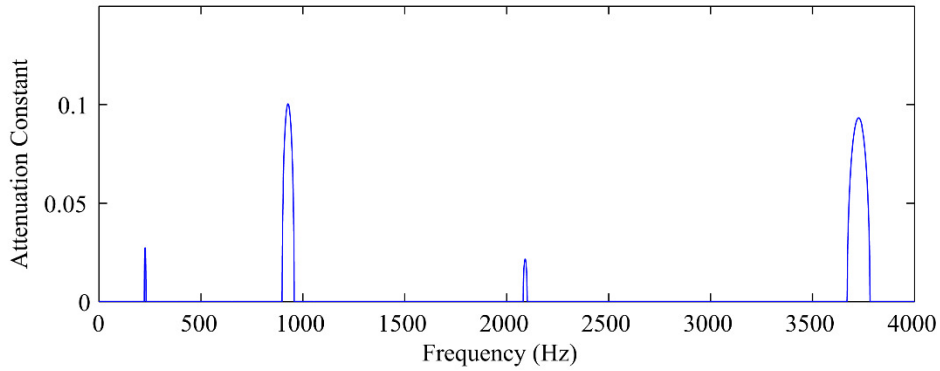

Figure 6.6 Attenuation constant of beam metamaterial in short-circuit condition

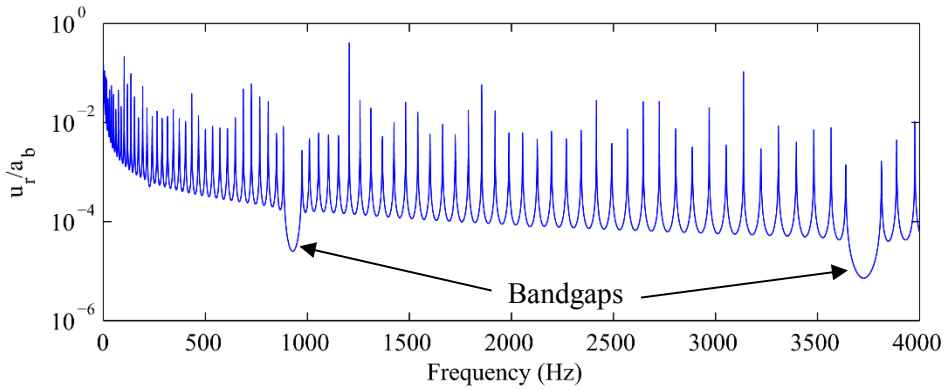

Figure 6.7 Cantilever beam metamaterial vibration in short-circuit condition

6.4.1 Simulation results of R-shunt and RL-shunt

Each piezoelectric film (QP16N) has capacitance of 125nF. Based on the following equation expressing the electrical resonant frequency,

$$\omega_n = \frac{1}{\sqrt{LC}} \tag{6.26}$$

we can obtain the inductance for a certain tuning frequency. Here we choose the tuning frequency to be 1500Hz. Based on Eq. (6.26) the inductance in RL-shunt is calculated to be 90.1mH. Note that if synthetic inductor comprised of op-amp and resistors, capacitors is used to realize large inductance [178, 185, 186], we can further reduce the tuning frequency. With damping ratio of 5%, the resistance in RL-shunt is 84.9Ω. As stated in [176], the resistance affects the amplitude and the frequency bandwidth of attenuation. Larger resistance reduces the maximum attenuation amplitude, but tends to broaden the bandwidth. For R-shunt, we choose resistance of 1kΩ as an example. The attenuation constant of the beam metamaterial with short-circuit, with R-shunt (R=1kΩ), and with RL-shunt (L=90.1mH, R=84.9Ω) are compared in Figure 6.8. We can see that RL-shunt has one more peak of attenuation constant at the tuning

frequency, which represents that the wave propagation and vibration will be attenuated around the desired tuning frequency.

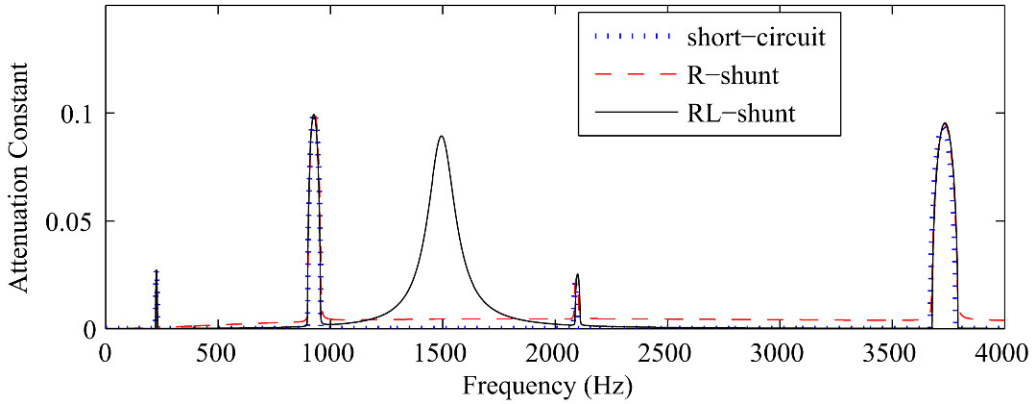

Figure 6.8 Attenuation constant when in short-circuit, with R-shunt (R=1kΩ), and with RL-shunt tuned for 1500Hz

Based on Eq. (6.25), we can get the corresponding vibration behaviors of the cantilever beam metamaterial, as shown in Figure 6.9. Note that no mechanical damping is considered here. We can see a bandgap at the tuning frequency by using the RL-shunt, while R-shunt just shows damping effect on the structure.

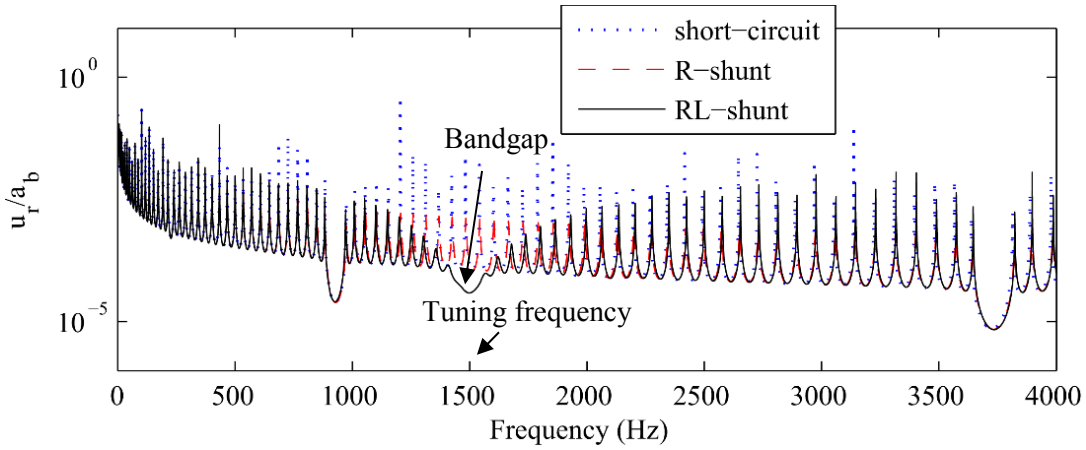

Figure 6.9 Beam vibrations with short-circuit, R-shunt (R=1kΩ), and RL-shunt tuned for 1500Hz

6.4.2 Simulation results of high-order resonant shunt circuit for broader band gaps

Based on the high-order resonant shunt circuit design in Section 6.3, we can design the high-order shunt as shown in Figure 6.5(b), with different damping ratios and inductance ratios, L_2/L_1, similar as "mass ratio" from mechanical point of view. Comparison of the proposed high-order shunt and the RL-shunt will be presented. The influence of inductance ratio and damping ratio on the vibration attenuation performance will also be explored in this section.

6.4.2.1 Comparison of high-order shunt and RL-shunt

Figure 6.10 shows the attenuation constant comparison of RL-shunt and high-order shunt, with the same attenuation constant peak amplitude at the tuning frequency. The parameters of the electrical components in the two types of shunts are: for RL-shunt, L=86.0mH, R=166Ω; for high-order shunt, L_1=90.1mH, R_1=0Ω, L_2=5.90mH, C_2=1.77μF, R_2=20.7Ω. With the definition of "bandwidth" as "the range of frequencies at $\frac{1}{\sqrt{2}}$ of the peak amplitude where the power drops to half of the maximum value, called "half power point"", the bandwidth of attenuation constant of RL-shunt is 196Hz, while the bandwidth of attenuation constant of high-order shunt is 337Hz which is 1.72 times wider than that of the RL-shunt. Thus, it is proved that the proposed high-order resonant shunt circuit can broaden the vibration attenuation bandwidth.

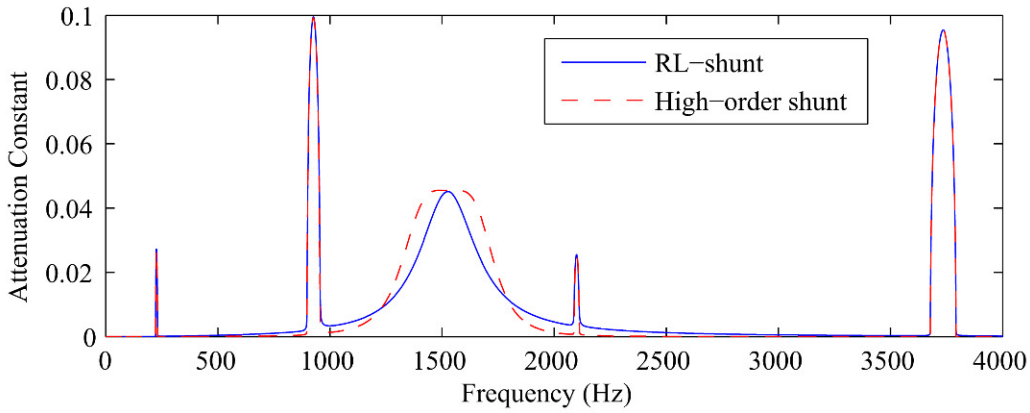

Figure 6.10 Attenuation constant with RL-shunt, and with high-order shunt

6.4.2.2 Influence of inductance ratio

Aiming at vibration attenuation around 1500Hz, the first-stage resonator and the second-stage resonator in the high-order shunt are designed to have the same tuning frequency of 1500Hz. In order to show the influence of inductance ratio, three different inductance ratios are chosen, 1%, 5%, and 10%. For all the inductance ratios, we choose the damping ratio in the first-stage resonator to be zero and the damping ratio in the second-stage resonator to be 5% (in order to compare with RL-shunt with damping ratio of 5%). The attenuation constants of high-order shunt with three different inductance ratios are compared in Figure 6.11.

For all the high-order shunts, $R_1 = 0\Omega$, $L_1 = 90.1\text{mH}$. For inductance ratio of 1%, $L_2 = L_1 \times 1\% = 901\mu\text{H}$, $C_2 = 12.5\mu\text{F}$, $R_2 = 0.849\Omega$. For inductance ratio of 5%, $L_2 = L_1 \times 5\% = 4.51\text{mH}$, $C_2 = 2.5\mu\text{F}$, $R_2 = 4.24\Omega$. For inductance ratio of 10%, $L_2 = L_1 \times 10\% = 9.01\text{mH}$, $C_2 = 1.25\mu\text{F}$, $R_2 = 8.49\Omega$. The result of RL-shunt with damping ratio of 5% (L=90.1mH,

R=84.9Ω) is also shown for comparison. From Figure 6.11 we can see that larger inductance ratio will generate more separate two peaks of attenuation constant, that is to say, with the same damping ratio, larger inductance ratio will result in more separation of two vibration bandgaps.

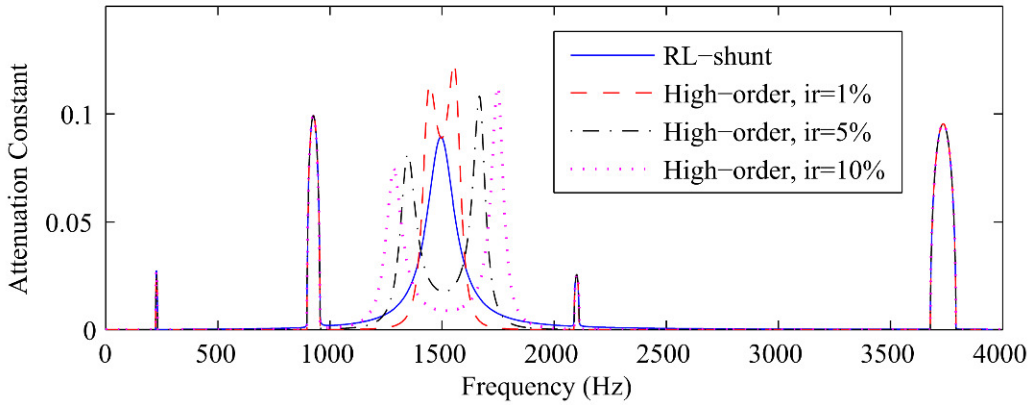

Figure 6.11 Attenuation constants of RL-shunt and high-order shunt with the same damping ratio of 5% but different inductance ratios (denoted as "ir") of 1% (dashed line), 5% (dash-dot line) and 10% (dotted line)

6.4.2.3 Influence of damping ratio

With the same inductance ratio of 5%, high-order resonant shunt circuit with no damping in the first-stage resonator and with three different damping ratios in the second-stage resonator, i.e., 1%, 5%, 10%, are compared in Figure 6.12.

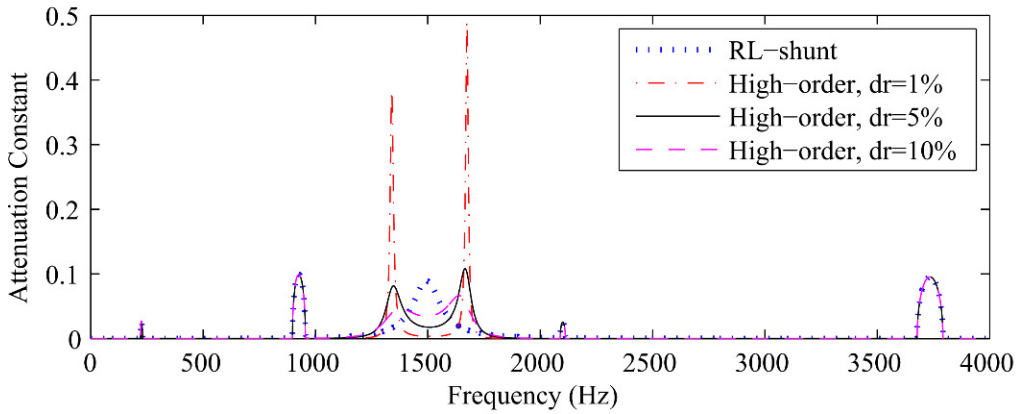

Figure 6.12 Attenuation constants of RL-shunt with damping ratio of 5% (dotted line) and high-order shunt with the same inductance ratio of 5% but different damping ratios (denoted as "dr") of 1% (dash-dot line), 5% (solid line), and 10% (dashed line)

For all the high-order shunts, $R_1 = 0\Omega$, $L_1 = 90.1\text{mH}$, $L_2 = L_1 \times 5\% = 4.51\text{mH}$, $C_2 = 2.50\mu\text{F}$. For damping ratio of 1%, $R_2 = 0.848\Omega$. For damping ratio of 5%, $R_2 = 4.24\Omega$. For damping ratio of 10%, $R_2 = 8.48\Omega$. From Figure 6.12 we can see that smaller damping ratio

results in two sharper peaks of attenuation constant but with narrower attenuation bandwidth, and the two peaks are more separate. It is concluded that with larger inductance ratio and smaller damping ratio, the proposed high-order shunt can generate more separate two bandgaps.

6.5 Design of Two Separate Bandgaps

By studying the influence of inductance ratio and damping ratio on vibration control performance in Section 6.4.2, we found that the proposed high-order resonant shunt circuit can generate two separate bandgaps around the tuning frequency. It is concluded in section 6.4.2.3 that larger inductance ratio and smaller damping ratio will result in more separation of the two bandgaps.

For practical application, if the bandgaps are desired at two specific frequencies, the way to determine electrical component parameters is very crucial. The beam metamaterial with periodic piezoelectric arrays with shunt circuits is a mechanical-electrical coupling structure. It is hard to predict the exact location of bandgaps. However, we can predict the approximate bandgap locations using impedance analysis of the circuit part by ignoring the coupling with the beam. This approximation shall be good enough to guide the practical design, since the influence from beam dynamics to the circuit resonances is small when the thickness of piezoelectric patches is much smaller than the beam itself.

6.5.1 Approximate prediction of bandgap location using impedance of resonant circuit

The circuit models of piezoelectric transducer with RL-shunt and high-order shunt are shown in Figure 6.13(a) and (b), respectively. The piezoelectric transducer can be modelled as a capacitor in parallel with a dependent current source, I_{p}.

Taking the parameters in Figure 6.11 as an example, the impedances of piezoelectric capacitor with RL-shunt and high-order shunts are compared in Figure 6.14. Due to the mechanical-electrical coupling between shunt circuit and beam structure, there are less than 1% frequency errors between the peaks of impedance curve and the peaks of vibration attenuation curve. Therefore, we can predict the approximate locations of bandgaps by analyzing the impedance of resonant circuit.

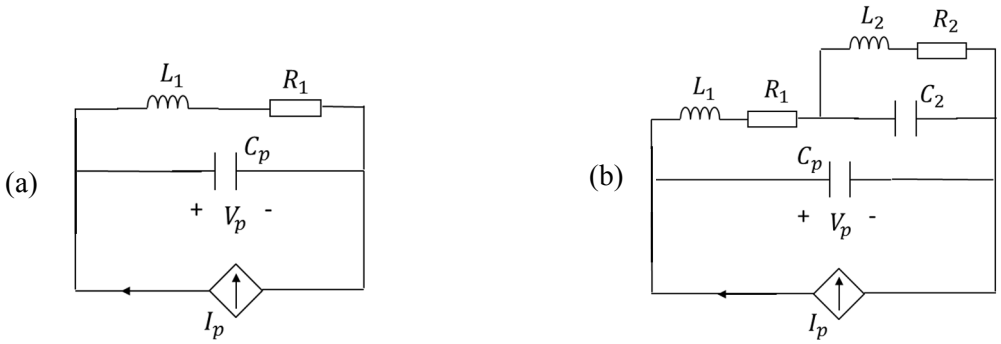

Figure 6.13 Electrical models of piezoelectric transducer with (a) RL-shunt and (b) high-order shunt

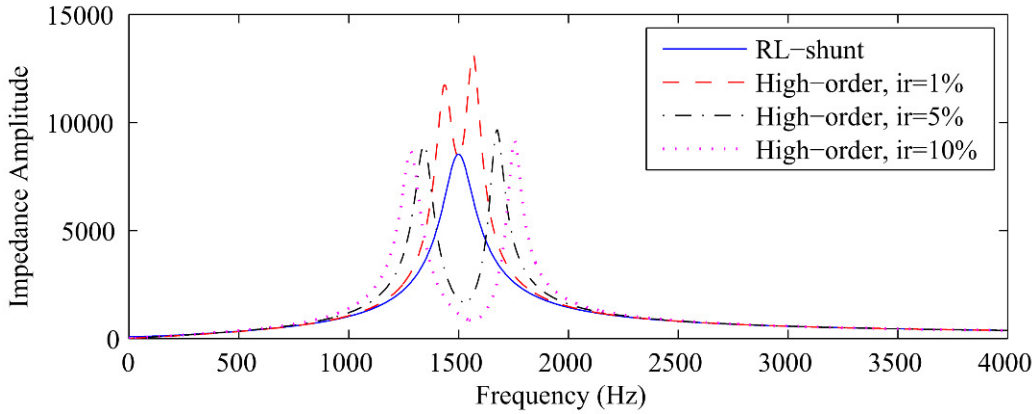

Figure 6.14 Impedance of piezoelectric transducer with shunt circuit (with the same parameters as in Figure 6.11)

6.5.2 Parameter determination of electrical components in the proposed high-order shunt

The impedance of piezoelectric transducer with high-order shunt is

$$Z = \frac{Num(s)}{Den(s)} \tag{6.27}$$

where

$$Num(s) = L_1L_2C_2s^3 + (R_1L_2C_2 + R_2L_1C_2)s^2 + (L_1 + L_2 + R_1R_2C_2)s + R_1 + R_2 \tag{6.27a}$$

$$Den(s) = L_1L_2C_2C_ps^4 + (R_1L_2C_2 + R_2L_1C_2)C_ps^3 + \left[(L_1 + L_2 + R_1R_2C_2)C_p + L_2C_2\right]s^2 + \left(R_1C_p + R_2C_p + R_2C_2\right)s + 1 \tag{6.27b}$$

The two resonant frequencies of the high-order shunt are solutions of the following equation.

$$L_1L_2C_2C_p\omega^4 - \left(L_1C_p + L_2C_p + R_1R_2C_2C_p + L_2C_2\right)\omega^2 + 1 = 0 \tag{6.28}$$

Thus, from Eq. (6.28), for two specific bandgap frequencies, denoted as f_1 and f_2 (the corresponding angular frequencies are ω_1 and ω_2), the electrical components need to satisfy the following two equations.

$$L_1C_p + L_2C_p + R_1R_2C_2C_p + L_2C_2 = \frac{1}{\omega_1^2} + \frac{1}{\omega_2^2} \tag{6.29}$$

$$L_1L_2C_2C_p = \frac{1}{\omega_1^2\omega_2^2} \tag{6.30}$$

For convenience, the two LC-branches are chosen to have the same resonant frequency, ω_n, from Eq. (6.30) we know

$$L_1C_p = L_2C_2 = \frac{1}{\omega_n^2} \tag{6.31}$$

Since the damping ratios ζ_1 and ζ_2 in the two stages resonators are usually small,

$$R_1R_2C_2C_p = 4\zeta_1\zeta_2\sqrt{L_1C_pL_2C_2} = \frac{4\zeta_1\zeta_2}{\omega_n^2} \ll \frac{1}{\omega_n^2} = L_1C_p \tag{6.32}$$

the term $R_1R_2C_2C_p$ in Eq. (6.29) can be neglected when calculate the parameter L_1 and L_2. Denoting the inductance ratio as γ, combining Eqs. (6.29)~(6.31), we can get

$$\gamma = \frac{\omega_2}{\omega_1} + \frac{\omega_1}{\omega_2} - 2 \tag{6.33}$$

Thus, the electrical parameters in the high-order shunt can be chosen for the desired bandgaps ω_1 and ω_2

$$L_1 = \frac{1}{\omega_1\omega_2C_p},\ L_2 = \gamma L_1 = (\frac{\omega_2}{\omega_1} + \frac{\omega_1}{\omega_2} - 2)L_1,\ C_2 = \frac{C_p}{\gamma} = \frac{C_p}{\frac{\omega_2}{\omega_1}+\frac{\omega_1}{\omega_2}-2},\ R_1 = 2\zeta_1\sqrt{\frac{L_1}{C_p}},\ R_2 = 2\zeta_2\sqrt{\frac{L_2}{C_2}} \tag{6.34}$$

The damping ratios can be selected based on the requirements of vibration attenuation amplitude and bandwidth.

6.5.3 Simulation result of two separate bandgaps

In order to verify the effectiveness of the parameter determination method described in Section 5.2, we arbitrarily chose two desired vibration attenuation frequencies, 1500Hz and 2500Hz. Based on Eq. (6.34), the inductance ratio is solved to be 26.7%, $L_1 = 54.0\text{mH}$, $L_2 = 14.4\text{mH}$, $C_2 = 469n\text{F}$. For the requirement of equal vibration attenuation at the two desired frequencies, we chose the two damping ratios to be $\zeta_1 = 4.5\%$, $\zeta_2 = 2\%$. The attenuation constant curve of high-order shunt is shown in Figure 6.15.

From the figure we can see that the high-order shunt with the designed electrical parameters generates two separate attenuation peaks at 1496Hz and 2497Hz, which are very close to the two desired frequencies. Based on Eq. (6.25), the corresponding beam vibration behaviors are illustrated in Figure 6.16. From the figure we can clearly see the high-order

resonant shunt circuit with the designed parameters significantly reduces beam vibration at the frequency ranges around the two desired frequencies, 1500Hz and 2500Hz. It generates two separate bandgaps around the two desired frequencies. It can be concluded that with well-designed inductance ratio and damping ratio we can achieve vibration and wave propagation attenuation at two desired frequencies by using the proposed high-order resonant shunt circuit.

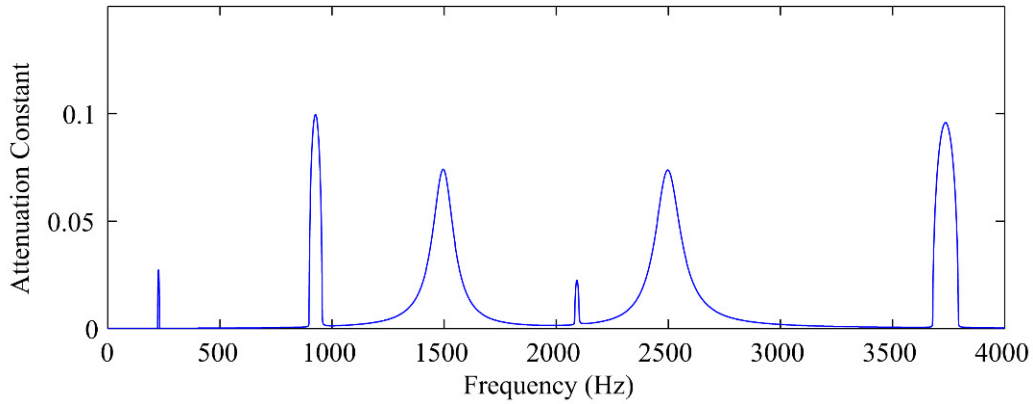

Figure 6.15 Attenuation constant of high-order shunt with the designed electrical parameters

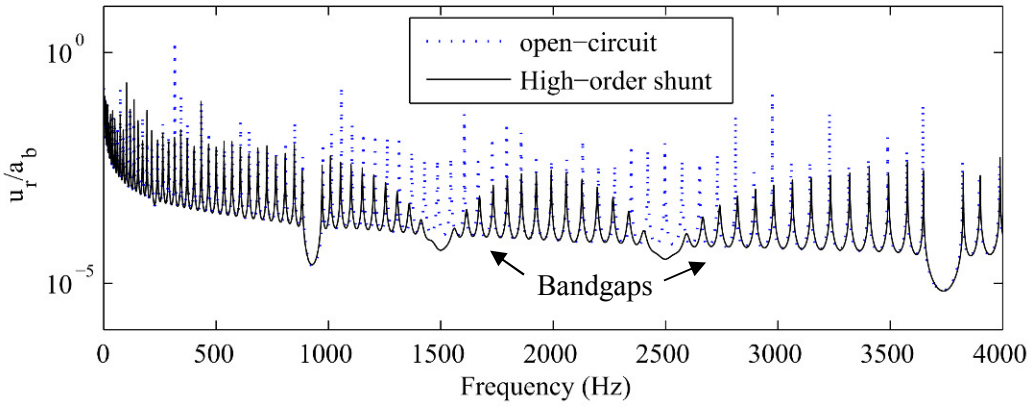

Figure 6.16 Beam vibration behavior with open-circuit, and high-order shunt with designed electrical parameters

The essential reason for vibration attenuation by using piezoelectric shunt circuit is that mechanical energy has been extracted and converted to electrical energy, which is stored in the external shunt circuit. The energy distribution in the two stages of high-order shunt in Figure 6.13(b) can be represented by i_1/I_p and i_2/I_p, where i_1 and i_2 are the current passing through inductor L_1 and L_2, respectively. The energy distribution for the high-order shunt with the designed electrical parameters is shown in Figure 6.17. We can see that the extracted mechanical energy is stored in both the two stages of resonators, a little more in the second-stage than in the

first-stage. Since the high-order shunt contains series resonances, the extracted energy is stored in both the two resonances, which is different from RL-shunt with single resonance.

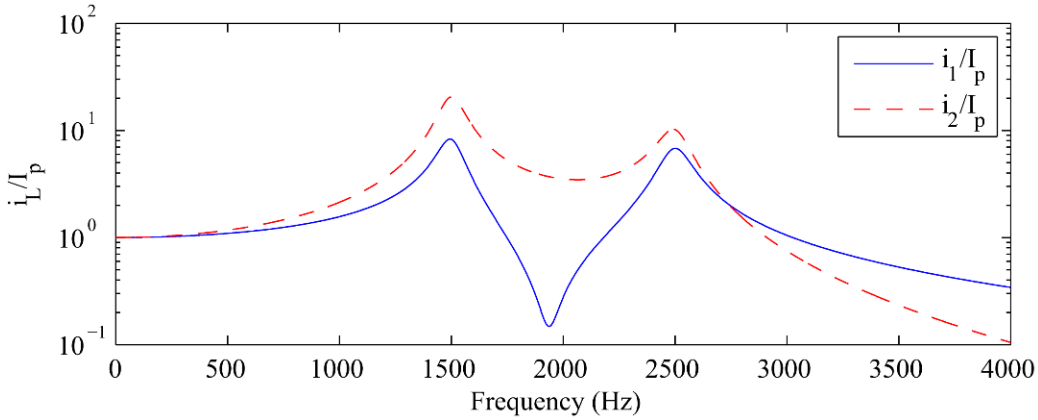

Figure 6.17 Energy distribution in the two stages of resonators in the high-order shunt

6.6 CONCLUSION

An innovative high-order resonant shunt circuit for the vibration and wave propagation attenuation of beam metamaterial with periodic piezoelectric arrays is proposed in this paper. Finite element modeling of the metamaterial is established, based on which the attenuation constant that represents the wave propagation and vibration attenuation performance has been obtained. Simulation results illustrate the attenuation performances of beam metamaterial with different types of piezoelectric shunt, i.e., R-shunt, RL-shunt, and the proposed high-order resonant circuit shunt. It is concluded that the proposed high-order shunt can generate broader vibration attenuation bandwidth without sacrificing the attenuation amplitude than the RL-shunt, and it can generate two separate bandgaps, while R-shunt just acts as adding damping to the beam structure. The influence of inductance ratio and damping ratio in high-order shunt on the attenuation performances is also studied. It is found that larger inductance ratio and smaller damping ratio will result in more separated bandgaps. An impedance-based parameter determination method is presented for the circuit parameter design in the proposed high-order shunt, in order to realize two bandgaps at two desired frequencies. The simulation results verify the effectiveness of this method.

Chapter 7 Conclusion

Piezoelectric-based multifunctional smart structures for energy harvesting, structure health monitoring, and vibration control are studied in this dissertation. Innovative ideas have been proposed and developed in all the three aspects, i.e., energy harvesting, structure health monitoring, and vibration control. The projects involve multidisciplinary knowledge in mechanical engineering and electrical engineering, including structural dynamics, vibration & control, mechatronics, circuit design, etc.

In the energy harvesting aspect, an efficient double-beam energy harvester with beam-type tuned mass damper has been designed and investigated, which has two primary advantages: vibration damping in multi-modes, and energy harvesting in broader bandwidth. An innovative beam-type tuned mass damper was proposed, which can virtually dissipate mechanical vibration in all the vibration modes. In the other hand, a type of 33-mode multilayer piezoelectric stack with force amplification frame is created and investigated. The energy generation density is much higher than the state-of-the-art.

In the structure health monitoring aspect, a sensitivity-enhanced admittance-based structure health monitoring method with high-order resonant circuit, which is equivalent to adding series tuned mass damper, has been proposed, with effects of increased signal-to-noise ratio and improved damage detection sensitivity. The technology of model conversion between mechanical model and electrical model based on electrical-mechanical analogy has been explored, which provides a tutorial guide for the external circuit design for piezoelectric transducer attached on mechanical host structure.

In the vibration control aspect, a self-powered vibration control system with switch pre-charged inductor circuit is developed, which can minimize mechanical vibration based on H_2 control algorithm, and meanwhile harvest energy from the mechanical vibration to provide power supply for the control unit. A type of switch pre-charged inductor circuit based on LC resonant circuit was proposed to implement desired piezoelectric voltage. The integration of H_2 control minimization algorithm and LC resonant circuit based implementation method is a non-conventional technology, which has been verified to be a promising way of building a self-powered system. In addition, vibration and wave propagation attenuation with periodic piezoelectric arrays for metamaterial has been studied, and a high-order resonant shunt circuit has been proven to reduce mechanical vibration in a broader frequency range and have the ability

of generating two separate bandgaps simultaneously. The high-order resonant circuit equivalent to adding series mechanical resonators to the unit cell of metamaterial was proposed and investigated, which was verified to possess better wave propagation attenuation performance.

The merits of this dissertation include: (1) The proposed innovative technologies in each of the three aspects will improve the development of the three aspects. It also bridges different areas and created new knowledge in these areas, especially in mechanical engineering and electrical engineering. It improves the interdisciplinary development, since it involves structural dynamics, vibration & control, mechatronics, circuit design, etc. (2) The proposed ideas in this dissertation can be applied for any beam type structures, typical applications for wind turbine blade and helicopter blade. The introduction of tuned mass damper design into the multifunctional smart structure provides a revolutionary way to reduce more mechanical vibration and meanwhile harvest more electrical energy. The conversion between the mechanical mass-spring-damper structure and the electrical inductor-capacitor-resistor circuit based on mechanical-electrical analogy provides a tutorial guide for the external circuit design for piezoelectric transducer adhered on mechanical host structure. (3) The technology of multifunctional smart structure with functions of energy harvesting, structure health monitoring, and vibration control has broad application, such as wind turbine blades, helicopter blades, aircraft wings, and other beam-like mechanical structures. Taking wind turbine blade as an example, using the multifunctional smart structure can reduce the unexpected flap bending vibration and meanwhile monitor the blade's health so that in-time action can be taken to prevent serious blade damage. The maintenance and repair costs can be significantly reduced. In addition, the multifunctional smart structure can convert the reduced mechanical energy into electrical energy, which can be used as power supply for the health monitoring sensors, vibration control sensors and actuators, so that the whole structure is a self-powered system with no need of external power supply.

Reference

[1] I. Ahmad, 1988, "Smart Structures and Materials", *Proceedings of U.S. Army Research Office Workshop on Smart Materials, Structures and Mathematical Issues*, edited by C. A. Rogers, September 15-16, Virginia Polytechnic Institute & State University, Technomic Publishing Co., Inc, pp. 13-16.

[2] R. F. Gibson, 2010, "A Review of Recent Research on Mechanics of Multifunctional Composite Materials and Structures", *Composite Structures*, **92**, pp. 2793-2810.

[3] World Wind Energy Association, www.wwindea.org/.

[4] F. Ashley, R. J. Cipriano, S. Breckenridge, G. A. Briggs, L. E. Gross, J. Hinkson, and P. A. Lewis, 2007, "Bethany Wind Turbine Study Committee Report", www.townofbethany.com.

[5] X. Shen, X. Zhu, and Z. Du, 2011, "Wind turbine aerodynamics and loads control in wind shear flow", *Energy*, **36**, pp. 1424-1434.

[6] J. Wang, D. Qin, and T. C. Lim, 2010, "Dynamic analysis of horizontal axis wind turbine by thin-walled beam theory", *Journal of Sound and Vibration*, **329**, pp. 3565-3586.

[7] M. L. Flemming, and S. Troels, 2003, "New lightning qualification test procedure for large wind turbine blades", Int. Conf. Lightning and Static Electricity, Blackpool, UK, pp. 36.1-10.

[8] E. Rosenbloom, 2006, "A Problem with Wind Power", www.aweo.org.

[9] M. J. Sundaresan, M. J. Schulz, and A. Ghoshal, 2002, "Structural health monitoring static test of a wind turbine blade", *Subcontract Report NREL/SR-500-28719*, National Renewable Energy Laboratory, CO, USA.

[10] H. Sutherland, A. Beattie, B. Hansche, W. Musial, J. Allread, J. Johnson, and M. Summers, 1994, "The application of non-destructive techniques to the testing of a wind turbine blade", *Sandia Report SAND93-1380*, Sandia National Laboratories, USA.

[11] P. A. Joosse, M. J. Blanch, A. G. Dutton, D. A. Kouroussis, T. P. Philippidis, and P. S. Vionis, 2002, "Acoustic emission monitoring of small wind turbine blades", *Proc. 21st ASME Wind Energy Symp. In conjunction with 40th AIAA Aerospace Sciences Meeting*, Reno, USA, pp. 1-11, AIAA-2002-0063.

[12] N. P. Avdelidis, D. P. Almond, C. Ibarra-Castanedo, A. Bendada, S. Kenny, and X. Maldague, 2006, "Structural integrity assessment of materials by thermography", Conf. Damage in Composite Materials, CDCM 2006, Stuttgart, Germany.

[13] D. Tuzzeo, and F. Lanza di Scalea, 2001, "Noncontact air-coupled guided wave ultrasonics for detection of thinning defects in aluminum plates", *Res. Nondestr. Eval.*, **13**, pp. 61-78.

[14] S. S. Kessler, S. M. Spearing, M. J. Atalla, C. E. S. Cesnik, and C. Soutis, 2002, "Damage detection in composite materials using frequency response methods", *Composites B*, **33**, pp. 87-95.

[15] H. Zhang, M. J. Schulz, F. Ferguson, and P. F. Pai, 1999, "Structural health monitoring using transmittance functions", *Mech. Syst. Signal Process*, **13**, pp. 765-787.

[16] C. R. Farrar, and S. W. Doebling, 1997, "An overview of modal-based damage identification methods", DAMAS 97, Sheffield, UK.

[17] S. W. Doebling, C. R. Farrar, and M. B. Prime, 1998, "A summary review of vibration-based damage identification methods", *Shock Vib. Dig.*, **30**, pp. 91-105.

[18] N. Takeda, 2002, "Characterization of microscopic damage in composite laminates and real-time monitoring by embedded optical fiber sensors", *Int. J. Fatigue*, **24**, pp. 281-289.

[19] P. Veers, G. Bir, and D. Lobitz, 1998, "Aeroelastic Tailoring in Wind-Turbine Blade Applications", *Windpower '98, American Wind Energy Association Meeting and Exhibitioin, Bakerfield*, California, April 28-May 1.
[20] V. Maldonado, M. Boucher, R. Ostman, and M. Amitay, 2009, "Active Vibration Control of a Wind Turbine Blade using Synthetic Jets", *Int. J. of Flow Control*, **1**(4), pp. 227-238.
[21] N. M. Karaolis, P. J. Mussgrove, and G. Jeronimidis, 1988, "Active and Passive Aeroelastic Power Control using Asymmetric Fibre Reinforced Laminates for Wind Turbine Blades", *Proc. 10th British Wind Energy Conf.*, D. J. Milbrow Ed., London, March 22-24.
[22] H. J. T. Kooijman, 1996, "Bending-Torsion Coupling of a Wind Turbine Rotor Blade", ECN report I-96-060, Peten, Dec. 1996.
[23] O. Dossing, 1997, "Vibration Control on Huge Wind Turbine Blades using Tuned Absorbers", *Proceeding of the SPIE*, **3089**(1), pp. 216-222.
[24] J. H. Laks, L. Y. Pao, and A. Wright, 2009, "Combined feedforward/feedback control of wind turbines to reduce blade flap bending moments", *Proc. AIAA/ASME Wind Energy Symp*.
[25] O. O. Ozgumus, and M. O. Kaya, 2007, "Formulation for flutter and vibration analysis of a hingeless helicopter blade in hover: Part I", *Aircraft Engineering and Aerospace Technology*, **79**(2), pp. 177-183.
[26] J. S. Park, S. N. Jung, Y. H. You, S. H. Park, and Y. H. Yu, 2011, "Validation of comprehensive dynamics analysis predictions for a rotor in descending flight", *Aircraft Engineering and Aerospace Technology*, **83**(2), pp. 75-84.
[27] MicroStrain company, http://www.microstrain.com/.
[28] Basic Principles – Piezoelectric Effect, a course of BME240 from University of California – Irvine, http://bme240.eng.uci.edu/students/06s/yuhsianh/Piezoelctric%20effect.htm
[29] S. R. Anton, and H. A. Sodano, 2007, "A Review of Power Harvesting using Piezoelectric Materials (2003-2006)", *Smart Mater. Struct.*, **16**, pp. R1-R12.
[30] B. Jaffe, R. Cook, and H. Jaffe, "Piezoelectric Ceramics", 1971, New York: Academic Press.
[31] N. W. Hagood, and A. Von Flotow, 1991, "Damping of Structural Vibrations with Piezoelectric Materials and Passive Electrical Networks", *Journal of Sound and Vibration*, **146**(2), pp. 243-268.
[32] Sodano, H. A., Inman, D. J., and Park, G., 2004, "A Review of Power Harvesting from Vibration using Piezoelectric Materials", *The Shock and Vibration Digest*, **36**(3), pp. 197-205.
[33] S. Roundy, E. S. Leland, J. Baker, E. Carleton, E. Reilly, E. Lai, B. Otis, J. M. Rabaey, P. K. Wright, and V. Sundararajan, 2005, "Improving Power Output for Vibration-based Energy Scavengers", *Pervasive Computing, IEEE*, **4**(1), pp. 28-36.
[34] J. Kymissis, C. Kendall, J. Paradiso, and N. Gershenfeld, 1998, "Parasitic Power Harvesting in Shoes", *Proc., 2nd IEEE Int. Symp. on Wearable Computers*, Pittsburgh, pp. 132-139.
[35] S. W. Arms, C. P. Townsend, D. L. Churchill, J. H. Galbreath, and S. W. Mundell, 2005, "Power management for energy harvesting wireless sensors", *Proc. Smart Structures and Materials Conf.*.

[36] C. Eichhorn, F. Goldschmidtboeing, and P. Woias, 2008, "A Frequency Tunable Piezoelectric Energy Converter based on a Cantilever Beam", *Proceedings of PowerMEMS 2008+ microEMS 2008*, Sendai, Japan, Nov. 9-12.

[37] V. R. Challa, M. G. Prasad, Y. Shi, and F. T. Fisher, 2008, "A Vibration Energy Harvesting Device with Bidirectional Resonance Frequency Tunability", *Smart Mater. Struct*., **17**, 015035.

[38] I. Kozinsky, 2009, "Study of Passive Self-Tuning Resonator for Broadband Power Harvesting", *PowerMEMS 2009*, Washington DC, Dec. 1-4.

[39] P. D. Mitcheson, T. C. Green, E. M. Yeatman, and H. S. Holmes, 2004, "Architectures for Vibration-driven Micro Power Generators", *J. Microelectromechanical Systems*, **13**(3), pp. 429-440.

[40] N. A. Kong, D. S. Ha, A. Etrurk, and D. J. Inman, 2010, "Resistive Impedance Matching Circuit for Piezoelectric Energy Harvesting", *J. Intelligent Material Systems and Structures*, **21**, pp. 1293-1302.

[41] J. Liang, and W. H. Liao, 2010, "Impedance Matching for Improving Piezoelectric Energy Harvesting Systems", *Proceedings of Active and Passive Smart Structures and Intelligent Systems*, **7643**, San Diego, CA.

[42] W. J. Wu, Y. Y. Chen, B. S. Lee, J. J. He, and Y. T. Pen, 2006, "Tunable Resonant Frequency Power Harvesting Devices", *Proceedings of Smart Structures and Materials: Damping and Isolation*, **6169**, San Diego, CA.

[43] A. Badel, D. Guyomar, E. Lefeuvre, and C. Richard, 2006, "Piezoelectric Energy Harvesting using a Synchronized Switch Technique", *J. Intelligent Material Systems and Structures,* **17**, pp. 831-839.

[44] I. Sari, T. Balkan, and H. Kulah, 2008, "An Electromagnetic Micro Power Generator for Wideband Environmental Vibrations", *Sensors and Actuators A*, **145-146,** pp. 405-413.

[45] M. Ferrari, V. Ferrari, M. Guizzetti, D. Marioli, and A. Taroni, 2008, "Piezoelectric Multifrequency Energy Converter for Power Harvesting in Autonomous Microsystems", *Sensors and Actuators A*, **142**, pp. 329-335.

[46] S. Qi, R. Shuttleworth, O. S. Olutunde, and J. Wright, 2010, "Design of a multiresonant beam for broadband piezoelectric energy harvesting", *Smart Materials and Structures*, **19.**

[47] H. Xue, Y. Hu, and Q. M. Wang, 2008, "Broadband Piezoelectric Energy Harvesting Devices Using Multiple Bimorphs with Different Operating Frequencies", *IEEE Transactions on Ultrasonics, Ferroelectrics, and Frequency Control*, **55**, pp. 2014-2018.

[48] S. Roundy, and Y. Zhang, 2005, "Toward Self-tuning Adaptive Vibration-Based Micro-Generators", *Proc. Smart Structures, Devices, and Systems II,* pp. 373-384.

[49] E. S. Leland, and P. K. Wright, 2006, "Resonance Tuning of Piezoelectric Vibration Energy Scavenging Generators using Compressive Axial Preload", *Smart Materials and Structures,* **15-14**, pp. 13-20.

[50] C. Eichhorn, F. Goldschmidtboeing, and P. Woias, 2009, "Bidirectional frequency tuning of a piezoelectric energy converter based on a cantilever beam", *J. Micromechanics and Micro engineering*, **19**.

[51] J. W. Xu, W. W. Shao, F. R. Kong, and Z. H. Feng, 2010, "Right- Angle Piezoelectric Cantilever with Improved Energy Harvesting Efficiency", *Applied Physics Letters*, **96**.

[52] B. Yang, C. Lee, W. Xiang, J. Xie, J. H. He, R. K. Kotlanka, S. P. Low, and H. Feng, 2009, "Electromagnetic Energy Harvesting from Vibrations of Multiple Frequencies", *J. Micromechanics and Micro engineering*, **19**.

[53] S. Lee, B. D. Youn, and B. C. Jung, 2009, "Robust Segment-Type Energy Harvester and its Application to a Wireless sensor", *Smart Materials and Structures*, **18**.
[54] Z. Yang, and J. Yang, 2009, "Connected Vibrating Piezoelectric Bimorph Beams as a Wide-Band Piezoelectric Power Harvester", *J. Intelligent Material Systems and Structures*, **20** pp. 569-574.
[55] A. Raghavan, and E. S. Cesnik, 2007, "Review of Guided-Wave Structural Health Monitoring", *The Shock and Vibration Digest*, **39**(2), pp. 91-114.
[56] D. Osmont, D. Devillers, and F. Taillade, 2001, "Health Monitoring of Sandwich Plates based on the Analysis of the Interaction of Lamb Waves with Damages", *Proceedings of the SPIE*, **4327**, pp. 290-301.
[57] S. Kessler, and M. Spearing, 2002, "Design of a Piezoelectric-based Structure Health Monitoring System for Damage Detection in Composite Materials", *Proceedings of the SPIE*, **4701**, pp. 86-96.
[58] P. Wilcox, M. Lowe, and P. Cawley, 1999, "Lamb and SH Wave Transducer Arrays for the Inspection of Large Areas of Thick Plates", *Proceedings of the Review of Progress in Quantitative Nondestructive Evaluation*, Melville, NY, pp. 1049-1056.
[59] G. Park, H. Sohn, and C. R. Farrar, 2003, "Overview of Piezoelectric Impedance-based Health Monitoring and Path Forward", *The Shock and Vibration Digest*, **35**(6), pp. 451-463.
[60] C. Liang, F. P. Sun, and C. A. Rogers, 1994, "Coupled Electromechanical Analysis of Adaptive Material Systems-Determination of the Actuator Power Consumption and System Energy Transfer", *Journal of Intelligent Material Systems and Structures*, **5**, pp. 12-20.
[61] J. W. Ayres, F. Lalande, Z. Chaudhry, and C. A. Rogers, 1998, "Qualitatie Impedance-Based Health Monitoring of Civil Infrastructures", *Smart Materials and Structures*, **7**, pp. 599-605.
[62] F. P. Sun, Z. Chaudhry, C. Liang, and C. A. Rogers, 1995, "Truss Structure Integrity Identification Using PZT Sensor-Actuator", *Journal of Intelligent Material Systems and Structures*, **6**, pp. 134-139.
[63] M. Abe, G. Park, and D. J. Inman, 2000, "Impedance-Based Monitoring of Stress in Thin Structure Members", *Proceedings of the 11th International Conference on Adaptive Structure and Technologies*, pp. 285-292, Nagoya, Japan.
[64] A. N. Zagrai, and V. Giurgiutiu, 2001, "Electromechanical Impedance Method for Crack Detection in Thin Plates", *Journal of Intelligent Material Systems and Structures*, **12**, pp. 709-718.
[65] S. Bhalla, A. S. K. Naidu, C. W. Ong, and C. K. Soh, 2002, "Practical Issues in the Implementation of Electromechanical Impedance Technique for NDE", *Proceedings of the SPIE International Symposium on Smart Materials, Nano-, and Micro-Smart Systems*, pp. 4935-4977, Melbourne, Australia.
[66] Z. A. Chaudhry, T. Joseph, F. P. Sun, and C. A. Rogers, 1995, "Local-Area Health Monitoring of Aircraft via Piezoelectric Actuator/Sensor Patches", *Proc. SPIE on Smart Structures and Materials*, pp. 2443-268, San Diego, CA.
[67] X. Wang, and J. Tang, 2009, "Damage Identification using Piezoelectric Impedance Approach and Spectral Element Method", *Journal of Intelligent Material Systems and Structures*, **20**(8), pp. 907-921.

[68] G. Park, H. Sohn, C. R. Farrar, and D. J. Inman, 2003, "Overview of Piezoelectric Impedance-Based Health Monitoring and Path Forward", *Shock and Vibration Digest*, **35**(6), pp. 451-463.

[69] S. Bhalla, A. Gupta, S. Bansal, and T. Garg, 2009, "Ultra Low-Cost Adaptations of Electro-mechanical Impedance Technique for Structural Health Monitoring", *Journal of Intelligent Material Systems and Structures*, **20**(8), pp. 991-999.

[70] D. M. Peairs, G. Park, and D. J. Inman, 2004, "Improving Accessibility of the Impedance-Based Structural Health Monitoring Method", *Journal of Intelligent Material Systems and Structures*, **15**(2), pp. 129-139.

[71] X. Wang and J. Tang, 2010, "Damage Detection using Piezoelectric Admittance Approach with Inductive Circuitry", *Journal of Intelligent Material Systems and Structures*, **21**(7), pp. 667-676.

[72] X. Wang, and J. Tang, 2010, "An Enhanced Piezoelectric Impedance Approach for Damage Detection with Circuitry Integration", *Smart Materials and Structures*, **19**(4), 045001.

[73] C. R. Farrar, W. E. Baker, T. M. Bell, K. M. Cone, T. W. Darling, T. A. Duffey, A. Eklund, and A. Migliori, 1994, "Dynamic Characterization and Damage Detection in the I-40 Bridge over the Rio Grande", *Los Alamos National Laboratory report*, LA-12767-MS.

[74] C. R. Farrar, S. W. Doebling, P. J. Cornwell, and E. G. Straser, 1997, "Variability of Modal Parameters Measured on the Alamosa Canyon Bridge", *Proc. 15th International Modal Analysis Conf.*, Orlando, FL, pp. 257-263.

[75] S. W. Doebling, C. R. Farrar, and R. S. Goodman, 1997, "Effects of Measurement Statistics on the Detection of Damage in the Alamosa Canyon Bridge", *Proceedings 15th International Modal Analysis Conf.*, Orlando, FL, pp. 919-929.

[76] A. Migliori, T. M. Bell, R. D. Dixon, and R. Strong, 1993, "Resonant Ultrasound Non-Destructive Inspection", *Los Alamos National Laboratory report*, LA-UR-93-225.

[77] W. M. West, 1984, "Illustration of the use of Modal Assurance Criterion to Detect Structural Changes in an Orbiter Test Specimen", *Proc. Air Force Conf. on Aircraft Structural Integrity*, pp. 1-6.

[78] C. P. Ratcliffe, 1997, "Damage Detection using a Modified Laplacian Operator on Mode Shape Data", *Journal of Sound and Vibration*, **204**(3), pp. 505-517.

[79] P. S. Skjaeraek, S. R. K. Nielsen, and A. S. Cakmak, 1996, "Identification of Damage in Reinforced-Concrete Structures from Earthquake Records: Optimal Location of Sensors", *Soil Dynamics and Earthquake Engineering*, **15**(6), pp. 347-358.

[80] A. K. Pandey, M. Biswas, and M. M. Samman, 1991, "Damage Detection from Changes in Curvature Mode Shape", *Journal of Sound and Vibration*, **145**(2), pp. 321-332.

[81] K. G. Topole, and N. Stubbs, 1995, "Nondestructive Damage Evaluation of a Structure from Limited Modal Parameters", *Earthquake Engineering and Structural Dynamics*, **24**(11), pp. 1427-1436.

[82] S. P. Beeby, M. J. Tudor, and N. M. White, 2006, "Energy Harvesting Vibration Sources for Microsystems Applications", *Meas. Sci. Technol.*, **17**, pp. 175-195.

[83] S. W. Arms, C. P. Townsend, D. L. Churchill, J. H. Galbreath, and S. W. Mundell, 2005, "Power Management for Energy Harvesting Wireless Sensors", *Proc. Smart Structures and Materials, Proc. SPIE 5763*, pp. 267-275.

[84] H. A. Sodano, D. J. Inman, and G. Park, 2004, "A Review of Power Harvesting from Vibration using Piezoelectric Materials", *The Shock and Vibration Digest*, **36**(3), pp. 197-205.
[85] M. A. Galhardi, T. H. Guilherme, and V. L. Junior, 2008, "A Review of Power Harvesting on Mechanical Vibration using Piezoelectric Materials and Applications", *7th Brazilian Conference on Dynamics, Control and Applications*, May 7-9, FCT-Unesp at Presidente Prudente, SP, Brazil.
[86] J. Feenstra, J. Granstrom, and H. Sodano, 2008, "Energy Harvesting through a Backpack Employing a Mechanically Amplified Piezoelectric Stack", Mechanical Systems and Signal Processing, **22**(3), pp. 721-734.
[87] C. A. Howells, 2009, "Piezoelectric Energy Harvesting", *Energy Conversion and Management*, **50**(7), pp. 1847-1850.
[88] D. Halim, and S. O. Reza Moheimani, 2002, "Spatial H2 Control of a Piezoelectric Laminate Beam: Experimental Implementation", *IEEE Transactions on Control Systems Technology*, **10**(4), pp. 533-546.
[89] D. Halim, and S. O. Reza Moheimani, 2002, "Experimental Implementation of Spatial H∞ Control on a Piezoelectric-Laminate Beam", *IEEE/ASME Transactions on Mechatronics*, **7**(3), pp. 346-356.
[90] D. Halim, and S. O. Reza Moheimani, 2001, "Spatial Resonant Control of Flexible Structures-Application to a Piezoelectric Laminate Beam", *IEEE Transactions on Control Systems Technology*, **9**(1), pp. 37-53.
[91] J. H. Han, K. H. Rew, and I. Lee, 1997, "An experimental study of active vibration control of composite structures with a piezo-ceramic actuator and a piezo-film sensor", *Smart Mater. Struct.*, **6**, pp. 549-558.
[92] A. Baz, S. Poh, 1988, "Performance of an active control system with piezoelectric actuators", *Journal of Sound and Vibration*, **126**(2), pp. 327-343.
[93] S. Narayanan, and V. Balamurugan, 2003, "Finite element modeling of piezolaminated smart structures for active vibration control with distributed sensors and actuators", *Journal of Sound and Vibration*, **262**(3), pp. 529-562.
[94] J. T. Scruggs, I. L. Cassidy, S. Behrens, 2012, "Multi-objective optimal control of vibratory energy harvesting systems", *Journal of Intelligent Material Systems and Structures*, **23**(18), pp. 2077-2093.
[95] G. Caruso, 2001, "A critical analysis of electric shunt circuits employed in piezoelectric passive vibration damping", *Smart Mater. Struct.*, **10**, pp. 1059-1068.
[96] S. Behrens, A. J. Fleming, and S. O. R. Moheimani, 2003, "A broadband controller for shunt piezoelectric damping of structural vibration", *Smart Mater. Struct*., **12**, pp. 18-28.
[97] G. K. Ottman, H. F. Hofmann, and G. A. Lesieutre, 2003, "Optimized Piezoelectric Energy Harvesting Circuit using Step-Down Converter in Discontinuous Conduction Mode", *IEEE Transactions on Power Electronics*, **18**(2), pp. 696-703.
[98] E. Lefeuvre, D. Audigier, C. Richard, and D. Guyomar, 2007, "Buck-Boost Converter for Sensorless Power Optimization of Piezoelectric Energy Harvester", *IEEE Transactions on Power Electronics*, **22**(5), pp. 2018-2025.
[99] A. J. Fleming, and S. O. R. Moheimani, 2003, "Adaptive piezoelectric shunt damping", *Smart Mater. Struct*., **12**, pp. 36-48.
[100] D. Niederberger, A. Fleming, S. O. R. Moheimani, and M. Morari, 2004, "Adaptive multi-mode resonant piezoelectric shunt damping", *Smart Mater. Struct*., **13**, pp. 1025-1035.

[101] A. J. Fleming, and S. O. R. Moheimani, 2005, "Control Orientated Synthesis of High-Performance Piezoelectric Shunt Impedance for Structural Vibration Control", *IEEE Transactions on Control Systems Technology*, **13**(1), pp. 98-112.
[102] D. Guyomar, and A. Badel, 2006, "Nonlinear semi-passive multimodal vibration damping: an efficient probabilistic approach", *Journal of Sound and Vibration*, **294**, pp. 249-268.
[103] D. Guyomar, A. Faiz, L. Petit, and C. Richard, 2006, "Wave reflection and transmission reduction using a piezoelectric semi-passive nonlinear technique", *Journal of the Acoustical Society of America*, **119**, pp. 285-298.
[104] K. Li, J. Y. Gauthier, and D. Guyomar, 2011, "Structural vibration control by synchronized switch damping energy transfer", *Journal of Sound and Vibration*, **330**, pp. 49-60.
[105] H. Shen, J. Qiu, H. Ji, K. Zhu, M. Balsi, I. Giorgio, and F. Dell'Isola, 2010, "A low-power circuit for piezoelectric vibration control by synchronized switching on voltage sources", *Sensors and Actuators A*, **161**, pp. 245-255.
[106] Y. Y. Chen, D. Vasic, F. Costa, W. J. Wu, and C. K. Lee, 2012, "A self-powered switching circuit for piezoelectric energy harvesting with velocity control", *Eur. Phys. J. Appl. Phys*., **57**, pp. 30903.
[107] D. Zhou, N. Kong, D. S. Ha, and D. J. Inman, 2010, "A Self-Powered Wireless Sensor Node for Structural Health Monitoring", *Proc. of SPIE, Health Monitoring of Structural and Biological Systems 2010*, **7650**.
[108] P. Wang, Y. Yan, G. Y. Tian, O. Bouzid, and Z. Ding, 2012, "Investigation of Wireless Sensor Networks for Structural Health Monitoring", *Journal of Sensors*, **2012**, 156329.
[109] C. Delebarre, T. Sainthuile, S. Grondel, and C. Paget, 2012, "Power Harvesting Capabilities of SHM Ultrasonic Sensors", *Smart Materials Research*, **2012**, 387638.
[110] D. Zhu, S. P. Beeby, M. J. Tudor, and N. R. Harris, 2009, "A Self Powered Tag for Wireless Structure Health Monitoring in Aeronautical Applications", *PowerMEMS 2009*, Washington DC, Dec. 1-4.
[111] K. Nakano, M. Ohori, and A. Tagaya, 2010, "Feasibility Study on Self-Powered Active Vibration Control using a Piezoelectric Actuator", *Proc. SPIE 7643, Active and Passive Smart Structures and Integrated Systems 2010*, 76432Y.
[112] M. Lallart, and D. Guyomar, 2010, "Self-Powered and Low-Power Piezoelectric Vibration Control using Nonlinear Approaches", *Vibration Control*, M. Lallart, Ed. InTech, pp. 265-291.
[113] S. Shimose, K. Makihara, and J. Onoda, 2012, "Comparison of Analog and Digital Self-Powered Systems in Multimodal Vibration Suppression", *Smart Materials Research*, **2012**, 287128.
[114] M. J. Konak, I. C. Powlesland, S. P. Van Der Velden, and S. C. Galea, 1997, "A Self-Powered Discrete Time Piezoelectric Vibration Damper", *Proc. SPIE in Smart Materials, Structures, and Integrated Systems*, **3241**, pp. 270-279.
[115] L. R. Ray, B. H. Koh, and L. Tian, 2000, "Damage Detection and Vibration Control in Smart Plates: Towards Multifunctional Smart Structures", *Journal of Intelligent Material Systems and Structures*, **11**(9), pp. 725-739.
[116] P. J. Cornwell, J. Goethal, J. Kowko, and M. Damianakis, 2005, "Enhancing Power Harvesting using a Tuned Auxiliary Structure", *J. Intelligent Material Systems and Structures*, **16**, pp. 825-834.

[117] P. E. Ma, J. E. Kim, and Y. Y. Kim, 2010, "Power-amplifying strategy in vibration powered energy harvesters", Active and passive smart structures and integrated systems *Proceedings of SPIE*, 7643, San Diego, CA.
[118] O. Aldraihem, and A. Baz, 2011, "Energy Harvester with a Dynamic Magnifier", *J. Intelligent Material Systems and Structures*, **22**(6).
[119] A. Aladwani, M. Arafa, O. Aldraihem, and A. Baz, 2011, "Cantilevered Piezoelectric Energy Harvester with a Dynamic Magnifier," ASME J. Vibration & Acoustics, Accepted.
[120] X. Tang, and L. Zuo, 2011, "Enhanced Vibration Energy Harvesting using Dual-Mass Systems", *J. Sound and Vibration*, **330**(21), pp. 5199-5209.
[121] H. Frahm, 1911, "Device for Damping Vibrations of Bodies", U.S. Patent No.989,958.
[122] J. P. Den Hartog, 1947, Mechanical Vibration, McGraw–Hill, New York.
[123] K. Xu, and T. Igusa, 1992, "Dynamic Characteristics of Multiple Substructures With Closely Spaced Frequencies", *Earthquake Eng. Struct. Dyn*., **21**, pp. 1059-1070.
[124] H. Yamaguchi, and N. Hampornchai, 1993, "Fundamental Characteristics of Multiple Tuned Mass Dampers for Suppressing Harmonically Forced Oscillations", *Earthquake Eng. Struct. Dyn.*, **22**, pp. 51–62.
[125] L. Zuo, and S. Nayfeh, 2006, "The Two-Degree-of-Freedom Tuned-Mass Damper for Suppression of Single-Mode Vibration Under Random and Harmonic Excitation", *ASME J. Vibration & Acoustics*, **128**, pp. 56-65.
[126] L. Zuo, 2009, "Effective and Robust Vibration Control Using Series Multiple Tuned-Mass Dampers", *J. Vibration and Acoustics*, **131**(3), 031003.
[127] G. B. Warburton, 1981, "Optimum Absorber Parameters for Minimizing Vibration Response", *Earthquake Eng. Structural Dynamics*, **9**(3), pp. 251-262.
[128] L. Kitis, B. P. Wang, and W. D. Pilkey, 1983, "Vibration Reduction Over a Frequency Range", *J. Sound and Vibration*, **89**(4), pp. 559-569.
[129] L. Zuo, and S. Nayfeh, 2004, "Minimax Optimization of Multi-Degree-of- Freedom Tuned-Mass Dampers", *J. Sound and Vibration*, **272**, pp. 893-908.
[130] L. Zuo, 2002, "Optimal Control with Structure Constraints and Its Application to the Design of Passive Mechanical Systems", M.S. thesis, Massachusetts Institute of Technology, Cambridge, MA.
[131] M. Arafa, W. Akl, A. Aladwani, O. Aldraihem, and A. Baz, 2011, "Experimental Implementation of a Cantilevered Piezoelectric Energy Harvester with a Dynamic Magnifier", *Smart Structures Conference proceedings of SPIE*, San Diego, CA.
[132] T. Dahlberg, 1989, "On Optimal use of the Mass of a Dynamic Vibration Absorber", *J. Sound and Vibration*, **132**, pp. 518-522.
[133] S. S. Rao, 2004, Mechanical Vibrations 4th Edition, Pearson Prentice Hall.
[134] H. W. Kim, S. Priya, H. Stephanou, and K. Uchino, 2007, "Consideration of Impedance Matching Techniques for Efficient Piezoelectric Energy Harvesting", *IEEE Transactions on Ultrasonics, Ferroelectrics, and Frequency Control*, **54**(9), pp. 1851-1859.
[135] H. W. Kim, A. Batra, S. Priya, K. Uchino, D. Markley, R. E. Newnham, and H. F. Hofmann, 2004, "Energy Harvesting using a Piezoelectric "Cymbal" Transducer in Dynamic Environment", *Jpn. J. Appl. Phys*., **43**, pp. 6178-6183.
[136] B. Marinkovic, and H. Koser, 2009, "Smart Sand – a Wide Bandwidth Vibration Energy Harvesting Platform", *Applied Physics Letters*, **94**, 103505.

[137] J. Baker, S. Roundy, and P. Wright, "Alternative Geometries for Increasing Power Density in Vibration Energy Scavenging for Wireless Sensor Networks", *3rd International Energy Conversion Engineering Conference*, AIAA-2005-5617.
[138] TRS Technologies Inc., www.trstechnologies.com
[139] J. Feenstra, J. Granstrom, and H. A. Sodano, 2008, "Mechanically Amplified Piezoelectric Stack Actuators for Harvesting Electrical Energy from a Backpack", *Mechanical Systems and Signal Processing*, **22**(3), pp. 721-734.
[140] T. B. Xu, X. Jiang, and J. Su, 2011, "A Piezoelectric Multilayer-Stacked Hybrid Actuation/Transduction System", *Appl. Phys. Lett.*, **98**, 243503.
[141] T. B. Xu, X. Jiang, J. Su, P. W. Rehrig, and W. S. Hackenberger, 2008, "Hybrid Piezoelectric Energy Harvesting Transducer System", US patent 7,446,459.
[142] T. B. Xu, E. J. Siochi, L. Zuo, X. Jiang, and J. H. Kang, 2012, "Multistage Force Amplification of Piezoelectric Stacks", US Patent Application 20120119620.
[143] M. Davis, D. Damjanovic, and N. Setter, 2004, "Direct Piezoelectric Effect in Relaxor-Ferroelectric Single Crystals", *Journal of Applied Physics*, **95**(10), pp. 5679-5684.
[144] D. Viehland, F. Tito, E. McLaughlin, H. Robinson, R. Janus, L. Ewart, and J. Powers, 2001, "Enhancement of Electromechanical Coupling Coefficient and Acoustic Power Density in Conventional "Hard" Pb(Zr1-xTix)O3 Ceramics by Application of Uniaxial Stress", *J. Appl. Phys.*, **90**(3), pp. 1496-1500.
[145] Y. Duan, J. Li, S. S. Li, J. B. Xia, and C. Chen, 2008, "Abnormal Ferroelectric Response and Enhancement of Piezoelectric of PbTiO3 under Uniaxial Compression", *J. Appl. Phys.*, **103**(8), 083713.
[146] F. Beer, E. R. Johnston, J. T. Dewolf, and D. F. Mazurek, 2009, "Mechanics of Materials", McGraw Hill Higher Education, New York.
[147] T. B. Xu, E. J. Siochi, J. H. Kang, L. Zuo, W. Zhou, X. Tang, and X. N. Jiang, 2011, "A Piezoelectric PZT Ceramic Multilayer Stack for Energy Harvesting under Dynamic Forces", *ASME DETC conference*, 2011-47720.
[148] J. Liang, and W. H. Liao, 2012, "Impedance Modeling and Analysis for Piezoelectric Energy Harvesting Systems", *IEEE/ASME Transactions on Mechatronic*, **17**(6), pp. 1145-1157.
[149] A. Erturk, and D. J. Inman, 2008, "Issues in Mathematical Modeling of Piezoelectric Energy Harvesters", *Smart Mater. Struct.*, **17**(6), 065016.
[150] M. Neubauer, M. Krack, and J. Wallaschek, 2010, "Parametric Studies on the Harvested Energy of Piezoelectric Switching Techniques", *Smart Mater. Struct.*, **19**(2), 025001.
[151] E. Perez-Delfin, J. E. Garcia, D. A. Ochoa, R. Perez, and F. Guerrero, 2011, "Effect of Mn-acceptor Dopant on Dielectric and Piezoelectric Responses of Lead Lanthanum Zirconate Titanate Piezoceramics", *J. Appl. Phys.*, **110**, 034106.
[152] D. M. Peairs, G. Park, and D. J. Inman, 2004, "Improving Accessibility of the Impedance-Based Structural Health Monitoring *Method", Journal of Intelligent Material Systems and Structures*, **15**(2), pp. 129-139.
[153] X. Wang, and J. Tang, 2010, "Damage Detection using Piezoelectric Admittance Approach with Inductive Circuitry", *Journal of Intelligent Material Systems and Structures*, **21**(7), pp. 667-676.
[154] X. Wang, and J. Tang, 2010, "An Enhanced Piezoelectric Impedance Approach for Damage Detection with Circuitry Integration", *Smart Materials and Structures*, **19**(4), 045001.

[155] L. Zuo, 2009, "Effective and Robust Vibration Control using Series Multiple Tuned-Mass Dampers", *Journal of Vibration and Acoustics*, **131**(3), 031003.
[156] H. A. Sodano, G. Park, and D. J. Inman, 2004, "Estimation of Electric Charge Output for Piezoelectric Energy Harvesting", *Strain*, **40**, pp. 49-58.
[157] A. Bloch, 1945, "Electromechanical Analogies and Their Use for the Analysis of Mechanical and Electromechanical System", *J. of the Institution of Electrical Engineers*, **92**(52), pp. 157-169.
[158] N. W. Hagood, and A. Von Flotow, 1991, "Damping of Structural Vibrations with Piezoelectric Materials and Passive Electrical Networks", *Journal of Sound and Vibration*, **146**(2), pp. 243-268.
[159] H. C. Ling, M. F. Yan, and W. W. Rhodes, 1990, "High Dielectric Constant and Small Temperature Coefficient Bismuth-based Dielectric Compositions", *Journal of Materials Research*, **5**, pp. 1752-1762.
[160] M. A. Ansari, J. Jyotsana, and A. K. Saxena, 2010, "Comparison of temperature coefficient of standard inductor by measuring change in inductance and resistance", *2010 Conference on Precision Electromagnetic Measurements (CPEM)*, June 13-18, pp. 378-379.
[161] D. Guyomar, and A. Badel, 2006, "Nonlinear semi-passive multimodal vibration damping: an efficient probabilistic approach", *Journal of Sound and Vibration*, **294**, pp. 249-268.
[162] D. Guyomar, A. Faiz, L. Petit, and C. Richard, 2006, "Wave reflection and transmission reduction using a piezoelectric semi-passive nonlinear technique", *Journal of the Acoustical Society of America*, **119**, pp. 285-298.
[163] K. Li, J. Y. Gauthier, and D. Guyomar, 2011, "Structural vibration control by synchronized switch damping energy transfer", *Journal of Sound and Vibration*, **330**, pp. 49-60.
[164] H. Shen, J. Qiu, H. Ji, K. Zhu, M. Balsi, I. Giorgio, and F. Dell'Isola, 2010, "A low-power circuit for piezoelectric vibration control by synchronized switching on voltage sources", *Sensors and Actuators A*, **161**, pp. 245-255.
[165] Y. Y. Chen, D. Vasic, F. Costa, W. J. Wu, and C. K. Lee, 2012, "A self-powered switching circuit for piezoelectric energy harvesting with velocity control", *Eur. Phys. J. Appl. Phys*., **57**, pp. 30903.
[166] S. S. Rao, Mechanical Vibrations 4th Edition, Pearson Prentice Hall, 2004.
[167] H. A. Sodano, G. Park, and D. J. Inman, 2004, "Estimation of electric charge output for piezoelectric energy harvesting", *Strain*, **40**, pp. 49-58.
[168] X. Tang, and L. Zuo, 2010, "Self-powered active control of structures with TMDs", *IMAC XXVIII Conference and Exposition on Structural Dynamics: Structural Dynamics and Renewable Energy*, Jacksonville, Flovida, Feb 1-4, pp. 5099.
[169] T. T. Wu, Z. G. Huang, T. C. Tsai, and T. C. Wu, 2008, "Evidence of complete band gap and resonances in a plate with periodic stubbed surface", *Applied Physics Letters*, **93**, 111902.
[170] A. Bergamini, T. Delpero, L. De Simoni, L. Di Lillo, M. Ruzzene, and P. Ermanni, 2013, "Phononic crystal with adaptive connectivity Advanced Materials", doi: 10.1002/adma.201305280.
[171] F. Casadei, T. Delpero, A. Bergamini, P. Ermanni, and M. Ruzzene, 2012, "Piezoelectric resonator arrays for tunable acoustic waveguides and metamaterials", *Journal of Applied Physics*, **112**, 064902.

[172] M. Carrara, M. R. Cacan, J. Toussaint, M. J. Leamy, M. Ruzzene, and A. Erturk, 2013, "Metamaterial-inspired structures and concepts for elastoacoustic wave energy harvesting", *Smart Mater. Struct*., **22**, 065004.
[173] O. Thorp, M. Ruzzene, and A. Baz, 2001, "Attenuation and localization of wave propagation in rods with periodic shunted piezoelectric patches", *Smart Mater. Struct*., **10**, pp. 979-989.
[174] O. Thorp, M. Ruzzene, and A. Baz, 2005, "Attenuation of wave propagation in fluid-loaded shells with periodic shunted piezoelectric rings", *Smart Mater. Struct*., **14**, pp. 594-604.
[175] B. S. Beck, K. A. Cunefare, M. Ruzzene, and M. Collet, 2011, "Experiment analysis of a cantilever beam with a shunted piezoelectric periodic array", *Journal of Intelligent Material Systems and Structures*, **22**, pp. 1177-1187.
[176] A. Spadoni, M. Ruzzene, and K. Cunefare, 2009, "Vibration and wave propagation control of plates with periodic arrays of shunted piezoelectric patches", *Journal of Intelligent Material Systems and Structures*, **20**, pp. 979-990.
[177] F. Casadei, M. Ruzzene, B. Beck, and K. Cunefare, 2009, "Vibration control of plates featuring periodic arrays of hybrid shunted piezoelectric patches", *Proceedings of SPIE, Active and passive smart structures and integrated systems*, 7288, March 2009, San Diego, CA.
[178] L. Airoldi, and M. Ruzzene, 2011, "Wave propagation control in beams through periodic multi-branch shunts", *Journal of Intelligent Material Systems and Structures*, **22**, pp. 1567-1579.
[179] J. Becker, O. Fein, M. Maess, and L. Gaul, 2006, "Finite Element-based Analysis of Shunted Piezoelectric Structures for Vibration Damping", *Computers and Structures*, **84**, pp. 2340-2350.
[180] R. D. Cook, D. S. Malkus, M. E. Plesha, and R. J. Witt, 2007, "Concepts and applications of finite element analysis", John Wiley & Sons, New York.
[181] A. Bloch, 1945, "Electromechanical analogies and their use for the analysis of mechanical and electromechanical system", *J. of the Institution of Electrical Engineers*, **92**, pp. 157-169.
[182] K. Narmashiri, and S. M. T. Hosseini-Tabatabai, 2013, "Tuned mass damper: an energy dissipation device for earthquake/wind resistant buildings", LAP LAMBERT Academic Publishing.
[183] W. Zhou, and L. Zuo, 2012, "Sensitivity-enhanced admittance-based structure health monitoring using a higher-order resonant circuit", *Smart Materials and Structures*, **21**, 105023.
[184] L. Zuo, 2009, "Effective and robust vibration control using series multiple tuned-mass dampers", *Journal of Vibration and Acoustics*, **131**, 031003.
[185] W. Zhou, Y. Wu, and L. Zuo, 2013, "Experiment study on damage detection method with higher-order circuit", *SPIE Smart Structures/NDE*, March 12-13, San Diego, CA.
[186] X. Wang, and J. Tang, 2010, "Damage detection using piezoelectric admittance approach with inductive circuitry", *Journal of Intelligent Material Systems and Structures*, **21**, pp. 667-676.